An Insertion Loss Based Fully Inkjet-Printed Flexible Chipless RFID Tag and Its Application in Concentration Measurements of Liquids and Gases

Zonghao Li

Master of Engineering

Department of Electrical and Computer Engineering

McGill University

Montreal,Quebec

2019-05

A thesis submitted to McGill University in partial fulfilment of the requirement for the degree of Master of Engineering

DEDICATION

To my beloved parents and grandmother...

ACKNOWLEDGEMENTS

I would like to first thank my parents who brought me to this wonderful world, and my grandmother who raised me up and taught me how to become a better person. I would like to especially thank Professor Sharmistha Bhadra for providing invaluable mentorship and supports through my study and research. Also, thank you, Mr. James Dietrich, from CMC Microsystems for aiding the probe station measurement at the University of Manitoba, Mr. Don Pavlasek at McGill University for the antenna fabrications, and Mr. Maxime Thibault from Polytechnique Montreal for the antenna characterizations. This thesis will not be completed without any of your bits of help.

ABSTRACT

This thesis presents the design and application of the flexible printed chipless radio frequency identification tag (RFID). Specifically, the insertion loss based technique is followed in this work. Firstly, it explores the challenges in the printed transmission line design, particularly, microstrip line and coplanar waveguide (CPW). Secondly, with these two transmission line topology as the skeleton, different ultra-wideband (UWB) antenna and resonator circuit designs are studied and compared. Thirdly, the reader antennas are designed using a novel methodology proposed in a research paper. In the end, a fully inkjet-printed flexible CPW chipless RFID tag shows promising performance. The chipless RFID tag comes with a CPW transmission line that is coupled to the multiresonator circuit to encode the information in the frequency domain. Two cross-polarized UWB antennas connected to the CPW receive and transmit the signals. As a proof-of-concept, three spiral resonators are used to encode a 3-bit signature, which can be easily expanded to more bits by adding more resonators. It will be shown that by shorting resonators, one has the freedom to encode different frequency signatures. The RFID tag is used for the concentration measurements of different binary liquid mixtures by characterizing the frequency response of the sensor, in both wired and wireless experiments. A capillary tube is placed on one of the resonators to allow the interaction between the sensor and the solutions. Correlations between the concentration and the frequency response are extracted from the change of the insertion loss at the resonant frequency $|\Delta S_{21}|$, the half-power 3-dB bandwidth ΔBW, and the shift of the resonant frequency $|\Delta f_{res}|$.

In addition, the sensor is applied for the concentration measurement of acetic acid vapor, varied from 20 to 120 ppm. The applications of this chipless RFID include but are not limited to logistic tracking, chemical and biomedical sensing, and environment monitoring.

ABRÉGÉ

Ce rapport présente la conception et les applications d'étiquettes de radio-identification (sigle RFID en anglais). Plus spécifiquement, ce travail se concentre sur la technique de pertes par insertion. Une introduction examine les défis que posent la conception de lignes de transmission imprimées, particulièrement les lignes microrubans et les guides d'ondes coplanaires (GOC). Dans une deuxième partie, en se basant sur la topologie de ces deux lignes de transmissions, différentes conceptions de circuits d'antennes et résonateurs ultras large bande (ULB) seront étudiées et comparées. La section suivante traite de la conception de lecteur d'antennes RFID en s'appuyant sur une nouvelle méthodologie issue d'un article scientifique. Finalement, les performances prometteuses d'une architecture flexible imprimée par jet d'encre RFID à GOC sont démontrées. Le RFID sans puce s'accompagne d'une ligne de transmission GOC couplée à un circuit multirésonateur qui encode l'information en domaine fréquentiel. Deux antennes ULB à polarisation croisée sont connectées au GOC pour la réception et transmission des signaux. Comme preuve de concept, trois résonateurs en spirale sont utilisés pour encoder une signature 3 bits qui peut facilement s'étendre à plus de bits en ajoutant d'avantages de résonateurs. On démontre que la mise en court-circuit des résonateurs permet à l'un d'entre eux d'encoder des signatures à différentes fréquences. Le RFID est utilisé pour des mesures de concentration de différents mélanges binaires liquides en caractérisant la réponse fréquentielle du capteur, des expériences à la fois câblées ou sans fil sont réalisées. Un tube capillaire est placé dans l'un des résonateurs pour permettre une interaction entre le capteur et les solutions tests. Des corrélations entre la concentration et la réponse fréquentielle sont extraites en relevant la modification des pertes par insertion à la fréquence de résonance $|\Delta S_{21}|$, la bande passante à la puissance moitié -3 dB ΔBW et le décalage de la fréquence de résonance $|\Delta f_{res}|$. De plus, le capteur est employé pour des mesures de concentration de vapeur d'acide acétique sur une plage de 20 à 120 ppm. Les applications de cette étiquette RFID inclus également le suivi logistique, la détection chimique et biomédicale et la surveillance environnementale sans exclure d'autres utilisations possibles.

TABLE OF CONTENTS

LIST OF TABLES

LIST OF FIGURES

CHAPTER 1
Introduction

1.1 Background and Research Scope

Radio frequency identification (RFID) is a contactless communication technology that has been used widely used in many applications such as logistics tagging and tracking, security surveillance, database management, environment monitoring, internet-of-things (IoT) , as well as chemical and biological sensing. With its versatility in many fields, it is no surprise that the RFID market has already surpassed \$10 billion [1]. The idea of RFID technology was conceptualized in the 1950s and became matured in 1980s due to the development of application-specific-integrated-circuits (ASIC) that would store the identification information. The smaller size and lower power-consumption ASICs dominant the manufacturing of RFID tags that ensure them better compactness and durability. Nevertheless, the presence of ASICs inevitably rises up the fabrication cost during the manufacturing process considering massive productions. A reasonably estimated cost of a passive RFID tag is 5 cents that give them unavoidable high cost compared to some other optical recognition methods such as the barcode technology [2]. It is shown that the absence of silicon chips on the RFID tag could potentially lower down its cost to around 0.1 cents if they are directly printed on the targeted item. Therefore, the major obstacle to stopping the RFID technology from popularizing is its cost, and the best way to lower it down is to remove chips or namely chipless RFID tag.

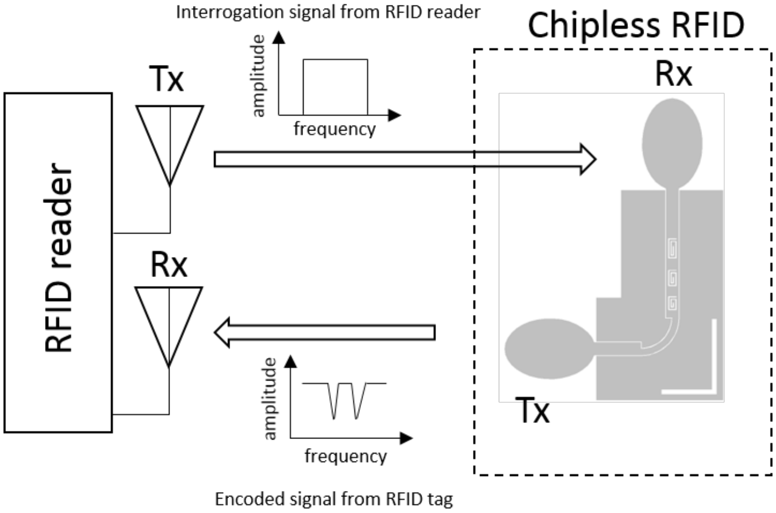

Figure 1–1: Block diagram of the chipless RFID system.

Unlike traditional RFID tags, the chipless RFID tag has no discrete integrated circuit components on it. Operating through the energy harvesting of RF signals, it has the advantages of low-cost, high durability, and compatibility with flexible substrates and printing technologies. Fig. 1–1 shows a complete block diagram of the chipless RFID system, where the interrogating signal is sent from the RFID reader to the chipless RFID tag. The manipulation of the amplitude in the frequency spectrum is a way to encode the information. Afterward, the tag will transmit the encoded signal back to the reader for further information processing. It is noted that the antennas on both primary and secondary side are cross-polarized, which is for providing a good isolation between the transmitting and receiving signals [3].

A very important application of the chipless RFID tag is sensing [1]. This could be for sensing liquid solutions and gas concentrations [4, 5] as they are found to be significant in the fields of food, medicine manufacturing, environment monitoring, and biomedical engineering. In this research, with different approaches attempted, a fully inkjet-printed flexible chipless RFID tag will be presented. It is based on a coplanar waveguide (CPW) coupled with multiresonators to encode the information in the frequency domain. Two cross-polarized ultra-wideband (UWB) antennas connected to the CPW receive and transmit the signals. As a proof-of-concept, three spiral resonators are used to encode a 3-bit signature, which can be easily expanded to more bits by adding more resonators. Later on, it is applied for sensing different liquids and gases concentrations. The scope of the research can be summarized in the following:

- Fabrication and testing of flexible printed chipless RFID tag.
- Design of RFID tag UWB antennas for transmitting and receiving signals from the reader.
- Design of UWB antennas at the reader end for transmitting and receiving signals from the chipless RFID tag.
- Concentration measurements of liquid solutions using the design chipless RFID tag.
- Concentration measurements of gases using the design chipless RFID tag.

1.2 Motivations of the Research

To approach the design of chipless RFID, the selection of topology is critical. The research on chipless RFID have progressed marvelously, and chipless RFIDs have been applied to many applications such as item tracking and wireless sensing. So far the only commercial chipless RFID system available is based on the surface acoustic wave (SAW) [6] that encodes the information in the time domain. Frequency domain solutions such as [2, 7] are based on the radar cross section (RCS) , and [3, 8] are based on the insertion loss response by the use of microwave multiresonator circuits. Between these two different approaches, only RCS based ones have been reported to be fully printed and flexible [9, 7, 10, 11, 12]. Although an insertion loss response based rigid-flexible chipless RFID tag is reported in [13], it is manufactured on a laminated board using the traditional printed circuit board (PCB) fabrication method. Some flexible printed microwave multiresonator circuits are reported in [14] to create insertion loss signatures, but they are not able to operate wirelessly.

Compared to RCS based RFID tags, insertion loss based ones are believed to have less mutual coupling effects, more possible bit numbers, and easier information encoding methods [3]. It has been shown that shorting and opening a resonator can correspondingly encode ”0” and ”1” in the insertion loss response. Therefore, the insertion loss based design is followed in this thesis. It will be shown later that, it is so far the only reported flexible printed insertion loss based chipless RFID tag among literature. The tag will have three parts, the multiresonator circuit for generating the frequency signature, the planar transmission line to couple the resonators, and the cross-polarized antennas to transmit and receive the interrogation signal from the RFID reader. The insertion loss based chipless RFID tag is found to be compatible with the printing technology, making them cheap and fast to fabricate.

1.2.1 Overview on Inkjet Printing Technology

Printing technologies have been successfully applied in the RFID technology [15], and there are major reasons behind. First, most printing methods are additive

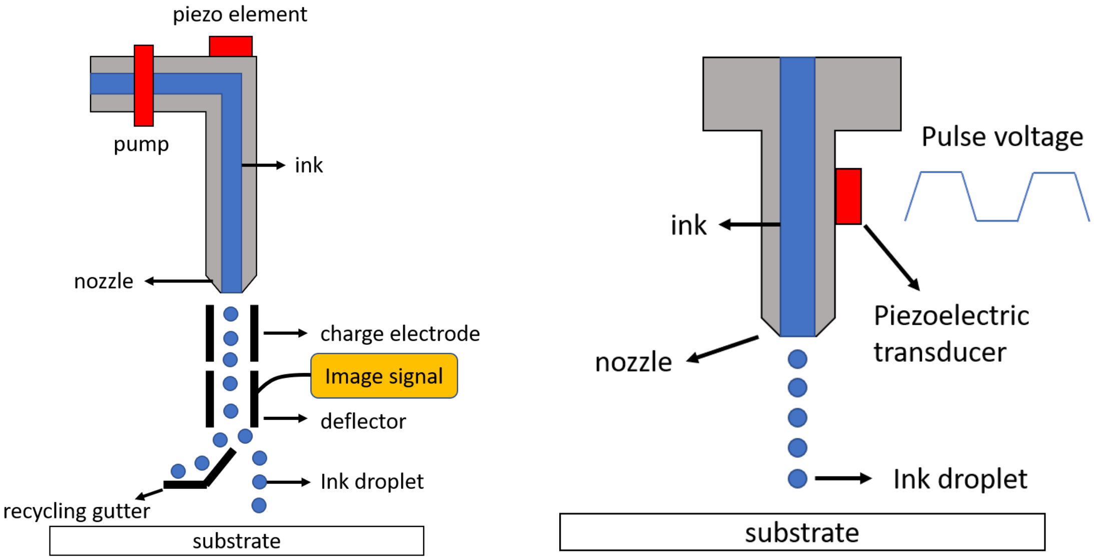

(a) (b)

Figure 1–2: (a) Continuous inkjet printing (CIJ) and (b) drop-on-demand (DOD) printing.

processes, which only deposit material on wanted areas, thereby saving more material and lowering the cost. Second, due to the absence of solid-state electronics, the passive chipless RFID tag is fully printable, making it ideal for instant mass production. Third, printing technologies are generally compatible with a wide variety of flexible substrate, making them an ideal candidate for flexible electronic fabrications. The flexible chipless RFID tag has the advantage of attaching it to various shape of items, making them suitable for embedded applications. These benefits make printing technologies more advantageous than the PCB fabrication.

Inkjet printing is a type of fast and accurate printing process. An inkjet printer will first interpret the prepared circuit design layout by converting it to the monochrome bitmap format, which is usually the image file type used in the inkjet printer. The pixels in the bitmap file will then represent the deposition areas of the ink. By the way of ink deposition, inkjet printing can be sorted as the continuous inkjet printing (CIJ) and the drop-on-demand inkjet printing (DOD) . It is noted that in both methods, the printer does not contact the printed area, thus enabling patterning on rigid and flexible substrates [16].

Fig. 1–2 shows the mechanisms behind these two inkjet printing methods. For CIJ, the ink will continuously flow, and the ink droplets will be charged by the charge electrode, which enables the deflector to select the droplets. The image signal will be applied to the deflector, and the unwanted droplets will be deflected to the recycling gutter for reuse, decreasing the waste of the ink. The DOD method, on the other hand, will only drop the liquid on the substrate if the nozzle is switched on. The pulse voltage will be applied on the piezoelectric transducer to convert the electric signal to mechanical on and off signal. Usually, either the substrate or the printing nozzle would move to complete the printing process. Due to its compatibility with various flexible substrates, the inkjet printing technology has been widely used in fabricating flexible electronics such as flexible displays, solar cells, sensors, and actuators [17].

Primarily, there are two types of printing ink for electronics, organic and inorganic. The organic inks have the advantage of flexibility and better printability, whereas the disadvantages are poor environmental stability and low charge mobility. The inorganic inks have opposite features. Therefore, there is a trade-off in between the selection of ink, which also depends on the compatibility of the printer. Inks can also be categorized as conductor, semiconductor, and insulator based on their conductivity. It is noted that for inorganic metal nanoparticle-based conductive ink, to obtain a reasonable viscosity and continuity so that the ink is printable, nanoparticles are covered by the surfactants to prevent their agglomeration. After the deposition of the nanoparticle-based conductive ink, the circuit has to be baked in a high-enough temperature environment so that the solvent and the surfactant in the ink can be evaporated, and a continuous film is formed. This process is called sintering. It can be concluded that the process of inkjet printing includes: preparation of the circuit layout ⟶ bitmap file formation ⟶ compatible ink selection ⟶ ink deposition ⟶ sintering ⟶ performance testing.

1.2.2 Microwave Techniques for Sensing Liquid Solutions

Microwave techniques for sensing liquid solutions have been studied numerously for the applications such as food, beverage, medicine manufacturing and even oil industry due to their prompt and accurate response, fine accuracy, non-invasive and non-destructive natures [18, 19, 20, 21]. Primarily, the microwave resonant-type sensors are dominant the sensing of liquid compounds. The variation of the concentration produces a change of the resonant frequency and quality factor (Q-factor), which provides an easy approach to analyze the liquid solutions. Specifically, the change of the insertion loss at the resonant frequency $|\Delta S_{21}|$, the change half-power 3-dB bandwidth ΔBW, and the shift of the resonant frequency $|\Delta f_{res}|$ are usually the choices for information extractions.

Several liquid compound sensors based on the microwave resonators have been reported in various literature. The rectangular-waveguide resonator designed in [21] using $\mathrm{T}E_{101}$ mode has achieved a very high sensitivity for both water/sodium chloride (NaCl) and water/sucrose binary solutions. However, the structure of the rectangular waveguide is bulky and its fabrication method is not suitable for massive production. The cylindrical resonator using TE_{010} mode has been studied in [22], which relies on the return loss response to measure the concentrations for different binary liquid solutions. Planar microwave resonator structure is another popular choice for liquid sensing. In [23], a microstrip line coupled with a complementary split-ring resonator (CSRR) is employed to sense the water/ethanol solution with different concentrations. The solutions are passed through the polydimethylsiloxane (PDMS) microfluidic channel on one edge of the CSRR, and the flow will directly contact the resonator. In [24] the testing liquid sample has to be placed in a cavity on the resonator. This makes the system inappropriate for monitoring continuous liquid flow, and the inevitable residual liquid within the cavity will cause the drifting error. Other planar structure sensors are reported in [25, 26], where the sensor microfabrication in the former leads to a higher cost in the prototyping process. So far, it seems only the liquid sensor in [27] has been reported to be fully printed and flexible. Nevertheless, all above-mentioned sensors require a wired connection to a data readout unit, making them unsuitable for embedded applications. Some designs utilize active components to further improve the accuracy and sensitivity of the sensors. In [4] an active feedback loop with an amplifier is employed to enhance the Q-factor of the sensor; in [28] a voltage-controlled oscillator with a very high Q-factor is used to analyze organic liquids by monitoring the shift of resonant frequency. Active sensors demonstrate better accuracy and sensitivity. However, the requirement of power supply leads to the necessity of battery replacement, not ideal for the long-term and embedded monitoring. With all previous-mentioned microwave liquid sensors discussed, a fully passive low-cost and wireless sensor is the ideal solution to the above issues. It is the motivation of this work.

1.2.3 Acetic Acid Vapor Sensing

Detection of volatile organic compounds (VOCs) receives enormous attention due to its significance in the environment and health monitoring [29, 30]. Many designs have been proposed for detecting VOCs, such as using polymer-coated cantilevers, thin-films, fibrous or nanostructured chemoresistive sensors, and vertical-cavity surface emitting laser vertical-cavity surface emitting lasers (VCSELs) [31, 32, 33, 34] . Recently, [5] shows the method of coating a thin PDMS on a microwave resonator to detect different concentrations of acetone gases by utilizing the swelling effect, obtaining promising results. The absorption of acetone molecules changes the insertion loss and resonant frequency of the resonator, thereby rendering a correlation with respect to the acetone gas concentration. This approach not only solves the temperature requirement for those chemoresistive sensors but also drastically lowers down the power consumption in contrast to VCSELs. Inspired by this approach, a thin PDMS layer will be coated on one of the resonators on the proposed printed flexible RFID, and it will be employed for the acetic acid vapor concentration measurement. Due to the lack of some experimental equipment, only the wired measurements will be conducted.

1.3 Fabrications, Simulations and Measurements

In this research work, the flexible substrate used is a 127 μm thickness Dupton Kapton polyimide (PI) with excellent electrical properties ($\epsilon_r = 3.4$ and $tan\delta = 0.0026$). The flexible silver nanoparticle conductive ink ($\sigma = 1{\times}10^6\ S/m$), as well as

Table 1–1: Major design resources in this work

Simulation	Flexible substrate	Printing technology	VNA
ANSYS HFSS	Kapton polyimide (PI) ($\epsilon_r = 3.4$, $tan\delta = 0.0026$)	Inkjet printing	Keysight E5063A

the inkjet printer, are from Voltera that supports DOD mode. The printer supports up to 200 μm feature size and 50 μm deposition thickness. All simulations are done using ANSYS HFSS , and S-parameters are measured by the vector network analyzer (VNA , Keysight E5063A). Table 1–1 lists basic design resources used in this work.

1.4 Thesis Structure

This thesis consists of eight chapters. Chapter 1 is the background introduction of this thesis. Chapter 2 will address the transmission line theory and introduce two different printed transmission line designs: microstrip line and CPW. Chapter 3 will present microstrip based and CPW based UWB antennas. Chapter 4 will discuss printed microstrip based and CPW based multiresonator circuits. Chapter 5 will introduce the design of the reader antenna. Chapter 6 will present the final flexible printed chipless RFID design and its application in liquid concentration measurements. Chapter 7 will present the acetic acid measurement using the proposed printed flexible multiresonator circuits. Finally, Chapter 8 will conclude this thesis and discuss future work.

CHAPTER 2
Printed Transmission Line Design

2.1 Review on Transmission Line Theory

2.1.1 Lumped Element Model Analysis

As mentioned before, the transmission line is required to excite the coupled resonators so that the desired frequency signature is obtained. Therefore, it is a benefit to briefly review some transmission line theory before moving onto the actual transmission line structures. Many of the following formulas can be found and derived from [35].

A transmission line is a guided wave structure that would consist of two or more separate conductors. Common transmission line structures include but are not limited to coaxial cables, microstrip lines and striplines on circuit boards. Usually, two-conductor transmission lines are used, where one conductor is for the signal propagation, and another is the signal ground so that the structure is closed-loop. When analyzing a two-conductor transmission line, it is convenient to treat it as the lumped element model, rather than from the aspect of electromagnetic fields. Particularly, it will be narrowed down to the situation of transverse electromagnetic wave propagation or TEM as it is a simple wave that consists of only one electric field $\bar{E}$ and magnetic field component $\bar{H}$, orthogonal to each other. It is the simplest way to wave propagation and it is dominantly appearing in different transmission

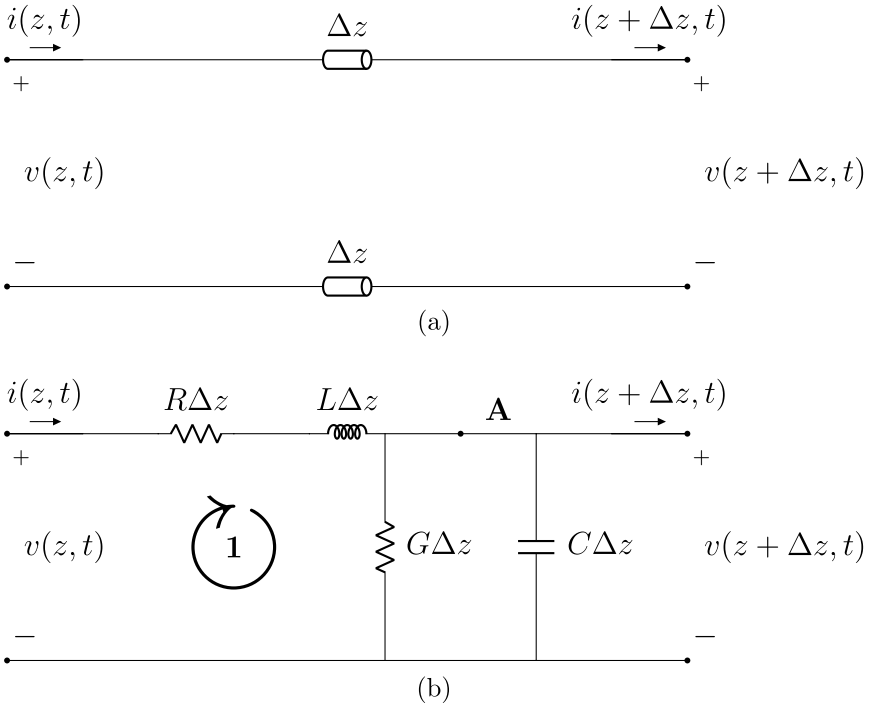

Figure 2–1: (a) A infinitesimal length transmission line Δz, (b) equivalent lumped element model that supports TEM mode.

line structure, therefore the lumped element model in the following will represent the TEM mode only.

Fig. 2–1 shows an infinitesimal length transmission line section Δz with its lumped element model, where

- R: the series resistance of the transmission line per unit length Ω/m
- L: the series inductance of the transmission line per unit length H/m
- C: the shunt capacitance between two conductors per unit length F/m
- G: the shunt conductance between two conductors per unit length H/m

It is easy to understand the contributions of these lumped elements. The resistance R is due to the finite conductivity of the conductors; the inductance L is due to the self-inductance of two conductors; the capacitance C is caused by the proximity of two conductors, analogy to a parallel plate capacitor; and the conductance G is caused by the dielectric losses between two conductors. It is noted that it is possible for a transmission line with uneven R, L, C and G, therefore the model in Fig. 2–1 is also called distributed lumped element model, which means it is spatial-dependent. The goal is to find out how the wave travels within this infinitesimal length transmission line. The analysis is started by writing down the Kirchoff's Voltage Law (KVL) and Kirchoff's Current Law (KCL) at loop **1** and node **A** in Fig. 2–1(b), respectively, which leads to

$$\frac{v(z+\Delta z,t)-v(z,t)}{\Delta z}=-Ri(z,t)-L\frac{\partial i(z,t)}{\partial t} \tag{2.1}$$

$$\frac{i(z+\Delta z,t)-i(z,t)}{\Delta z}=-Gv(z+\Delta z,t)-C\frac{\partial v(z+\Delta z,t)}{\partial t} \tag{2.2}$$

By taking the limit as $\Delta z \longrightarrow 0$ of above two equations, it leads to the Telegrapher's Equations

$$\frac{\partial v(z,t)}{\partial z}=-Ri(z,t)-L\frac{\partial i(z,t)}{\partial t} \tag{2.3}$$

$$\frac{\partial i(z,t)}{\partial z}=-Gv(z,t)-C\frac{\partial v(z,t)}{\partial t} \tag{2.4}$$

By taking the differentiation with respect to z of Eq. 2.3

$$\frac{\partial^2 v(z,t)}{\partial^2 z}=-R\frac{\partial i(z,t)}{\partial z}-L\frac{\partial^2 i(z,t)}{\partial z\partial t} \tag{2.5}$$

Taking the differentiation with respect to t of Eq. 2.4

$$\frac{\partial^2 i(z,t)}{\partial z \partial t} = -G\frac{\partial v(z,t)}{\partial t} - C\frac{\partial^2 v(z,t)}{\partial^2 t} \tag{2.6}$$

Substitute Eq. 2.6 to Eq. 2.5 for $\frac{\partial^2 i(z,t)}{\partial z \partial t}$

$$\frac{\partial^2 v(z,t)}{\partial^2 z} = -R\frac{\partial i(z,t)}{\partial z} + LG\frac{\partial v(z,t)}{\partial t} + LC\frac{\partial^2 v(z,t)}{\partial^2 t} \tag{2.7}$$

Substitute Eq. 2.4 to Eq. 2.7 for $\frac{\partial i(z,t)}{\partial z}$ so that it is a fuction of only one variable $v(z,t)$

$$\frac{\partial^2 v(z,t)}{\partial^2 z} = RGv(z,t) + (RC + LG)\frac{\partial v(z,t)}{\partial t} + LG\frac{\partial v(z,t)}{\partial t} + LC\frac{\partial^2 v(z,t)}{\partial^2 t} \tag{2.8}$$

Eq. 2.8 is the wave equation of the voltage within the transmission line with spatial and time variations. For simplicity purposes, which is also valid in the actual applications, we could neglect the losses of the transmission line ($R = 0$ and $G = 0$). So the above equation can be simplified as

$$\frac{\partial^2 v(z,t)}{\partial^2 z} - LC\frac{\partial^2 v(z,t)}{\partial^2 t} = 0 \tag{2.9}$$

By comparing to one dimensional plane wave equation, the phase velocity v_p is defined as

$$v_p = \frac{1}{\sqrt{LC}} \tag{2.10}$$

Looking back to Eq. 2.9, which is a linear homogeneous second-order partial differential equation, whose solution form is well-known as

$$v(z,t) = af_1(t - \frac{z}{v_p}) + bf_2(t + \frac{z}{v_p}) \tag{2.11}$$

where a and b are some arbitrary amplitude scaling constant, and f_1 and f_2 are some functions, representing the forward and backward wave, respectively. The current direction in Fig. 2–1 is defined as the forward. It is noted that the forward and backward wave does not need to be the same shape or the same amplitude. The solution of the current $i(z,t)$ can be found by taking the integral of both sides of Eq. 2.3 assuming it is lossless ($R = 0$), then substituting Eq. 2.11 for $v(z,t)$, which leads to

$$i(z,t) = \frac{a}{Lv_p} f_1(t - \frac{z}{v_p}) - \frac{b}{Lv_p} f_2(t + \frac{z}{v_p}) \tag{2.12}$$

The ratio between either forward voltage and current, or backward voltage and current, is defined as characteristic impedance Z_0. For instance, if the forward voltage and current are used for this definition

$$Z_0 = \sqrt{\frac{L}{C}} \tag{2.13}$$

Going back to Eq. 2.8, if the steady-state response is under the interest, the time-harmonic analysis can be used. So follow the similar procedure, by substituting $v(z,t) = Re[V(z)e^{jwt}]$ to Eq. 2.8

$$\frac{\partial^2 V(z)}{\partial^2 z} - (R + j\omega L)(G + j\omega C)V(z) = 0 \tag{2.14}$$

The propagation constant γ is defined as

$$\gamma = \sqrt{(R + j\omega L)(G + j\omega C)} = \alpha + j\beta \tag{2.15}$$

where α is defined as the attenuation constant, and β is defined as the phase constant. Further expanding the expression for γ

$$\gamma = j\omega\sqrt{LC}(1 + \frac{R}{j\omega L})^{0.5}(1 + \frac{G}{j\omega}C)^{0.5} \tag{2.16}$$

Applying binomial series approximation, and expanding the last two terms, it can be shown that

$$\gamma \approx \frac{\sqrt{LC}}{2}\frac{RC + LG}{LC} + j\omega\sqrt{LC} \tag{2.17}$$

Substitute Eq. 2.17 to Eq. 2.15, α and β can be found as

$$\alpha = \frac{\sqrt{LC}}{2}\frac{RC + LG}{LC} \tag{2.18}$$

$$\beta = \omega\sqrt{LC} \tag{2.19}$$

When the transmission line is lossless, there will be no physical attenuation ($\alpha = 0$), therefore

$$\gamma = j\beta = j\omega\sqrt{LC} \tag{2.20}$$

It is noted that from the physical meaning of phase constant β, it is defined as how the phase changes per unit length. Therefore, β is also defined as

$$\beta = \frac{2\pi}{\lambda} \tag{2.21}$$

where λ is the wavelength, and since it is well-known that $\lambda = v_p f$ where f is the frequency of the wave, the phase velocity is then correlated to β by

$$v_p = \frac{2\pi f}{\beta} \tag{2.22}$$

Finally, using the propagation constant for the expression of Eq. 2.14

$$\frac{\partial^2 V(z)}{\partial^2 z} - \gamma^2 V(z) = 0 \tag{2.23}$$

In analogy to the voltage, by substitute $i(z,t) = Re[I(z)e^{jwt}]$ and following the similar derivation from Eq. 2.3 to Eq. 2.8, one would arrive at

$$\frac{\partial^2 I(z)}{\partial^2 z} - \gamma^2 I(z) = 0 \tag{2.24}$$

Eq. 2.23 and 2.24 are similar to one dimensional Helmholtz equation, whose solution form is known as

$$V(z) = V_z^+ e^{-\gamma z} + V_z^- e^{\gamma z} \tag{2.25}$$

$$I(z) = I_z^+ e^{-\gamma z} - I_z^- e^{\gamma z} \tag{2.26}$$

In which the positive and negative sign represents the wave propagation is either forward or backward, respectively. Therefore, it is concluded that the voltage at any location on a transmission line at one time instant, is equal to the summation of both forward and backward voltage waves. The current, on the other hand, is equal to the subtraction of both forward and backward current waves. Alternatively, one can also use the characteristic impedance Z_0 to relate Eq. 2.25 and 2.26. For instance, Eq. 2.26 can be rewritten as

$$I(z) = \frac{V_z^+}{Z_0} e^{-\gamma z} - \frac{V_z^-}{Z_0} e^{\gamma z} \tag{2.27}$$

With the wave solutions Eq. 2.25 and 2.26 found, the characteristic impedance can also be found by the time-harmonic analysis. Substituting $v(z,t) = Re[V(z)e^{jwt}]$ and $i(z,t) = Re[I(z)e^{jwt}]$ to Eq. 2.3 and 2.4, respectively

$$\frac{\partial V(z)}{\partial z} = -(R + j\omega L)I(z) \tag{2.28}$$

$$\frac{\partial I(z)}{\partial z} = -(G + j\omega C)V(z) \tag{2.29}$$

Substituting Eq. 2.25 to the right-hand-side of Eq. 2.28 and solve for $I(z)$

$$I_z = \frac{\gamma}{R + j\omega L}(V_z^+ e^{-\gamma z} - V_z^- e^{\gamma z}) \tag{2.30}$$

Equating Eq. 2.26 and 2.30 and the expression for I_z^+ and I_z^- can be found as

$$I_z^+ = V_z^+ \frac{\gamma}{R + j\omega L} \tag{2.31}$$

$$I_z^- = V_z^- \frac{\gamma}{R + j\omega L} \tag{2.32}$$

With the definition of the characteristic impedance introduced before, and the expression of γ in Eq. 2.15

$$Z_0 = \frac{R + j\omega L}{\gamma} = \sqrt{\frac{R + j\omega L}{G + j\omega C}} \tag{2.33}$$

When the transmission line is lossless, $Z_0 = \sqrt{\frac{L}{C}}$, which is identical to Eq. 2.13.

The phase velocity for a lossy transmission line is worth analyzing under a special case, which is given as

$$\frac{R}{L} = \frac{G}{C} \tag{2.34}$$

Discovered by Oliver Heaviside, under this condition the transmission line will have no dispersion, and the phase velocity will be the same as a lossless transmission line. This can be easily justified by substituting Eq. 2.34 to Eq. 2.17, finding out the expression for β and then solving v_p using Eq. 2.22.

With all the above analysis, Table 2–1 summarizes the expressions for Z_0, v_p, γ, α, and β for both lossy and lossless transmission line.

2.1.2 Terminated Transmission Line

Consider a transmission with length a and Z_0, terminated with an arbitrary load Z_L, as shown in Fig. 2–2. The arrow indicates the conventional positive direction

Table 2–1: Summary of some important transmission line parameters

	Z_0	v_p	γ	α	β
Lossless	$\sqrt{\frac{L}{C}}$	$\frac{1}{\sqrt{LC}}$	$\omega\sqrt{LC}$	0	$\omega\sqrt{LC}$
Lossy	$\sqrt{\frac{R+j\omega L}{G+j\omega C}}$	$\frac{1}{\sqrt{LC}}$ when $\frac{R}{L}=\frac{G}{C}$	$j\omega\sqrt{LC}(1+\frac{R}{j\omega L})^{0.5}\cdot$ $(1+\frac{G}{j\omega}C)^{0.5}$	$\frac{\sqrt{LC}}{2}\frac{RC+LG}{LC}$	$\omega\sqrt{LC}$

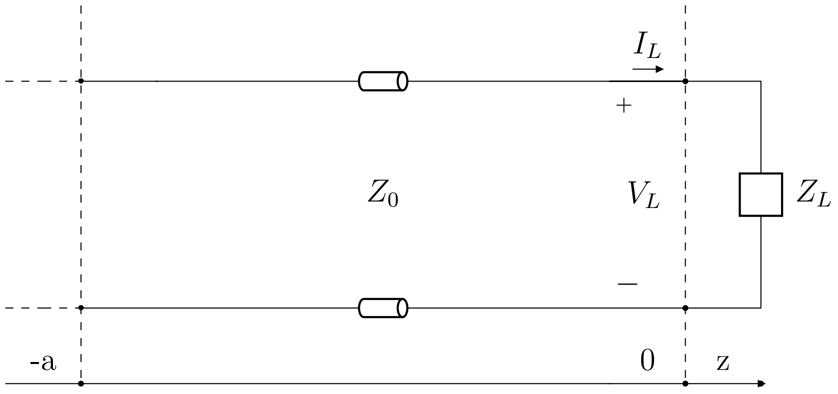

Figure 2–2: A transmission line terminated with an arbitrary load Z_L.

for the wave propagation. Therefore, $z = -a$ is the input of the transmission line, and $z = 0$ is the output.

Refer to Eq. 2.25, the reflection coefficient Γ at the load Z_L is defined as the ratio between the backward wave and forward wave at $z = 0$

$$\Gamma_L = \frac{V_z^- e^{\gamma(0)}}{V_z^+ e^{-\gamma(0)}} = \frac{V_z^-}{V_z^+} \tag{2.35}$$

The load impedance can be easily found by Ohm's Law at $z = 0$

$$Z_L = \frac{V(z=0)}{I(z=0)} \tag{2.36}$$

By substituting Eq. 2.25 and 2.27 to the above equation, Z_L can be rewritten as

$$Z_L = \frac{V_z^+ + V_z^-}{V_z^+ - V_z^-} \tag{2.37}$$

Substituting Eq. 2.35 to Eq. 2.37, Z_L can be expressed as

$$Z_L = Z_0 \frac{1 + \Gamma_L}{1 - \Gamma_L} \tag{2.38}$$

A more practical expression is found for Γ_L as

$$\Gamma_L = \frac{Z_L - Z_0}{Z_L + Z_0} \tag{2.39}$$

When Γ_L is zero, namely $Z_L = Z_0$, it is said that the load impedance is matched to the input as there is no reflected waves from the terminal.

Refer to Eq. 2.25 and 2.35, the load impedance at $z = -a$ is found by taking the ratio of the backward and forward wave at the point

$$\Gamma_{z=-a} = \frac{V_z^- e^{\gamma(-a)}}{V_z^+ e^{-\gamma(-a)}} = \Gamma_L e^{-j2\gamma a} \tag{2.40}$$

From Eq. 2.40, it can be seen that seeing from the load, an a long transmission line would cause a $2\gamma a$ phase difference from the termination to the input.

Similar to Eq. 2.36, the input impedance at $z = -a$ is found as

$$Z_{in}|_{z=-a} = \frac{V(z=-a)}{I(z=-a)} = Z_0 \frac{Z_L + jZ_0 tan(\gamma a)}{Z_0 + jZ_L tan(\gamma a)} \tag{2.41}$$

When the termination is short, namely $V(z = 0) = 0$ at $z = 0$ Therefore from Eq. 2.25

$$V_z^+e^{-\gamma(0)} + V_z^-e^{\gamma(0)} = V_z^+ + V_z^- = 0 \tag{2.42}$$

$$\Gamma_L = \frac{V_z^-}{V_z^+} = -1 \tag{2.43}$$

The input impedance at $z = -a$ can be easily found by making $Z_L = 0$ in Eq. 2.41, which gives

$$Z_{short}|_{z=-a} = jZ_0tan(\gamma a) \tag{2.44}$$

When the termination is open, namely $I(z = 0) = 0$ at $z = 0$. Therefore from Eq. 2.27

$$\frac{V_z^+}{Z_0} - \frac{V_z^-}{Z_0} = 0 \tag{2.45}$$

$$\Gamma_L = \frac{V_z^-}{V_z^+} = 1 \tag{2.46}$$

The input impedance at $z = -a$ can be easily found by making $Z_L = \infty$ in Eq. 2.41, which gives

$$Z_{open}|_{z=-a} = -jZ_0cot(\gamma a) \tag{2.47}$$

When the transmission line is with a quarter length of the wavelength $a = \frac{\lambda}{4}$ with a termination Z_L, the transmission line is called a quarter-wave transformer. Let $a = \frac{\lambda}{4}$ in Eq. 2.41, the input impedance is

$$Z_{quarter}|_{z=-a} = \frac{Z_0^2}{Z_L} \tag{2.48}$$

which is very useful for the impedance matching and biasing for microwave circuits. The quarter-wave transformer is also called impedance inverter, which will take the reciprocal of the load impedance. For example, when a DC voltage source is used for biasing an active component, it ideally has zero output impedance, which means it presents a short circuit and it is not useful to connect a short circuit directly across a transmission line. However, a quarter-wave transformer will invert a short circuit into an open circuit that has no effect on the signals on the line [36].

2.1.3 Scatter Parameters

In high-frequency domain, since the voltage and current are spatial and time variant, as shown in Eq. 2.11 and 2.12, it becomes almost impossible for measuring the voltage and current of a high-frequency system. Therefore, it is more convenient to analyze a high-frequency network from the concept of the wave, as the wave at any point is the summation of all forward and backward waves, which is easier for the measurement in the steady state condition. It introduces the terminology of Scatter Parameters or S-parameters.

Fig. 2–3 presents a two-port network the voltage waves as an example. The dashed lines are the reference planes where the analysis is conducted. S-parameters are defined as following

$$\begin{bmatrix} V_1^- \\ V_2^- \end{bmatrix} = \begin{bmatrix} S_{11} & S_{12} \\ S_{21} & S_{22} \end{bmatrix} \begin{bmatrix} V_1^+ \\ V_2^+ \end{bmatrix} \tag{2.49}$$

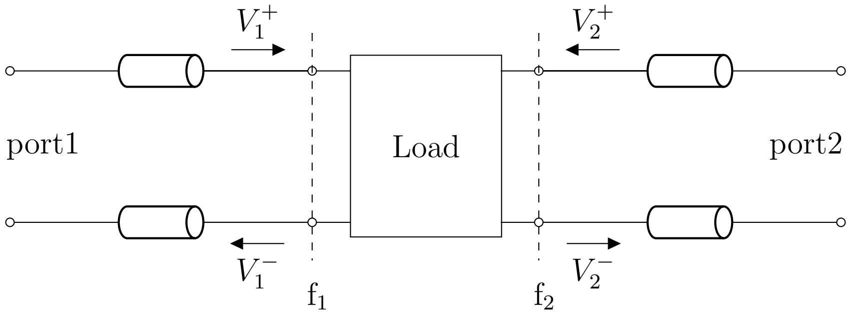

Figure 2–3: A two-port network, the dashed lines represent the reference planes, and the characteristic impedance of the transmission line is Z_0.

where S_{11}, S_{12}, S_{21}, and S_{22} the S-parameters. V_1^+ and V_2^+ are the incident waves to the load, and V_1^- and V_2^- are the reflected waves. S-parameters can be measured by matching a specific port then measuring the transmitted and reflected waves at the same port, or other ports if it is a multi-port network. To illustrate this, from Eq. 2.49

$$\begin{aligned} V_1^- &= S_{11}V_1^+ + S_{12}V_2^+ \\ V_2^- &= S_{21}V_1^+ + S_{22}V_2^+ \end{aligned} \tag{2.50}$$

By matching the load at port 2, namely making $Z_{L2} = Z_0$, the reflected wave V_2^+ from port 2 (incident wave to the load from port 2) is, therefore, zero by Eq. 2.39

$$S_{11}^-|_{V_2^+=0} = \frac{V_1^-}{V_1^+} \quad \text{for} \quad S_{21}^-|_{V_2^+=0} = \frac{V_2^-}{V_1^+} \tag{2.51}$$

Similarly, by terminating port 1 with a matched load $Z_{L1} = Z_0$, the reflected wave V_1^+ from port 1 (incident wave to the load from port 1) is therefore zero

$$S_{12}^{-}|_{V_1^+=0} = \frac{V_1^-}{V_2^+} \quad \text{for} \quad S_{22}^{-}|_{V_1^+=0} = \frac{V_2^-}{V_2^+} \tag{2.52}$$

S_{21} is also referred to as the gain of the load if it is active, or the insertion loss of the load if it is passive. S_{11} is sometimes also called the return loss.

It is worth mentioning the reciprocity property of a network. Considering apply a voltage V_1 at port 1 and a voltage V_2 is obtained at port 2. If then a voltage V_2 is applied at port 2 and a voltage V_1 is found at port 1, we conclude that this network is reciprocal, namely

$$S_{11} = S_{22} \quad \text{for} \quad S_{12} = S_{21} \tag{2.53}$$

2.2 Microstrip Line

2.2.1 Characteristic Impedance of Microstrip Line

The microstrip line is the most popular transmission line design due to its fabrication simplicity and its possible compatibility with the inkjet printing technology. Fig. 2–4 shows the cross-section view of a microstrip line and its field lines. W is the width of the conductive trace, d is the thickness of the dielectric substrate, and ϵ_r is the dielectric constant of the dielectric material.

It is desirable to use the TEM transmission line model to analyze the microstrip line due to simplicity. Nevertheless, the microstrip line does not support the pure TEM mode. The TEM wave consists of only one electric field component $\bar{E}$ and one magnetic field component $\bar{H}$, and their cross product is called Poynting vector $\bar{S}$ $[W/m^2]$ that indicate the direction of the energy flow. In this case, defining the

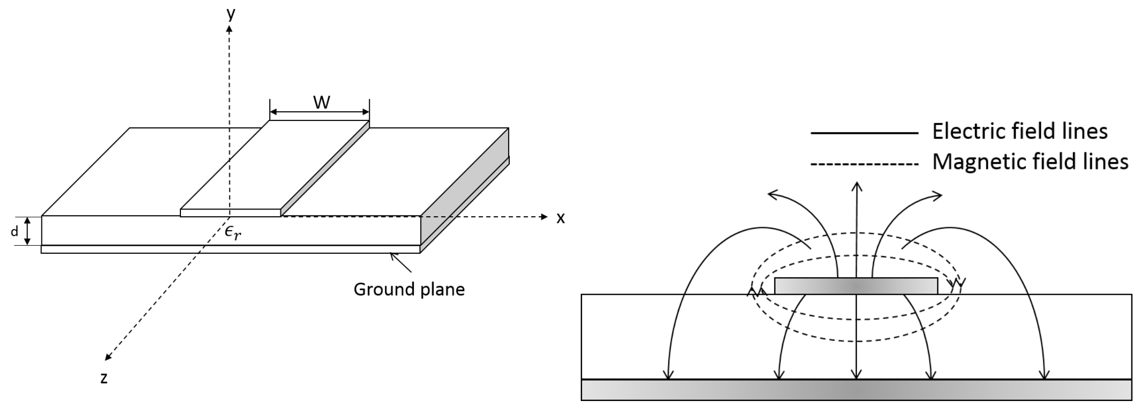

(a) (b)

Figure 2–4: Microstrip line with geometry (a) and field lines (b).

waves in Fig. 2–4 will be guided along the z direction, which is the same direction as the energy flow, therefore

$$\bar{S} = \bar{E} \times \bar{H} \tag{2.54}$$

is also pointing along the z direction, with $\bar{E}$ in y direction and $\bar{H}$ in x direction.

The TEM wave is the simplest type of propagating wave that can transmit the energy that consists of only two orthogonal field components. One requirement for this condition to be valid is that the waves have to travel within a homogeneous media. Without showing the math, it is known from the analogy of the sound that wave travels with different speed within different media. This is also true for electromagnetic waves, and it only travels in the speed of light in the vacuum environment. Without the derivation of the phase velocity from the perspective of electromagnetic waves for the sake of simplicity, it is defined as

$$v_p = \frac{c}{\sqrt{\epsilon_e}} \tag{2.55}$$

and

$$c = \frac{1}{\sqrt{\mu_0 \epsilon_0}} \tag{2.56}$$

where c is the speed of light, $\mu_0 = 4\pi \times 10^{-7}$ H/m is the absolute permeability constant, $\epsilon_0 = 8.854 \times 10^{-12}$ F/m is the absolute permittivity constant, and ϵ_e is the effective dielectric constant of the microstrip line since some of the field lines are in the dielectric region (grey area in Fig. 2–4) and some are in the air (white area in Fig. 2–4)

$$\epsilon_e = \frac{\epsilon_r + 1}{2} + \frac{\epsilon_r - 1}{2} \frac{1}{\sqrt{1 + 12\frac{d}{W}}} \tag{2.57}$$

Therefore, the waves in the air and in the dielectric region travel at different speed, and the microstrip line does not support the pure TEM mode. It is also true for the coplanar waveguide (CPW) that will be introduced later. But in reality, the dielectric substrates are usually very thin ($d \ll \lambda$), and the situation is approximated as the quasi-TEM mode that can be solved in the static case (DC), which neglect difference of the phase velocity in different media. Thus, the characteristic impedance is frequency independent (neglect the frequency variation of ϵ_r).

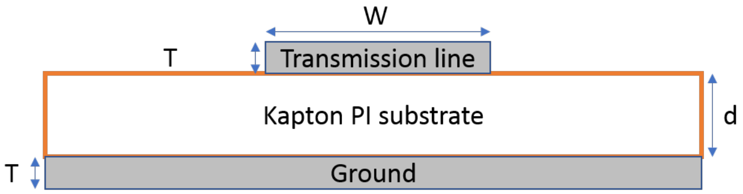

Figure 2–5: Printed microstrip line cross section view.

$$Z_0 = \begin{cases} \frac{60}{\sqrt{\epsilon_e}} ln(\frac{8d}{W} + \frac{W}{4d}) \quad \text{for} \quad W/d \leq 1 \\ \frac{120\pi}{\sqrt{\epsilon_e} W/d + 1.393 + 0.667 ln(W/d + 1.444)} \quad \text{for} \quad W/d \geq 1 \end{cases} \tag{2.58}$$

2.2.2 Printed Microstrip Line Design

With the synthesis equation for the characteristic impedance given, Fig. 2–5 shows the geometry of the printed microstrip line design. Table 2–2 shows the dimension of the microstrip line with a 50 Ω characteristic impedance. The S_{21} simulation and measurement results are plotted together in Fig. 2–6. A huge deviation between two results has been observed. This is primarily caused by the discontinuity between the soldering joint of the SMA connectors to the microstrip line, as shown in Fig. 2–7(a) highlighted in the red box. The SMA connector is with a 0.76 mm diameter pin, cold soldered by the silver epoxy to the microstrip line. Based on the dimension, this silver epoxy joint has been approximated by a 2 × 2 mm^2 conductive pad in HFSS, shown in Fig. 2–7(b).

The simulated S_{21} shows harmonics with a period of 3 GHz approximately, which is due to the periodically short and open of the transmission line, as shown in Eq.

Table 2–2: Dimension of printed microstrip line

W	T	d
250 μm	50 μm	127 μm

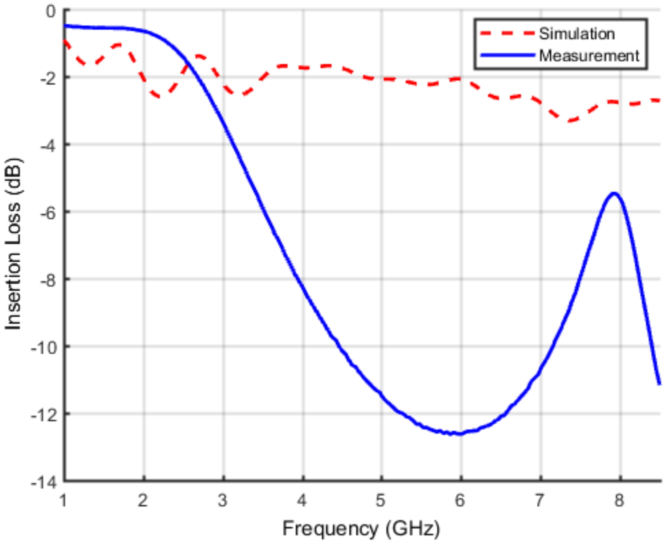

Figure 2–6: S_{21} simulation versus measurement without considering the silver epoxy joint.

2.41. This silver epoxy pad does not totally capture the impedance mismatch due to the discontinuity in the simulation, but a similar trend has been shown. The significance behind this is since the information is encoded as the notches created by the microwave resonators in the insertion loss response unless very large S_{21} attenuation is achieved, those resonances will be easily buried by the measured S_{21} in Fig. 2–6. The information will then be not recognizable. This is exactly what happened in [37]: a screen-printed microstrip line is coupled to several spiral resonators to create a frequency signature, and the tag is solder to the SMA connectors, which does not show any intended response. Therefore, it is reasonable to conclude that by removing this discontinuity, a smooth transition from the SMA connector to the microstrip line

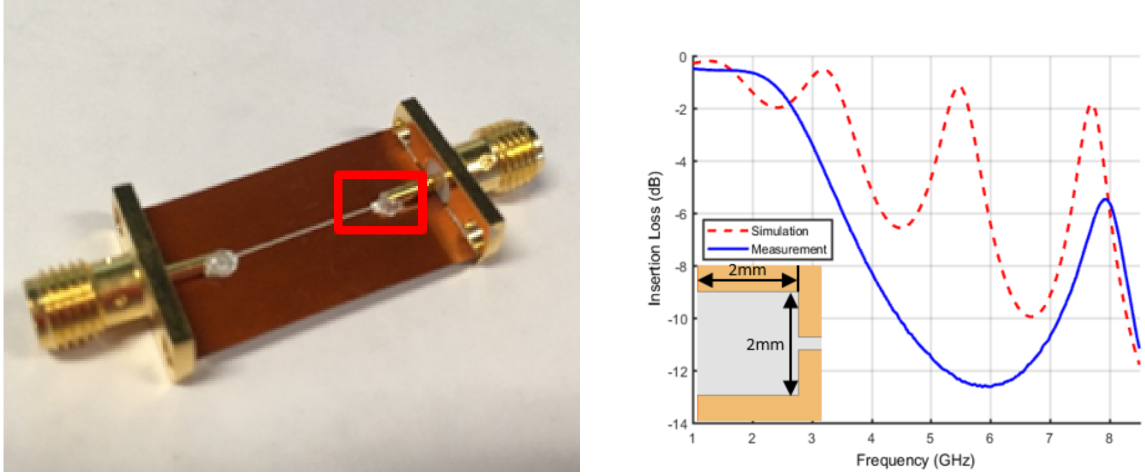

(a) (b)

Figure 2–7: (a) SMA connectors with the printed microstrip line. (b) S_{21} simulation versus measurement with the silver epoxy joint modeled

should reduce the loss. Nevertheless, the pin size of the SMA connector is 3 times as the microstrip line that will create a discontinuity step. It is only possible to greatly solve this issue by using connectors whose size is even smaller than the microstrip line. This could be achievable by using end-launch connectors that do not even require any soldering as the connection is achieved by the mechanical coupling. However, as it will be presented later, the biggest challenge is the coupling between the resonators and the microstrip line. Since 250 μm is almost the finest resolution supported by the printer, the uniformity of the printing process is questionable as it is always better to leave some margin to ensure the printing accuracy.

2.3 Coplanar Waveguide (CPW)

2.3.1 Characteristic Impedance of CPW

As noted in the previous section, to achieve a 50 Ω characteristic impedance system, a flexible printed microstrip line will have a very fine resolution requirement

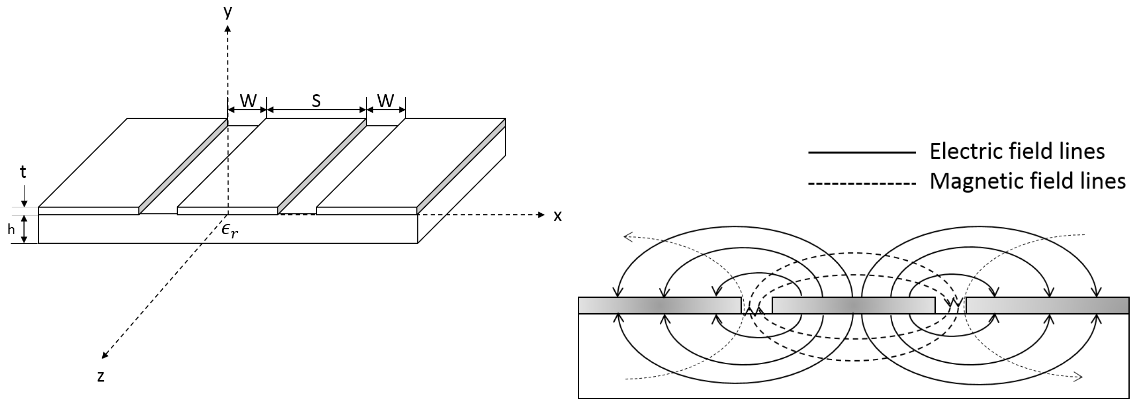

(a) (b)

Figure 2–8: (a) Geometry of CPW. (b) Electromagnetic field distribution.

for the printer that makes the printing accuracy questionable [38], which motivates us to use the CPW structure. CPW is first proposed by Wen [39] as a coplanar transmission line topology, which has been successfully applied in multiresonator based chipless RFID [13] tags through PCB fabrication techniques. Fig. 2–8 shows the geometry and field distributions of a CPW. The CPW consists of two slots and each is with W that isolate the signal path S to the ground. As noted that CPW is not a waveguide but a transmission line topology since it is a two-conductor structure, and the dominant mode is quasi-TEM, which is because of the same reason as the microstrip line: waves travel within two different media, with $\bar{E}$ and $\bar{H}$ fields orthogonal to each other.

The derivation of the CPW characteristic impedance in [39] using the conformal mapping assumes the substrate and the conductor thickness to be infinitely thick and thin, respectively. When the conductor thickness (metallization) is comparable to the substrate ($t = 50$ μm and $h = 127$ μm in Fig. 2–8(a)), it is necessary to revise the formulation for the CPW characteristic impedance. This is because it has been observed that the increase of the metallization would cause a decrease of the effective dielectric constant ϵ_e and the characteristic impedance Z_0. This can be intuitively explained from the observation that a higher metallization thickness gives rise to an additional concentration of the electric field between the slots [40, 41, 42]. Considering a conventional CPW transmission line on a dielectric substrate with a finite thickness, its characteristic impedance can be derived as [43]:

$$Z_0 = \frac{30\pi}{\sqrt{\epsilon_e}} \frac{K^{'}(k_1)}{K(k_1)} \tag{2.59}$$

$$\epsilon_e = 1 + \frac{(\epsilon_r - 1)}{2} \frac{K(k_2)}{K^{'}(k_2)} \frac{K^{'}(k_1)}{K(k_1)} \tag{2.60}$$

An accurate expression of the ration $K(k)/K^{'}(k)$ [44]

$$\frac{K(k)}{K^{'}(k)} = \begin{cases} \dfrac{\pi}{ln(\dfrac{2(1+\sqrt{k^{'}})}{1-\sqrt{k^{'}}})} & \text{for} \quad 0 \leq k \leq 0.707 \\ \dfrac{1}{\pi} ln \dfrac{2(1+\sqrt{k})}{1-\sqrt{k}} & \text{for} \quad 0.707 \leq k \leq 1 \end{cases} \tag{2.61}$$

$$k_1 = \frac{W^{'}}{W^{'} + 2G^{'}} \quad \text{for} \quad k_1^{'} = \sqrt{1 - k_1} \tag{2.62}$$

$$k_2 = \frac{sinh(\pi W^{'}/4H)}{sinh(\pi(W^{'} + 2G^{'})/4H)} \quad \text{for} \quad k_2^{'} = \sqrt{1 - k_2} \tag{2.63}$$

where ϵ_r is the dielectric constant of the substrate, ϵ_{eff} is the effective dielectric constant, and $K(k)$ represents the complete elliptic integral to the corresponding

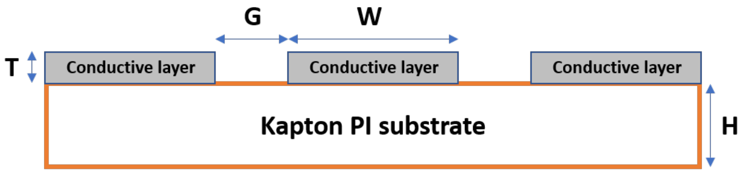

Figure 2–9: Printed CPW cross section view

modulus k. $W^{'}$ and $G^{'}$ are the modified width and gap after taking the effect of finite metallization thickness into account [45].

$$W^{'} = W + \Delta \quad \text{for} \quad G^{'} = G - \Delta \tag{2.64}$$

$$\frac{\Delta}{T} = \frac{1}{\pi}\left(4.089 + \left(0.9536 + 3.864 \times 10^{-3}(\frac{b}{T})\right)ln(\frac{4\pi G}{T})\right) \tag{2.65}$$

2.3.2 Printed CPW Design

Fig. 2–9 shows the cross-section view of the CPW transmission line used in our design, with its dimension summarized in 2–3. It can be seen that the signal path has a width of 5 mm, which is way above the supported printing resolution of the printer and therefore it could further ensure the printing accuracy compared with the printed microstrip line. Also, since its width is larger than the SMA connector epoxy joint, it does not suffer from the impedance mismatch issue. Moreover, in contrast to the microstrip line that the ground plane locates on another side of the substrate, noticing that the ground planes are aside from the signal path, which means that it does not require double-sided printing process, and therefore saving time and ink.

Table 2–3: Dimension of printed CPW

W	G	T	H
5 mm	0.3 mm	50 μm	127 μm

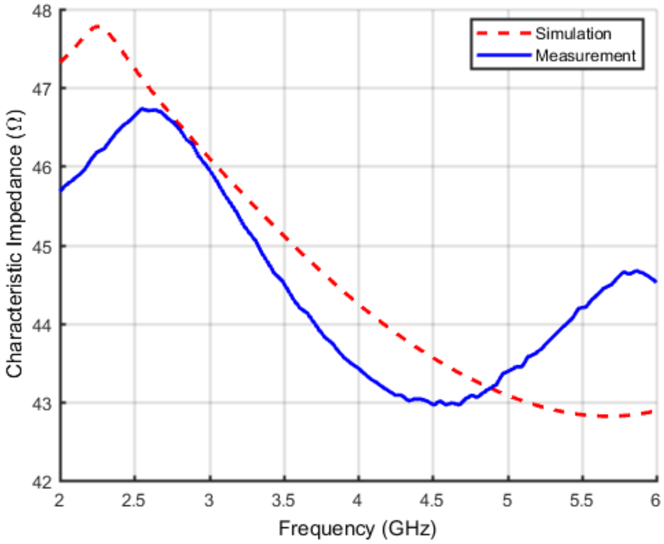

Figure 2–10: Simulated and Measured S_{21} response of the printed CPW deisgn.

The theoretical calculated Z_0 based on the dimensions in Table 2–3 is around 53 Ω at 4 GHz. To do so, since the two-port CPW line is reciprocal, it can be derived that [46] for a 50 Ω system

$$Z_{char} = Z_0 \sqrt{\frac{(1+S_{11})(1+S_{22}) - S_{12}S_{21}}{(1-S_{11})(1-S_{22}) - S_{12}S_{21}}} \tag{2.66}$$

Fig. 2–10 shows the simulated and measured S_{21} response of the printed CPW design. An average characteristic impedance of about 45 Ω has been achieved across the bandwidth of interest in both results, which slightly deviates to the analytic calculation. Besides the inaccurate printing process, since the vendor-provided electrical properties of the substrate and the conductive ink are both measured in low frequency, it is reasonable to see some tolerable deviations. With the advantages of CPW mentioned in this section, it is therefore concluded that CPW is more printing-friendly than the microstrip line.

2.3.3 Printed Modified CPW Bend Design

To integrate two UWB antennas in a cross-polarized fashion on the tag later, the CPW bend is required. A common but not optimized method is the right-angle bend used in [13]. However, unlike the regular copper cladding, the lossy conductive ink and the thick conductive layer lead to a lot of losses in the simulations with this structure. This is primarily caused be the slotline mode excitations within the CPW bend due to the unequal traveling distances of the waves. To mitigate this issue, the 90^o circular bend with a novel slow-wave compensation structure [47] is applied in the design to decrease the losses, which does not need extra components and materials like other compensation methods such as wire-bond techniques or dielectric overlay techniques.

Three common CPW bend structures are shown in Fig. 2–11. The dashed squares outline the region of interest for the analysis. In each structure, the outer and inner slots are denoted as L_1 and L_2, respectively. To maximally mitigate the slotline mode excitations, it is desirable to make the outer/inner slot length ration to approach to the unity, namely $L_1/L_2 \rightarrow 1$. In contrast to right-angle bend, it is well-known that the 90^o circular bend does provide a smaller slot length ratio and thereby has a better suppression on the slot-line mode than the right-angle bend.

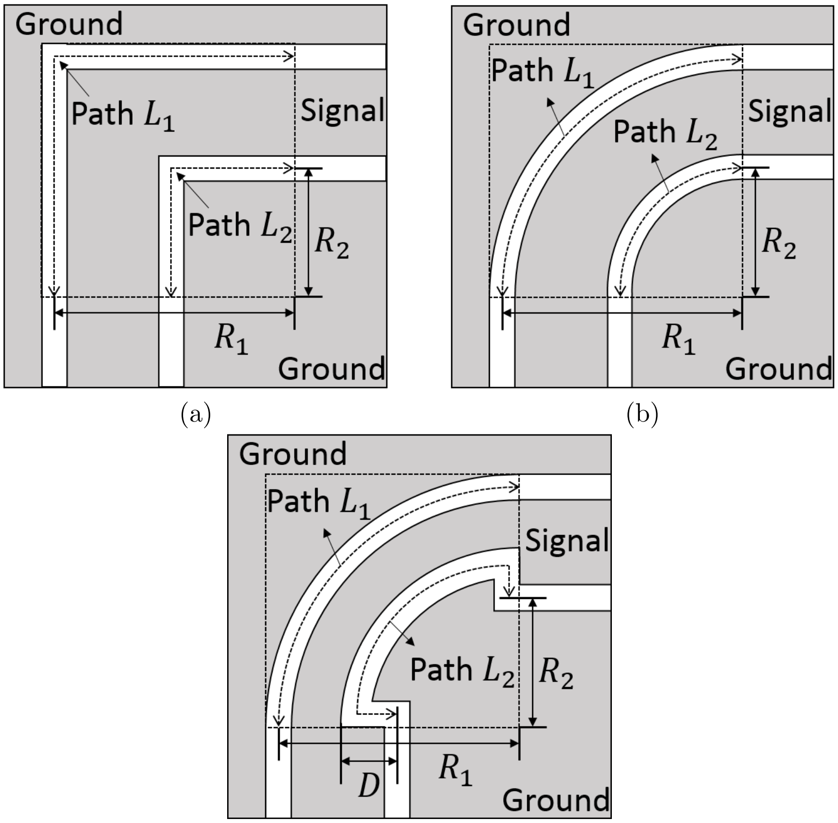

(a) (b)

(c)

Figure 2–11: (a) Right-angle bend. (b) 90^o circular bend. (c) 90^o circular bend with slow-wave compensation $D = 2.65$ mm used in the design. The dimensions of the transmission line are the same as in Fig. 2–5. For (b) and (c), the outer and inner radius are $R_1 = 9.615$ mm and $R_2 = 15.15$ mm, respectively, calculated as the effective radius.

This has been validated through the HFSS simulation, presented in Fig. Fig. 2–12 in terms of the insertion loss response. To further suppress the slotline mode, we add a small step discontinuity $D = 2.65$ mm on the inner side on the circular bend to increase the length of L_2 and thereby lowering down the slot length ration. The simulation result justifies the improvement from the pure 90^o circular bend structure to this slow-wave compensation structure. The slow-wave compensation structure

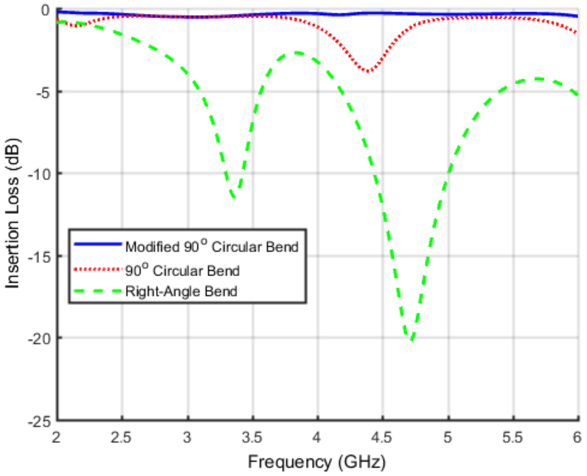

Figure 2–12: Simulated insertion loss response of three different CPW bends.

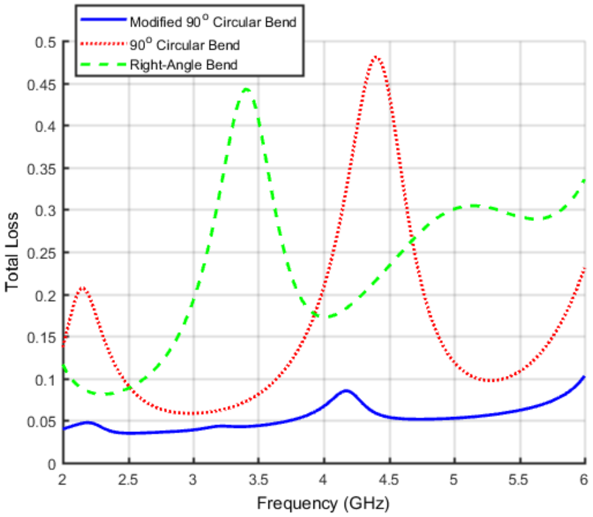

Figure 2–13: Total loss of three different CPW bends.

does not generate any resonance in the S_{21} response. This is also illustrated in Fig. 2–13, where the total loss is defined as

$$Total\ Loss = 1 - |S_{11}|^2 - |S_{21}|^2 \tag{2.67}$$

which is in the linear scale rather than dB. As anticipated, the slow-wave compensation also does provide a very small total loss compared to others.

CHAPTER 3
Printed Ultra-Wideband (UWB) Antenna

3.1 Microstrip Line UWB Antenna

The encoded frequency signature may occupy a large bandwidth that requires a UWB antenna to transmit the signal with a low loss. It is also desirable to have an omnidirectional antenna so that the reader antennas can more easily receive the signal from the tag. Therefore, the monopole UWB antenna is preferable. Recall the SMA connector issue with the microstrip line in Chapter 2 due to the silver epoxy joint, this will also cause the deviation between the simulation and measurement of the return loss. Fig. 3–1 shows the geometry of the printed circular monopole microstrip UWB antenna. It should be noted that the ground plane, colored in light grey, locates on the back of the substrate, and the dark grey color represents the top layer. G_{ant} is the gap between the background plane and the top circular patch, and the feed-line length is therefore equal to the sum of G_{ant} and L_{ground}. The ultra-wide bandwidth is achieved by optimizing G_{ant} and R_{ant}. Particularly, to achieve the optimized G_{ant} in the actual printing process, it is required to align the top layer and bottom ground plane with the aid of via that is the reference (not shown).

The via will be first mechanically drilled on the substrate that is similar to the idea of origin. The printer will ask the user to input the coordinate of the via by manually moving the printing nozzle to its location. The program will store it to the memory and then start printing. When the top layer is completed, the substrate has

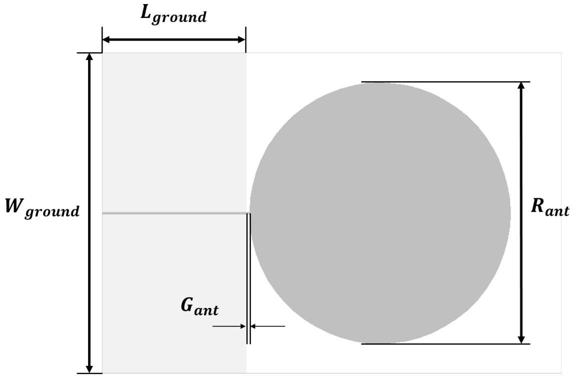

Figure 3–1: Geometry of the printed microstrip monopole UWB antenna. Colored in light grey is the ground plane that locates on the back of the substrate, and the dark grey color represents the top layer.

Table 3–1: Specifications of printed microstrip UWB Antenna

W_{ground}	L_{ground}	G_{ant}	R_{ant}	Bandwidth
40 mm	18.3 mm	0.4 mm	32.6 mm	4 GHz

to be flipped manually, and the same procedure as the top plane will be repeated. Afterward, the backplane will be aligned to the top plane.

Table 3–2 lists the optimized specifications of the printed microstrip UWB antenna. The above process involves many steps that would introduce inaccuracy. When using the nozzle to manually locate the position of the via, its precision completely depends on the eyeballs, leading to an inevitable offset. After flipping the substrate, the same procedure will be replicated, accumulating the same error. It will lead to an inaccurate G_{ant} that is simulated to be only 0.4 mm in this design. What is worse, with the silver epoxy at the connector considered, the S_{11} will deviate to the simulation result greatly.

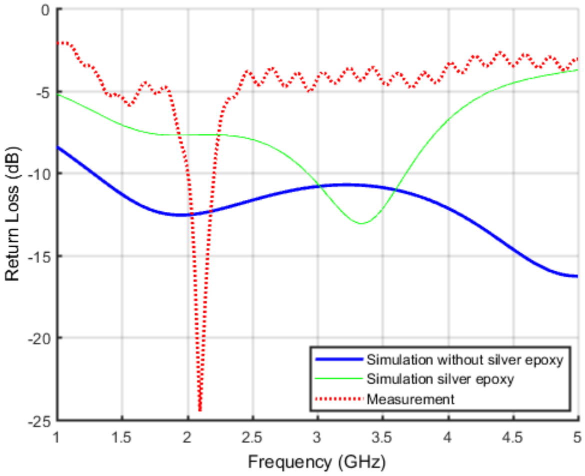

Figure 3–2: Simulated and measured return loss of the microstrip UWB antenna.

Table 3–2: Specifications of printed CPW UWB antenna

$W_{ellipse}$	$L_{ellipse}$	G_{ant}	W_{ant}	L_{ant}	Bandwidth
24 mm	35.6 mm	0.5 mm	15 mm	40.6 mm	4 GHz

Fig. 3–2 justifies this concern. Similar to Fig. 2–6, the silver epoxy is modeled by a 2×2 mm^2 pad at the input. This does not fully capture the mismatch effect as the joint is with an irregular shape and an uneven thickness. Somewhat, it shows that the epoxy joint destroys the S_{11} response and only a narrow bandwidth is below -10 dB around 3.3 GHz. In the measurement also a notch is found around 2.1 GHz, with a frequency shift compared with the estimated model. Nevertheless, it shows the idea of how the mismatch at the connector influences the measurement result. Again, with the end-launch connector with a smaller pin size might solve this issue, which is something the lab does not have at this moment.

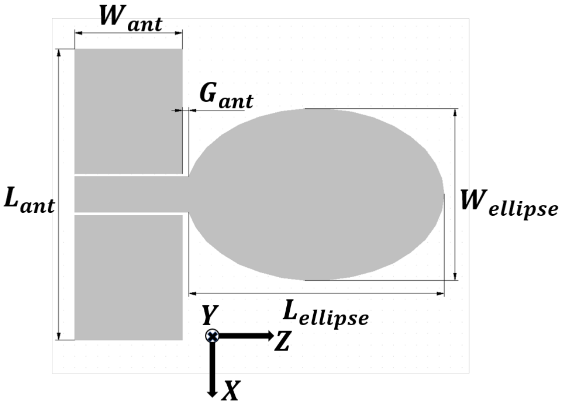

Figure 3–3: Geometry of the printed ellipse UWB antenna.

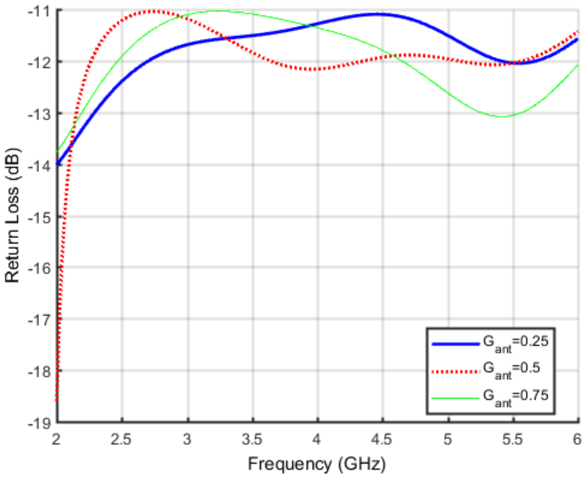

Figure 3–4: Parametric sweep of G_{ant} in millimeter.

3.2 CPW UWB Antenna

3.2.1 Design, Simulation and Measurement

Flexible printed CPW UWB antennas have been studied in [38]. It is shown that the ellipse-shaped planar structure has a better return loss response. In this design, the antenna aims at a 4 GHz bandwidth from 2 GHz to 6 GHz. Fig. 3–3 presents the

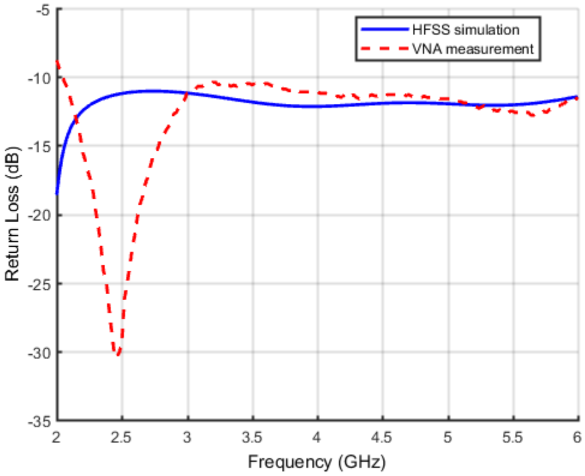

Figure 3–5: Simulated and measured return loss of the UWB antenna.

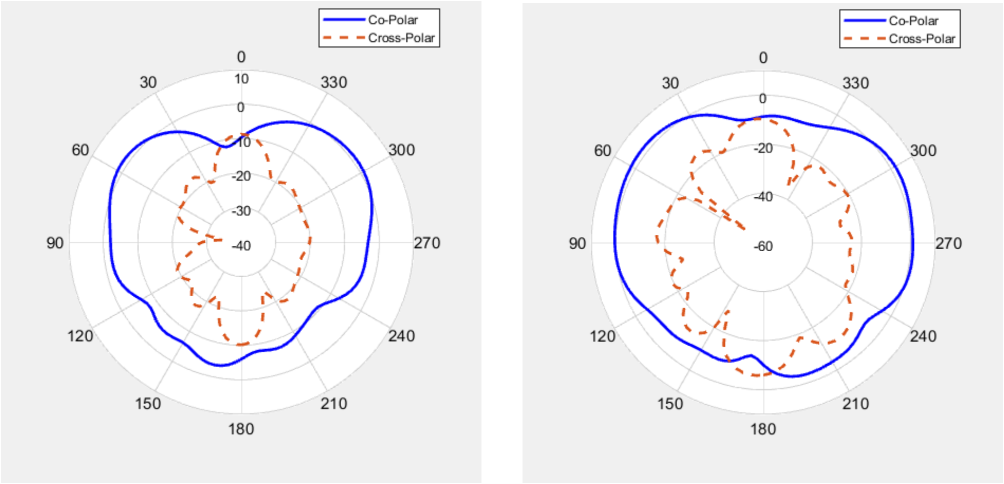

(a) (b)

Figure 3–6: Measured co-polar and cross-polar far-field radiation patterns of the UWB antenna at 4 GHz in the (a) XZ and (b) YZ plane.

layout of the inkjet-printed flexible UWB antenna design with its dimensions listed in Table 3–2.

It is remarked that the CPW UWB antenna is not only printing friendly since only one side of the substrate requires the ink deposition, but also provides better accuracy and consistency as it does not need the ground plane alignment as the microstrip line UWB antenna does. Also, it is very insensitive to the process variation, particularly the gap between the monopole and the ground plane. Fig. 3–4 shows the parametric sweep of G_{ant} while keeping other parameters the same. It can be seen that the return loss of the antenna, from G_{ant} = 0.25 mm to 0.75 mm, are consistently below the -10 dB rule of thumb [48].

The simulated and measured return loss of the antenna is shown in Fig. 3–5. Both plots are below the -10 dB rule of thumb across the bandwidth of interest. A simulated return loss notch is found around 2 GHz that is outside the bandwidth of interests and therefore not totally shown. Thus, the deviation is majorly a frequency shift caused by similar reasons happen in the printed CPW design. Fig. 3–6 shows the simulated far-field radiation patterns of the UWB antenna at the central frequency 4 GHz, in both YZ and XZ planes. The UWB antenna demonstrates unidirectional radiation patterns in both planes, with a reasonable polarization purity as the cross-polar levels in both planes are greatly smaller than the co-polar levels.

3.2.2 Flexibility Test

It would be also important to measure the insertion loss of the printed flexible antenna to verify its performance when it is bent [49, 50]. Fig. 3–7 shows two types of bending tests in this measurement. The antenna is attached to a plastic cylinder with a radius of 21 mm. The bending direction is based on the coordinate system associated with the antenna in Fig. 3–3. Fig. 3–8 presents the S_{11} of the antenna

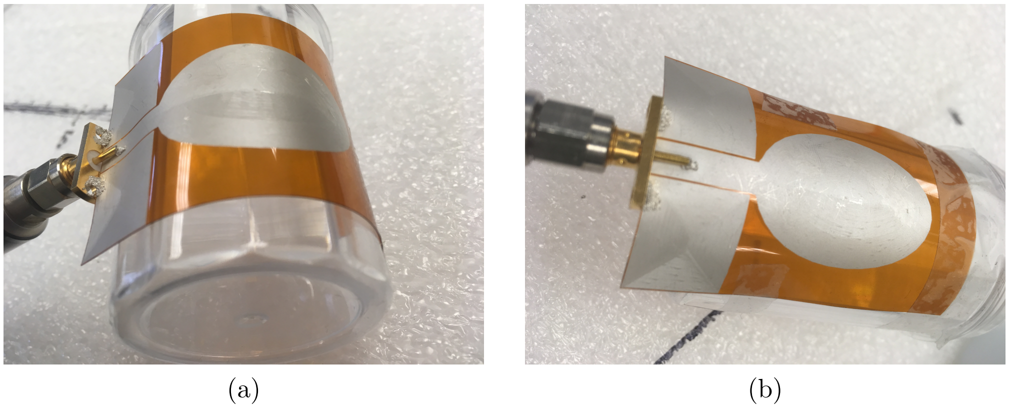

Figure 3–7: Bending test of the printed flexible CPW UWB antenna; (a) bending along the Z-axis and (b) bending along the X-axis.

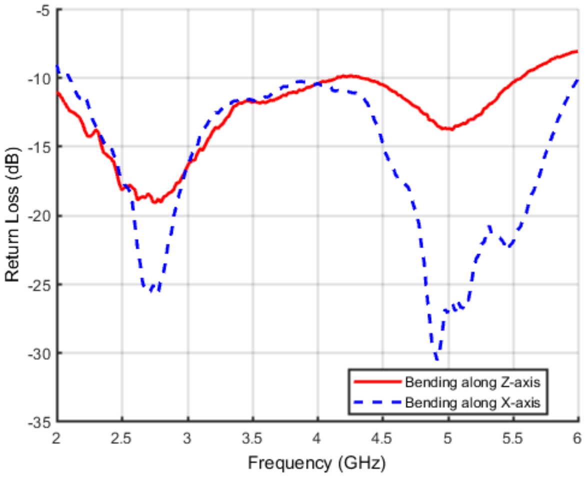

Figure 3–8: S_{11} of the printed flexible CPW UWB antenna in the bending test.

that experiences bending. As one can see, the bandwidth of the antenna does not alter hugely when it is bend, either along Z-axis or X-axis. A $|S_{11}| < -10$ dB has been almost achieved in both tests in the bandwidth of interest. In Fig. 3–7(a) the antenna suffers from more deformation than (b) that leads to a slightly smaller usable bandwidth, whose insertion loss is above -10 dB after 5.5 GHz. From the perspective of system integrity, this degrading is not significant. First, it will be a rare situation for the antenna to experience a great bending as 3–7(a). Second, since the UWB antennas will be connected to the multiresonator circuit, as long as the designed resonators do not generate any resonance beyond 5.5 GHz, the bending will not result in any critical issue.

CHAPTER 4
Printed Multiresonator Design

4.1 Microstrip Line Coupled Resonator

4.1.1 Microstrip Open-Loop Resonator

Inspired by [3], a microstrip line coupled to three square open-loop resonators is attempted. Fig. 4–1 shows the top layer of this design where all resonators are coupled to the microstrip line through a gap S, and all the line width is the same as $W = 250\ \mu$m in Fig. 2–4. The design dimensions are given in Table 4–2. It has been shown in [51], [52] that the open-loop resonator is essentially a $\lambda/2$ open-circuit resonator whose miniaturization is achieved bending it to an open-loop fashion.

From Eq. 2.55, the resonant frequency of an open-loop resonator is determined as

$$f = \frac{c}{2l\sqrt{\epsilon_e}} \tag{4.1}$$

where $l = \lambda/2$ is the total length of the open-loop resonator and ϵ_e is the effective dielectric constant in Eq. 2.55. Hamerstad and Bekkadal [53] point out that by bending the half-wave resonator to the open-loop topology, two open-ended discontinuities will form that contribute to an additional line length Δl at each end. This is because of the extra capacitance at the open end. The expression of Δl is [54]

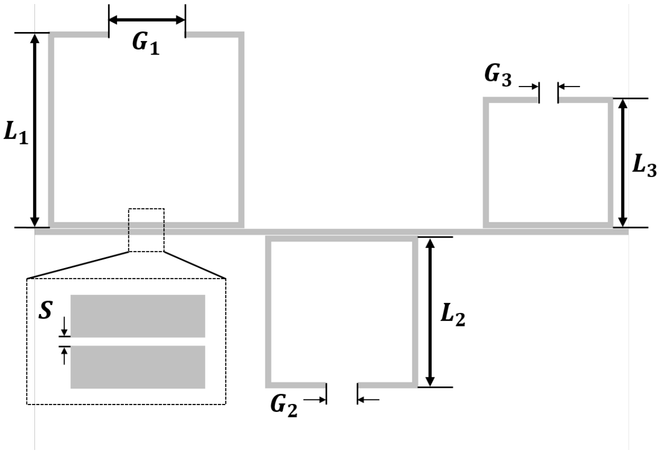

Figure 4–1: Microstrip line coupled open-loop resonators.

Table 4–1: Dimensions of printed open-loop resonators (all lengths are in millimeter)

L_1	L_2	L_3	G_1	G_2	G_3	S
9	7	6	3.5	1.5	1	0.05

$$\frac{\Delta l}{d} = 0.412 \frac{\epsilon_e + 0.3}{\epsilon_e - 0.258} \frac{W/d + 0.264}{W/d + 0.8} \tag{4.2}$$

where T and d can be found in Table 2–2. Therefore

$$l = 4L - G + 2\Delta l \tag{4.3}$$

Equivalently, a $\lambda/2$ resonator is a parallel RLC circuit with the conduction loss taken into the consideration. To calculate the resistance, it is first required to define the surface resistivity as [35]

$$R_s = \sqrt{\frac{\pi f \mu_0}{\sigma}} \tag{4.4}$$

where σ is the conductivity of the ink. The attenuation factor α_c due to the conduction loss is

$$\alpha_c = \frac{R_s}{Z_0 W} \tag{4.5}$$

where W is the width of the microstrip line. The wave number in the vacuum k_0 is defined as

$$k_0 = 2\pi f \sqrt{\mu_0 \epsilon_0} \tag{4.6}$$

where W is the width of the microstrip line. By relating Eq. 2.22 and 2.55, the relation between k_0 and β can be found as

$$\beta = \sqrt{\epsilon_e} k_0 \tag{4.7}$$

The attenuation factor due to the dielectric loss ($tan\delta$) is

$$\alpha_d = \frac{k_0 \epsilon_r (\epsilon_e - 1) tan\delta}{2\sqrt{\epsilon_e}(\epsilon_r - 1)} \tag{4.8}$$

The attenuation due to both conduction and dielectric loss is

$$\alpha = \alpha_c + \alpha_d \tag{4.9}$$

The resistance is therefore

$$R = \frac{Z_0}{\alpha l} \tag{4.10}$$

And the conductance as well as the inductance

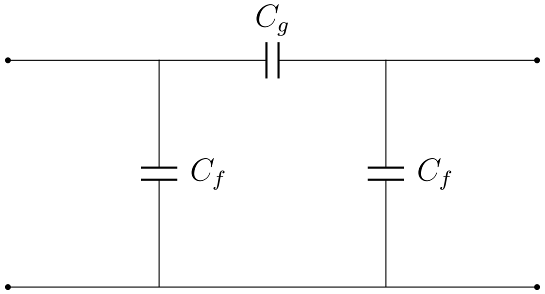

Figure 4–2: π network representation of the capacitance in the coupled microstrip line.

$$C = \frac{1}{4fZ_0} \tag{4.11}$$

$$L = \frac{1}{4\pi^2 f^2 C} \tag{4.12}$$

It is noted that, to fully extract the equivalent circuit in Fig. 4–1 is nontrivial if the coupled microstrip line segments are taken into account. Each open-loop resonator has one edge that is coupled to the microstrip line, and it will contribute to the gap capacitance and inductance. It can be found that the inductance in the coupled line structure, in this case, is negligible in the equivalent circuit model analysis due to its small value [55]. First, a π circuit representation of the capacitance in the coupled line structure is given in Fig. 4–2 that represents the E field coupling where C_f represent the fringing capacitance between the microstrip line and ground, and C_g is the capacitance between two coupled microstrip lines [55].

It is shown in [45] that for the analysis of coupled microstrip lines, even and odd mode capacitance are evaluated that relate to two impedance modes. Even-mode means two coupled microstrip lines are driven by the common-mode signal, whereas odd-mode suggest that two coupled microstrip lines are driven by the differential-mode signal. The superposition of these two modes will deliver a precious analysis on the capacitance. The even-mode capacitance is given as

$$C_{even} = C_p + C_f + C_f^{'} \tag{4.13}$$

where C_p is capacitance formed by the coupled lines with the ground plane. C_f is the fringing capacitance at the outer edge of the strip. $C_f^{'}$ is the modified fringing capacitance of one strip with the appearance of another one. C_p can be analyzed in analogy to the parallel plate capacitor

$$C_p = \frac{\epsilon_0 \epsilon_r W}{d} \tag{4.14}$$

C_f and is $C_f^{'}$ are defined as

$$C_f = \frac{\sqrt{\epsilon_e}/cZ_0 - C_p}{2} \tag{4.15}$$

$$\begin{cases} C_f^{'} = \dfrac{C_f}{1 + A(d/S)tanh(10S/d)} \\ A = exp(-0.1e^{2.33-2.53S/d}) \end{cases} \tag{4.16}$$

The odd-mode capacitance C_{odd} is defined as [36]

$$C_{odd} = C_{even} + C_{gd} + C_{ga} \tag{4.17}$$

where C_{gd} is the capacitance between two microstrip lines in the differential mode, and C_{ga} is the capacitance of the gap capacitance in the air between these two lines.

$$C_{gd} = \frac{\epsilon_0 \epsilon_r}{\pi} ln(coth(\frac{\pi}{4}\frac{S}{d})) + 0.65C_f(0.02\frac{\sqrt{\epsilon_r}}{S/d} + 1 - \frac{1}{\epsilon_r^2}) \tag{4.18}$$

$$C_{ga} = \epsilon_0 \frac{K(k^{'})}{K(k)} \tag{4.19}$$

where $K(k^{'})/K(k)$ can be found in Eq. 2.59. The total gap capacitance C_g for a length Δl combining even and the odd mode is [55]

$$C_g = -\frac{C_{even} - C_{odd}}{2}\Delta l \tag{4.20}$$

With all the value calculated, Fig. 4–3 shows the entire approximated equivalent circuit with a characteristic impedance $Z_0 = 50\ \Omega$. The Q-factor, or the unloaded Q-factor Q_0 for each parallel RLC circuit is

$$Q_0 = \frac{R_n}{2\pi f L} = \frac{\beta}{2\alpha} \tag{4.21}$$

where f_n is the resonant frequency of each resonator. In Fig. 4–3, the load of the equivalent circuit has been ideally modeled as $R_s = R_L = Z_0 = 50\Omega$. Neglect the coupled microstrip line gap capacitance C_g and fringing capacitance C_f, the loaded Q-factor Q_L is defined as

$$Q_L = \frac{Z_0}{2\pi f L} \tag{4.22}$$

To critically couple the resonators to the transmission line, it is required that

$$R = Z_0 \tag{4.23}$$

The coupling coefficient is defined as

$$g = \frac{Q_0}{Q_L} \tag{4.24}$$

The resonator is said to be critically coupled to the transmission line if $g = 1$. For illustration simplicity, if only the gap capacitance C_g is taken into account, then the input impedance for each coupled open-loop $\lambda/2$ resonator is

$$Z_{in} = -j(\frac{1}{2\pi f C_g} + Z_0 cot\beta l) \tag{4.25}$$

It has been shown that [35] when the resonance occurs, a gap coupled $\lambda/2$ resonator has an input resistance

$$R = \frac{Z_0 \pi}{2Q_0 b_c^2} \tag{4.26}$$

where $b_c = Z_0 2\pi f C_g$ is the normalized susceptance of C_g. For critical coupling, since $R = Z_0$

$$b_c = \sqrt{\frac{\pi}{2Q_0}} \tag{4.27}$$

And the required C_g to achieve the critical coupling is

$$C_g = \frac{b_c}{2\pi f Z_0} \tag{4.28}$$

For example, for the first resonator in Fig. 4–3, Q_0 is around 37.67, b_c is 0.2, and C_g is calculated around 0.254 pF, very close to the C_g value in Table 4–2 with the fact

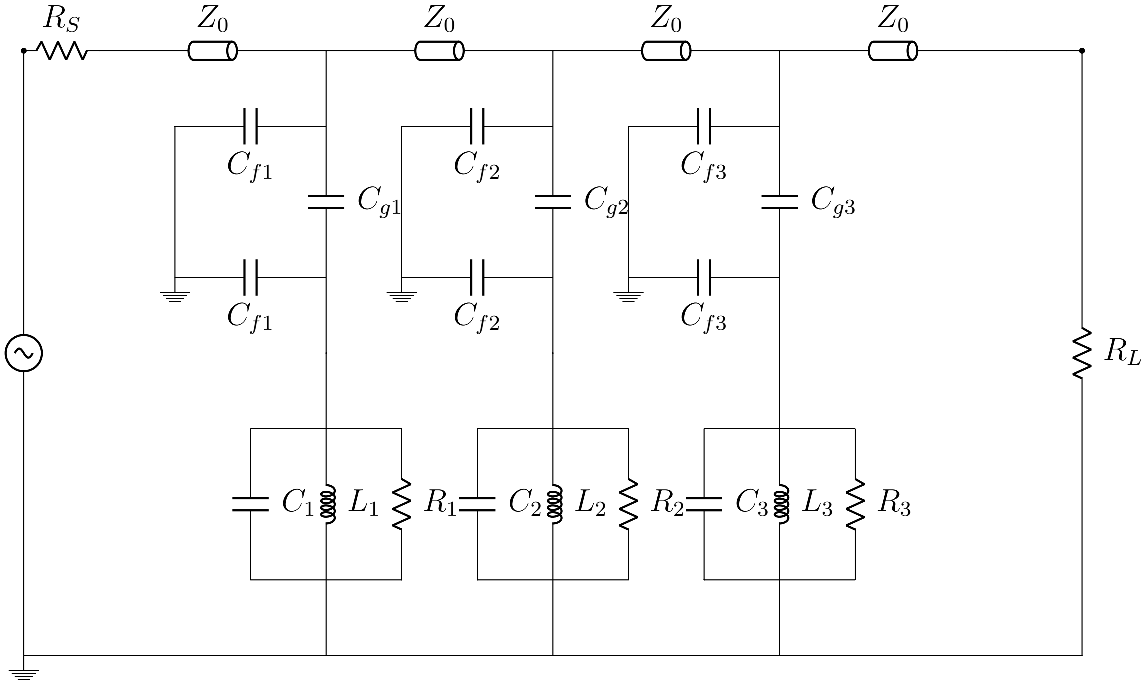

Figure 4–3: Equivalent circuit model of the open-loop resonator circuit in Fig. 4–1.

Table 4–2: Equivalent circuit value of printed open-loop resonators

R_s	R_L	C_{g1}	C_{g2}	C_{g3}	C_{f1}	C_{f2}	C_{f3}
50 Ω	50 Ω	0.187 pF	0.145 pF	0.125 pF	0.28 pF	0.22 pF	0.19 pF

C_1	C_2	C_3	L_1	L_2	L_3
1.77 pF	1.44 pF	1.25 pF	1.79 nH	1.46 nH	1.27 nH

R_1	R_2	R_3
1060 Ω	1163 Ω	1241 Ω

that C_f is neglected in this analysis. This would ensure the resonator could couple to the transmission line properly and maintain a high Q-factor.

It is noted that with the current inkjet printer, it is not achievable to print two lines with a gap $S = 50\ \mu$m. The aerosol jet printing facility at the University of Montreal supports up to 10 μ m feature size with a minimum spacing of 40μm between

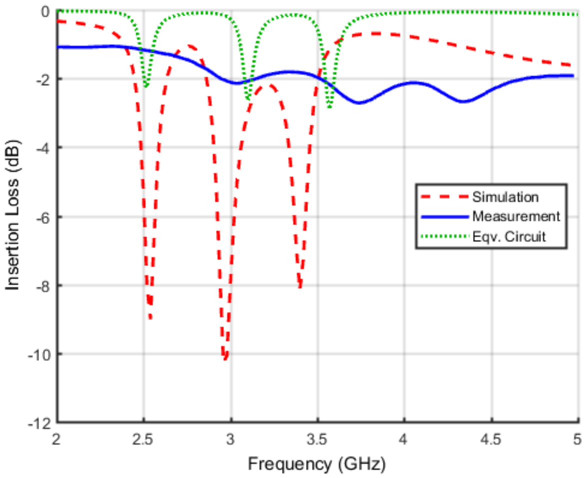

Figure 4–4: Insertion loss of the microstrip open-loop resonator circuit.

printed features. The conductive ink of the aerosol jet printer is found by the 4-point measurement with $\sigma = 1.25\times10^6$ S/m, surprisingly close to the one from Voltera. However, since the aerosol jet printing is a thin-film process (measured thickness is around 5 μm), this has to be taken into account when the simulation is conducted. To solve the SMA connector epoxy joint issue brought up in Chapter 2, the design has been tested in the RF/Microwave facility affiliated to CMC Microsystems at the University of Manitoba, where they have the probe station capable for measuring very small dimension microstrip lines.

Fig. 4–4 shows the S_{21} plots from the HFSS simulation, probe station measurement, and Advanced Design Studio (ADS) equivalent circuit simulation. It can be seen that the full-wave simulation result slightly deviates to the equivalent circuit model with an about 100 MHz frequency shift in the second and third resonances due to the coupling capacitance. The full-wave simulation also shows a deeper attenuation in all three notches. The depth of the notch is dependent on the resistance of each open-loop resonator. In the HFSS simulation, the resonators demonstrate higher resistance than the equivalent circuit model as it also captures other losses such as the fringing fields. Also as noted before, the electrical properties provided by the vendors on the conductive ink and flexible substrate are only measured at the low frequency, and the closed-form equations provided on the equivalent coupled microstrip lines circuit modal are approximations in a certain degree [45], [55]. Therefore, the equivalent circuit could fairly reflect the behavior of the printed open-loop resonator circuit in terms of the resonant frequency. Nevertheless, the measured result is hugely distinct to the other two plots. It is shown in [13] that the printed microstrip resonators show a poor coupling to the transmission line compared with printed CPW resonators in the measurement. Thus, the resonances are barely noticeable. However, the reason behind the frequency shift in the measurement is not very clear. This might be due to the aerosol jet printing process.

4.1.2 Microstrip Complementary Split-Ring Resonator (CSRR)

One of the primary problems happens in the microstrip open-loop resonator design, is the gap between the transmission line and coupled open-loop resonators, as shown in Fig. 4–1. As the excitation requirement, this gap S is made to be very small so that the resonator could be coupled to the transmission line better, which requires a higher resolution printing process such as the aerosol jet printing, which is very expensive and time consuming compared to the inkjet printing. The solution could be if the resonators do not couple to the microstrip line through the gap but

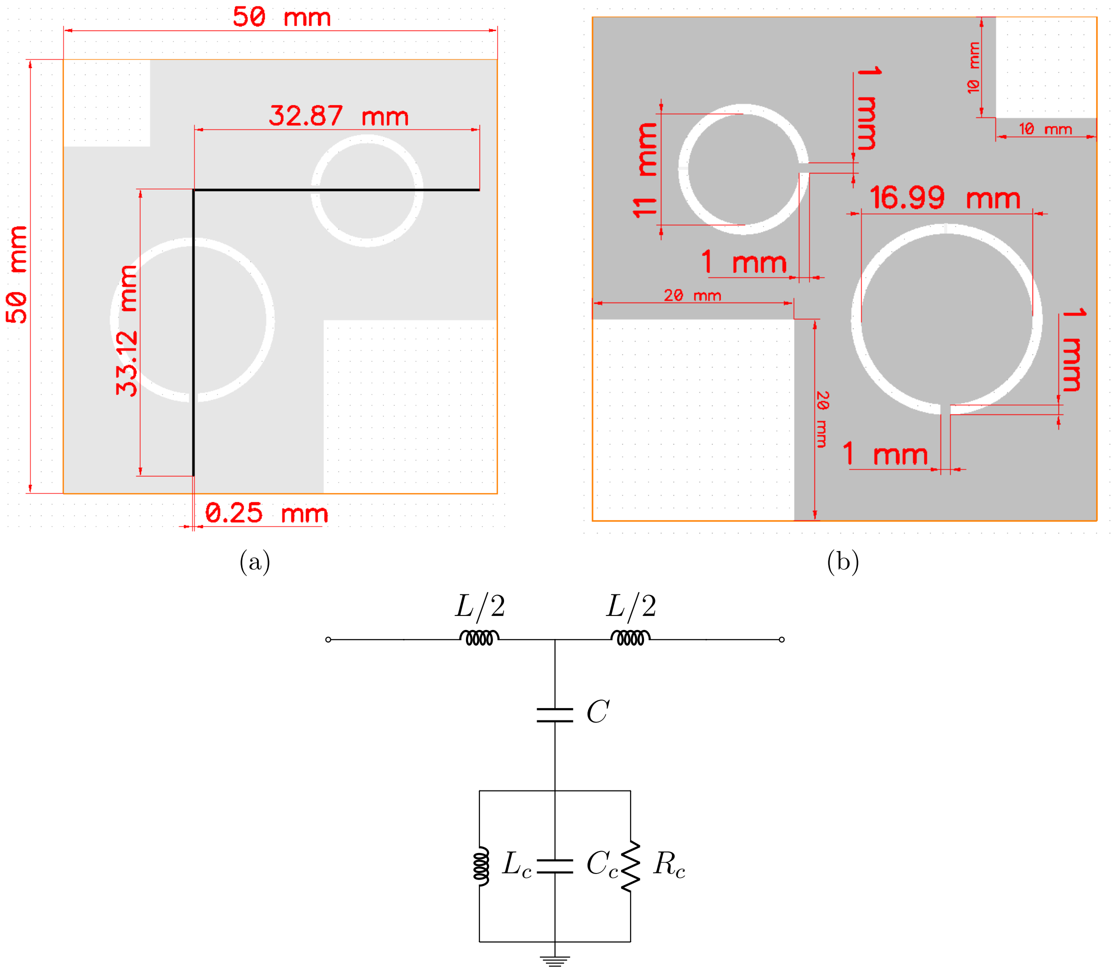

(a) (b)

(c)

Figure 4–5: Dimensions of the proposed design. The white colour represents the substrate and the grey colour represents the conductive layer; (a) the top plane, where the transmission line is aligned with the CSRRs at the ground plane in the center (the light grey colour shows the ground plane conductive layer); (b) the ground plane with the CSRRs; (c) equivalent circuit model for each CSRR.

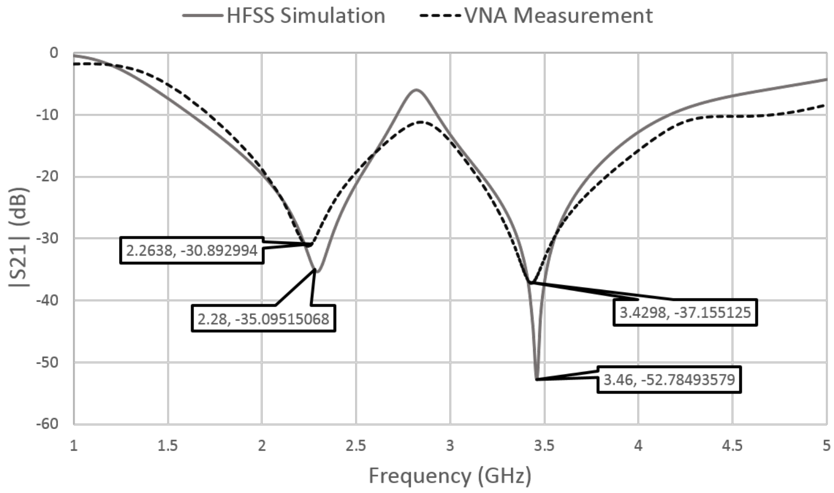

Figure 4–6: Insertion loss of the microstrip CSRR resonator circuit.

through the substrate, then the printing issue would be solved. Motivated by this thought, the complementary split-ring resonator CSRR topology is attempted.

As opposite to gap-coupled resonators, the CSRR is on the ground plane where an open-loop ring conductor is "etched" away, which suggests the term "complementary". The CSRR is a metamaterial element that has a negative effective permittivity. It has been found that by coupling CSRRs to the transmission line, stopbands at different resonant frequencies can be achieved [56]. The CSRR has been used in the liquid sensing in [23] where a microfluidic channel passes through one edge of the resonator. Since the microstrip line and resonators are now coupled through the substrate by the fringing field, the printing resolution requirement is relaxed.

Fig. 4–5(a) and (b) show the top and bottom planes of the printed CSRR circuit design, respectively. Two CSRRs with different size are aligned to the microstrip line to create two stopbands in the S_{21} plot [57]. The equivalent circuit model for the CSRR loaded microstrip line structure is in Fig. 4–5(c). L and C are the inductance and capacitance of the microstrip line, respectively. L_c is the inductance of the CSRR coming from the conductive path at the gap of CSRR. C_c is the gap capacitance caused by the "etched-away" ring-shape slot of the CSRR. R_c accounts for the equivalent CSRR loss [58]. The resonant frequency is

$$f = \frac{1}{2\pi\sqrt{L_c(C + C_c)}} \tag{4.29}$$

The quality factor of the resonance is

$$Q = R\sqrt{\frac{C + C_c}{L_c}} \tag{4.30}$$

Fig. 4–6 shows the simulated and measured insertion loss plots of the CSRR circuit. Unlike the open-loop resonator S_{21} plot in Fig. 4–4, the simulation and measurement results match to each other quite well. Moreover, the mismatch issue with the SMA connector is not observed in this case. This is because the CSRR creates a very deep attenuation at the stopband that conceals the loss due to the silver epoxy. However, since the conductive loss of the silver ink is the dominant cause of such a low Q-factor (as opposed to the open-loop resonator), two resonances occupy a very large bandwidth. It will be more beneficial to encode more information within a smaller bandwidth, this not only improves the efficiency of bandwidth utilization but also relaxes the design specifications of the UWB antennas at the primary and secondary sides.

4.2 CPW Coupled Resonator

4.2.1 Design, Simulation, and Measurement

In [8, 13], CPW with spiral resonators shows a good insertion loss response with a high Q-factor. Therefore, in contrast to the microstrip line coupled resonators, it is possible to encode more information within a certain bandwidth. As a result, it is also used in this study due to its printing easiness. Fig. 4–7 presents the layout of the resonator design with dimensions in Table 4–3. Three spiral resonators locate within the CPW transmission line to create a 3-bit spectrum signature. ADS is used to extract its equivalent circuit model from the HFSS simulation result based on the 3^{rd} order Chebyshev low pass filter prototype that is shown in Fig. 4–8 [59]. Its insertion loss response is plotted together with the HFSS simulation result and VNA measurement of the printed prototype design in Fig. 4–9. The resonances of the equivalent circuit can be calculated by

$$\omega_{res} = \frac{1}{\sqrt{L'_n C'_n}} \quad \text{for} \quad n = 1, 2, 3. \tag{4.31}$$

Depending on the topology (series and shunt) of the inductor and capacitor, the Q-factor of each resonance is [35]

$$Q_{series} = R_0 \sqrt{\frac{C'_n}{L'_n}} \quad \text{for} \quad n = 1, 3. \tag{4.32}$$

$$Q_{shunt} = R_0 \sqrt{\frac{L'_n}{C'_n}} \quad \text{for} \quad n = 2. \tag{4.33}$$

where

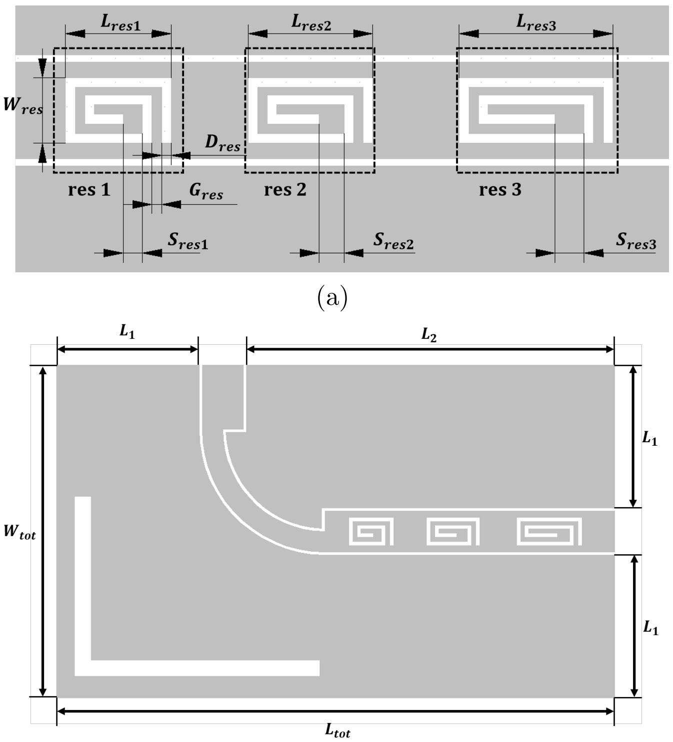

(a)

(b)

Figure 4–7: (a) Spiral resonator design, where the grey area is the conductive layer. (b) Layout of the multiresonator circuit. All resonators ("res 1", "res 2" and "res 3") are centered within the CPW. From left to right, the resonators are simulated to resonate at 5.1, 4.4 and 3.5 GHz, respectively.

$$L_n^{'} = \frac{R_0}{\omega_n \Delta C_n} \quad \text{and} \quad C_n^{'} = \frac{\Delta C_n}{\omega_n R_0} \quad \text{for} \quad n = 1, 3. \tag{4.34}$$

$$L_n^{'} = \frac{\Delta L_n R_0}{\omega_n} \quad \text{and} \quad C_n^{'} = \frac{1}{\omega_n \Delta L_n R_0} \quad \text{for} \quad n = 2. \tag{4.35}$$

For a 50 Ω system, $R_0 = R_4 = 50\ \Omega$; ω_n is the resonant frequency created by each corresponding LC circuit; Δ is the fractional bandwidth of the stopband; and

Table 4–3: Dimensions of printed CPW spiral resonators (all lengths are in millimeter)

L_{res1}	L_{res2}	L_{res3}	S_{res1}	S_{res2}	S_{res3}	W_{res}	D_{res}	G_{res}
5.5	6.5	8	1	1.3	1.5	3.4	0.5	0.5

L_1	L_2	L_{tot}	W_{tot}
17.4	45	68.2	40.6

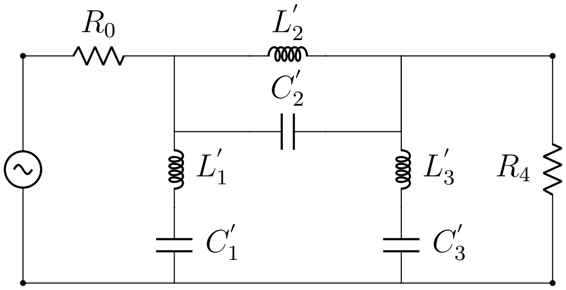

Figure 4–8: Equivalent lossless circuit model of the CPW coupled to the three resonators.

Table 4–4: Element values for maximally flat low-pass filter prototype

Order N	g_0	g_1	g_2	g_3	g_4
3	1	1	2	1	1

Table 4–5: Equivalent circuit value of printed CPW spiral resonators

R_0	R_4	$L_1^{'}$	$C_1^{'}$	$L_2^{'}$	$C_2^{'}$	$L_3^{'}$	$C_3^{'}$
50 Ω	50 Ω	132 nH	15.3 fF	89.8 pH	14.43 pF	113.7 nH	8.7 fF

the values for L_n and C_n are the Chebyshev coefficients that can be found in [60], presented in Table 4–4, where

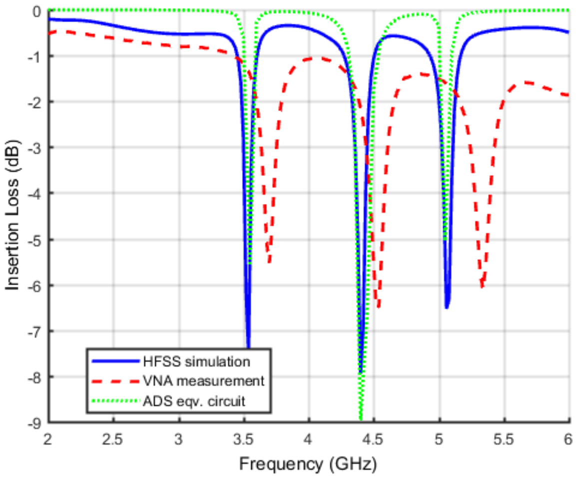

Figure 4–9: Insertion loss of the CPW coupled to the three resonators.

$$\begin{aligned}
g_0 &= \begin{cases} \text{generator resistance for voltage source} \\[1em] \text{generator conductance for current source} \end{cases} \\
g_k &= \begin{cases} \text{inductance for series inductors} \\[1em] \text{capacitance for shunt capacitors} \end{cases} \qquad \text{for} \quad k = 1 \text{ to } N. \\
g_{N+1} &= \begin{cases} \text{load resistance if } g_N \text{ is a shunt capacitor} \\[1em] \text{load conductance if } g_N \text{ is a series inductor} \end{cases}
\end{aligned} \tag{4.36}$$

The values for each equivalent circuit component are summarized in Table 4–5.

It can be seen that three plots are matching to each other properly, with some degree of deviations, with some tolerable deviations primarily caused by the imperfect printing process. The insertion loss of the equivalent circuit is very close to the HFSS simulation result, with generally higher Q-factors in the resonances as the loss is

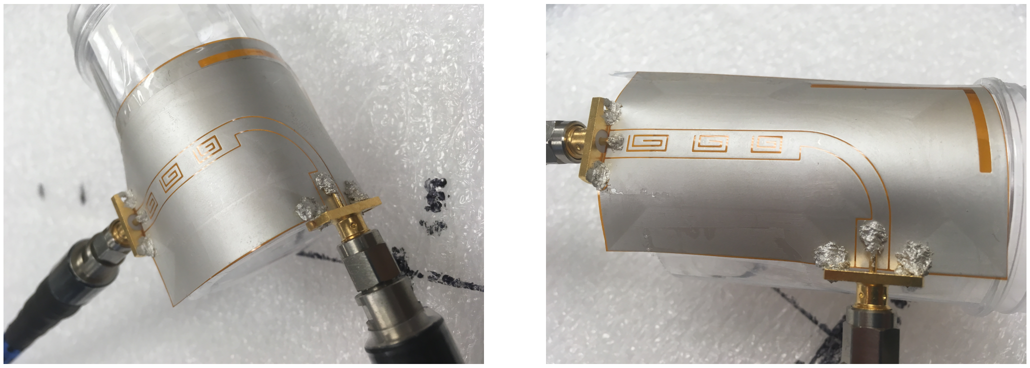
(a) (b)

Figure 4–10: Bending tests for the flexible printed CPW multiresonator circuit. (a) Bending along L_{tot}. (b) Bending along W_{tot}

neglected in the equivalent circuit model in Fig. 4–8 for the purpose of simplicity. The VNA measurement result deviates from the rest two plots obviously, with an about 200 MHz shift towards the higher frequency for each resonance. This is due to the imperfect printing process. When the ink is deposited on the substrate, it tends to spread to the blank area. Therefore, the D_{res} from Fig. 4–7 (a) will appear smaller on the printed tag than the designed value, leading to a resonance occurs at a slightly higher frequency. Three notches around 3.6, 4.5 and 5.3 GHz have been observed from the measurement that is generated by ”res 3”, ”res 2” and ”res 1”, respectively. Therefore, the resonant frequency increases with the dimension shrinkage of the resonator. Three resonances render a 3-bit spectrum signature. In contrast to microstrip resonators, CPW resonators show a higher Q-factor with great compatibility to the Voltera inkjet printer.

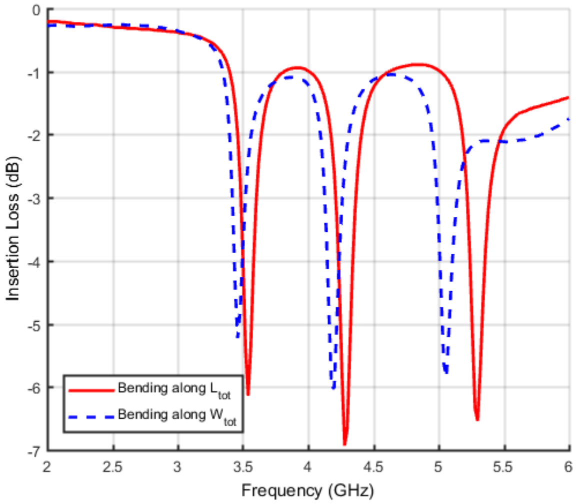

Figure 4–11: Insertion loss of the flexible printed CPW multiresonator circuit that experiences two different bending tests.

4.2.2 Flexibility Test

Similar to the bending tests for the CPW UWB antenna, the flexible printed CPW multiresonator circuit is bent along two directions, with respect to L_{tot} and W_{tot}, shown in Fig. 4–10. The multiresonator circuit is attached to the same plastic cylinder whose radius is 21 mm. The measured S_{21} plots are presented in Fig. 4–11. Two kinds of bending slightly cause the shift of the resonant frequencies due to the deformation of spiral resonators. Nevertheless, since the spiral resonators do not deform greatly in these two tests, their equivalent capacitance and inductance are not altered a lot. Resonances around 3.5, 4.3 and 5.4 GHz are observed. As noted before, all resonances are designed below 5.5 GHz, therefore the CPW UWB antennas will ensure the information transmission efficiency even when they are bent as Fig. 3–8(a).

CHAPTER 5
Reader Antenna Design

It is beneficial to choose directional high gain antennas for the reader so that it could interrogate the RFID tag in the ambient environment. A very wide antenna bandwidth is another requirement as the encoded information occupies a fairly large interval in the frequency domain, as can be seen in Fig. 4–9. In this design, the Vivaldi antenna is selected due to its high directional gain, wide bandwidth, and fabrication simplicity. The antenna substrate board is Rogers 3206 with $\epsilon_r = 6.15$, $tan\delta$ =0.0027, a dielectric thickness $H = 1.27$ mm, and a copper cladding $T = 17$ μm.

The proposed tapered slot antenna design methodology in [61] is adapted in this work. For a Vivaldi antenna, its size and desired bandwidth are correlated to the formula of the exponential taper, characterized by the Chebyshev multi-section matching transformer. Each transformer is denoted as x_n where $n \in [0, N]$ and $N+1$ is the number of transformers that will be used in the design to achieve the desired bandwidth. The width of each transformer is W_n. Fig. 5–1(a) shows the top plane of the Vivaldi antenna modeled by Chebyshev transformers. D is the circular cavity that improves the matching of the antenna [62], and L_s is recommended to be around

$$L_s = \frac{1}{4}\lambda_0 \tag{5.1}$$

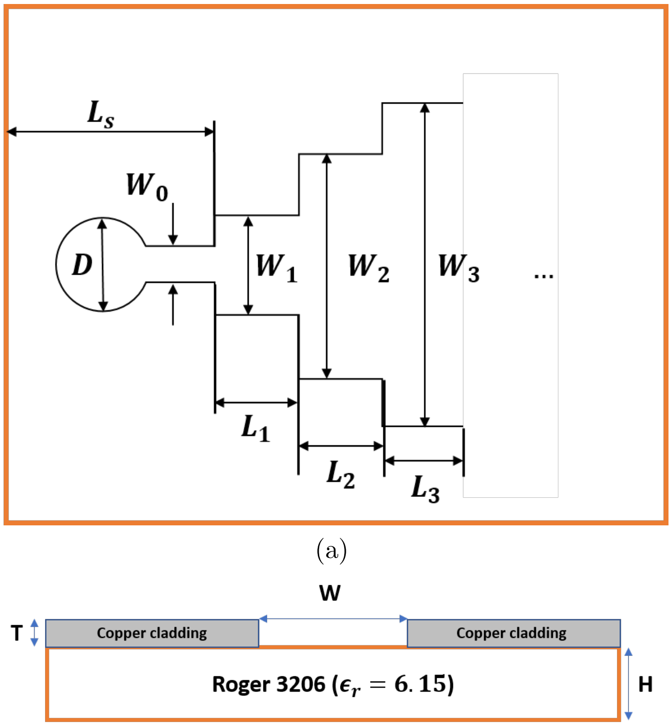

(a)

(b)

Figure 5–1: (a) Top plane of Vivaldi antenna modeled by Chebyshev transformers. (b) Cross-section view of each transformer, which is the slotline. $\epsilon_r = 6.15$, $H = 1.27$ mm, and $T = 17$ μm

where λ_0 is the wavelength of the centered frequency f_{avg}. Essentially, each transformer is a section of slotline, as shown in 5–1(b). The following design prcedure will be followed. First, assuming the desired bandwidth of the antenna is $[f_{lo}, f_{hi}]$, so the center frequency f_{avg} is

$$f_{avg} = \frac{f_{hi} + f_{lo}}{2} \tag{5.2}$$

The length of the initial transformer x_0 is calculated by solving the following equation

$$f_{lo} = 0.647 f_{avg} cos^{-1}(\frac{1}{x_0}) \tag{5.3}$$

Assuming Γ_m is the minimum tolerable reflection coefficient for each transformer (0.1 for instance), the Chebyshev polynomial is founded as

$$T_N(x_0) = \frac{Z_L - Z_0}{Z_L + Z_0} \frac{1}{\Gamma_m} \tag{5.4}$$

where $T_N(x_0)$ is the N-th order Chebyshev polynomial. In practice it is reasonable to assume the load impedance $Z_L \gg Z_0$ [61]. The value of N is then calculated by solving

$$x_0 = cosh(\frac{1}{N} cosh^{-1}(T_N)) \tag{5.5}$$

and

$$x_n = cos((2n-1)\frac{\pi}{2N}) \quad \text{for} \quad n = 1, 2, ..., N. \tag{5.6}$$

To find out the width of each transformer, it is required to calculate the characteristic impedance of each. First, the nth transformer phase is

$$\phi_n = -2cos^{-1}(\frac{x_n}{x_0}) \quad \text{for} \quad n = 1, 2, ..., N. \tag{5.7}$$

and

$$\omega_n = e^{j\phi_n} \quad \text{for} \quad n = 1, 2, ..., N. \tag{5.8}$$

ω_n is used to solve the following two equations simultaneously

$$\begin{cases} \sum\limits_{n=0}^{N} \Gamma_n \omega^n = \Gamma_n \prod\limits_{n=1}^{N} (\omega - \omega_n) \\ \sum\limits_{n=0}^{N-1} \Gamma_n = 1 \end{cases} \tag{5.9}$$

The first one is a polynomial equation of ω, and Γ_n can be solved by matching the coefficient of ω^n on both sides, together with the second equation. Finally, the characteristic impedance of each transformer is

$$Z'_{n+1} = \frac{1+\Gamma_n}{1-\Gamma_n} Z'_n \quad \text{for} \quad n = 0, 1, 2, ..., N-1. \tag{5.10}$$

Therefore, once Z'_0 is calculated, the impedance for all transformers can be solved recursively. Z_0 is frequency dependent, and since it is the first transformer that is also the transition from the microstrip line feed on the bottom plane to other Chebyshev transformers on the top plane, it is, therefore, bandwidth dependent [63]. To determine the value of Z'_0, first a term called -0.97 dB bandwidth v is calculated by solving

$$BW = \frac{\pi - tan^{-1} \dfrac{1}{1.272v}}{tan^{-1} \dfrac{1}{1.272v}} \tag{5.11}$$

where BW is the bandwidth of interest. For a system with a characteristic impedance Z_0

$$Z'_0 = Z_0 v \tag{5.12}$$

With the first slotline impedance $Z_0^{'}$ calculated, Eq. 5.11 can be solved iteratively. Finally, by using the closed-form equations of the slotline in [63], the width of each transformer W_n can be found by solving the following equation

$$\begin{aligned} Z_n^{'} &= 73.6 - 2.15\epsilon_r + (638.9 - 31.37\epsilon_r)(\frac{W_n}{\lambda_0})^{0.6} \\ &+(36.23\sqrt{\epsilon_r^2 + 41} - 225)\frac{W_n/H}{W/H + 0.876\epsilon_r - 2} \\ &+0.51(\epsilon_r + 2.12)(\frac{W_n}{H})ln(100\frac{H}{\lambda_0}) - 0.753\epsilon_r\frac{H/\lambda_0}{\sqrt{W_n/\lambda_0}} \\ &\text{for} \quad n = 0, 1, 2, ..., N. \end{aligned} \tag{5.13}$$

The next step is to calculate the length of each transformer L. In this design, all transformer lengths are identical, namely $L_1 = L_2 = ... = L_N = L$. Therefore, it is only necessary to calculate the length of the initial transformer L_0 even though it has emerged as a part of L_s, shown in Fig. 5–1(a). This is also because the initial transformer is the transition from the feedline to the antenna, which dominantly determines the frequency response of the design. The normalized wavelength $\lambda^{'}/\lambda_0$ is defined as

$$\begin{aligned} \frac{\lambda^{'}}{\lambda_0} &= 0.9217 - 0.277ln\epsilon_r + 0.0322\frac{W_0}{H}(\frac{\epsilon_r}{W_0/H + 0.435})^{0.5} \\ &-0.01ln(\frac{H}{\lambda_0})(4.6 - \frac{3.65}{\epsilon_r^2\sqrt{W_0/\lambda_0}(9.06 - 100W_0/\lambda_0)}) \end{aligned} \tag{5.14}$$

where $\lambda^{'}$ is the slotline guide wavelength for the slotline width before the first transformer L_1. Finally, the length for each transformer is

$$L = \frac{\lambda^{'}}{4} \tag{5.15}$$

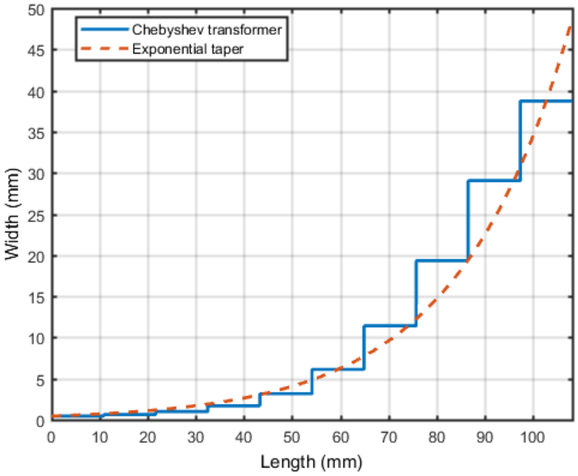

Figure 5–2: Exponential taper to smooth the Chebyshev transformers.

The total minimum required length of the antenna is therefore

$$L_{total} = \frac{\lambda'}{4}N + L_s \tag{5.16}$$

With a 4 GHz bandwidth of interest spanning from 2 to 6 GHz, W and L can be calculated for all transformers. Table 5–1 summarizes all critical calculated parameters in this design by following the above methodology. By smoothing the above Chebyshev transformers using the exponential curve equation, Fig. 5–2 shows the approximated exponential taper that smooths the Chebyshev transformers, where the exponential function is calculated as

$$y = 0.4913e^{0.0425x} - 0.0413 \tag{5.17}$$

With the exponential taper found, Fig. 5–3(a) shows the layout of the top plane of the design Vivaldi antenna.

Table 5–1: Summary of some critical parameters from the Vivaldi antenna design methodology

Eq.	Values
5.3	$x_0 = 1.062$
5.5	$N = 9$
5.6	$x_1 = 0.9848$, $x_2 = 0.866$, $x_3 = 0.6428$, $x_4 = 0.342$, $x_5 = 0$, $x_6 = 0.342$, $x_7 =$ -0.6428, $x_8 =$ -0.866, $x_9 =$ -0.9848
5.7	$\phi_1 =$ -0.7674, $\phi_2 =$ -1.2346, $\phi_3 =$ -1.8414, $\phi_4 =$ -2.4858, $\phi_5 =$ -3.1416, $\phi_6 =$ -3.7974, $\phi_7 =$ -4.4417, $\phi_8 =$ -5.0486, $\phi_9 =$ -5.5158
5.9	$\Gamma_0 = 0.0790$, $\Gamma_1 = 0.0807$, $\Gamma_2 = 0.1081$, $\Gamma_3 = 0.1298$, $\Gamma_4 = 0.1419$ $\Gamma_5 = 0.1419$, $\Gamma_6 = 0.1298$, $\Gamma_7 = 0.1081$, $\Gamma_8 = 0.0807$, $\Gamma_9 = 0.0790$
5.10 5.12	$Z_0' = 107.9\ \Omega$, $Z_1' = 126.53\ \Omega$, $Z_2' = 148.735\ \Omega$, $Z_3' = 184.78\ \Omega$, $Z_4' = 239.94\ \Omega$, $Z_5' = 319.28\ \Omega$, $Z_6' = 424.86\ \Omega$, $Z_7' = 551.66\ \Omega$, $Z_8' = 685.39\ \Omega$, $Z_9' = 805.65\ \Omega$

The next step is to design the microstrip-to-slotline transition to feed the signal to the antenna. Since the impedance of the slot line Z_0' has been calculated, the goal is to first find the characteristic impedance of the transition microstrip line Z_{mic}. Defining J, K, M and N parameters [64]

$$\begin{cases} J = \sqrt{\epsilon_r - (\frac{\lambda_0}{\lambda'})^2} \\ K = \sqrt{(\frac{\lambda_0}{\lambda'})^2 - 1} \\ M = \frac{2\pi JH}{\lambda_0} + atan(\frac{J}{K}) \\ N = cos(\frac{2\pi JH}{\lambda_0}) - cot(M)sin(\frac{2\pi JH}{\lambda_0}) \end{cases} \tag{5.18}$$

where H is the height of the dielectric. Z_{mic} is calculated by

$$Z_{mic} = N^2 Z_0' \tag{5.19}$$

Table 5–2: Equivalent circuit value of printed CPW spiral resonators (all lengths are in millimeter)

$W_{vivaldi}$	$L_{vivaldi}$	$S_{vivaldi}$	$D_{vivaldi}$	$R_{vivaldi}$
80	110	16	1.85	3

W_{bottom}	L_1	L_2	L_3	L_4	W_1	W_2	W_3	R_{stub}	α	β
58.52	14	3.24	10	11.2	1.88	1.08	0.31	6.33	90^o	70^o

which is the characteristic impedance corresponding to the section L_4 is Fig. 5–3(b). The next section will be a quater-wave transformer that transform a 50 Ω input to the microstrip-to-slotline transition. Its characteristic impedance $Z_{quarter}$ (L_2 and L_3 in Fig. 5–3(b)) can be easily calculated by Eq. 2.48

$$Z_{quarter} = \frac{Z_0^2}{Z_L} \tag{5.20}$$

Finally, a short section of $Z_0 = 50\ \Omega$ microstrip line L_1 completes the matching of the feedline. In addition, a 90-degree radial stub is used to conduct a broadband matching to decrease the loss [62]. Fig. 5–3(b) shows the feedline design of the antenna located on the backplane, and Table 5–2 lists all dimensions in Fig. 5–3. Some post-optimization have been done after the calculation to further improve the frequency response and accommodate the fabrication process, so the values in the table may slightly deviate to the above results.

Fig. 5–4 shows the measured co-planar and cross-polar radiation patterns of the designed Vivaldi antenna at 4 GHz. A near 30-dB gain difference has been achieved in the Z direction, allowing a good polarization purity and directivity. Fig. 5–5 shows the return loss and gain of the antenna along the Z direction across the

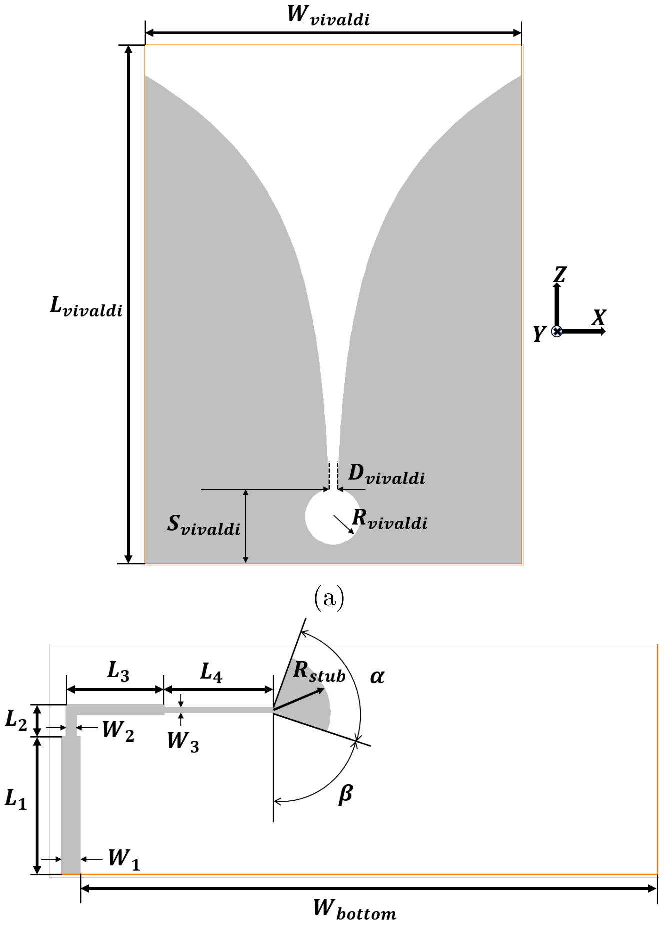

(a)

(b)

Figure 5–3: (a) Top plane of the Vivaldi antenna. (b) Bottom plane of the antenna with the microstrip-to slotline transition

bandwidth of interest. A more than 6 dB average gain and a return loss smaller than -10 dB have been achieved from 2 - 6 GHz.

Another metric to look at is the voltage standing wave ratio (VSWR) of the antenna, which is defined as

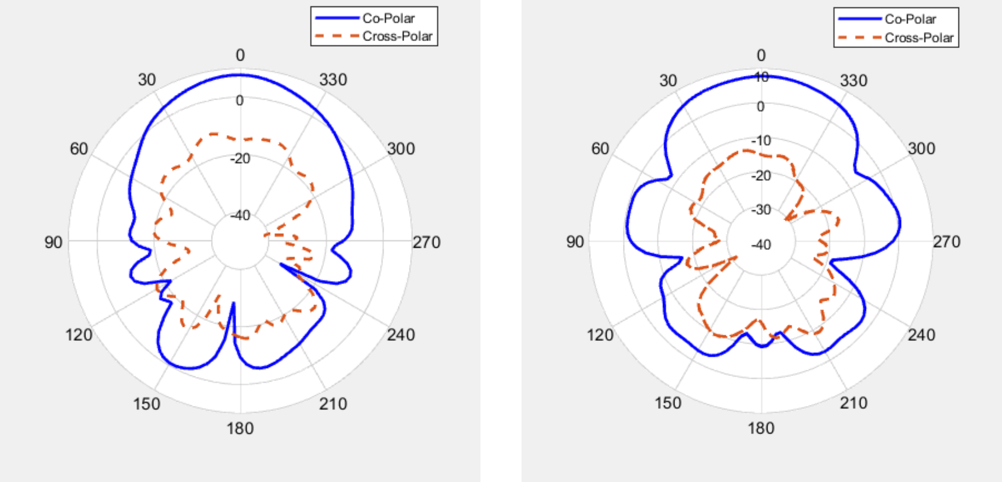

(a) (b)

Figure 5–4: Measured co-polar and cross-polar far-field radiation patterns of the Vivaldi antenna at 4 GHz in the (a) XZ and (b) YZ plane.

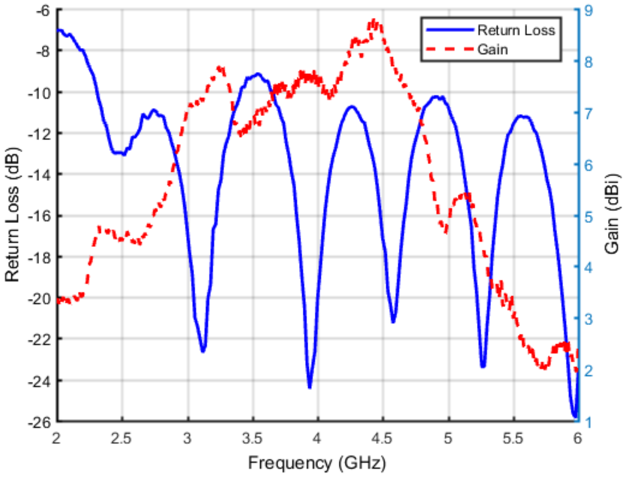

Figure 5–5: Measured return loss and gain of Vivaldi reader antenna.

$$VSWR = \frac{1 + |\Gamma|}{1 - |\Gamma|} \tag{5.21}$$

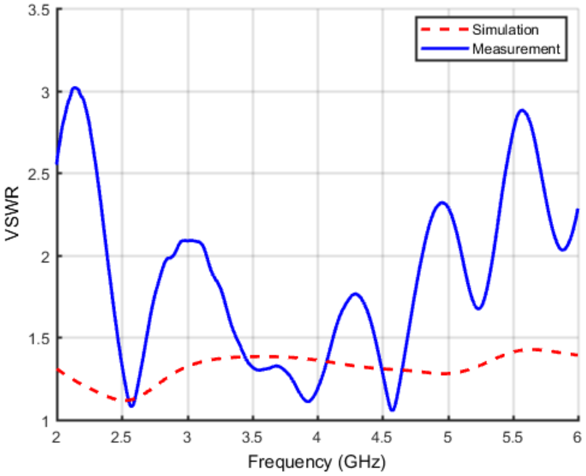

Figure 5–6: Simulated and measured VSWR of vivaldi antenna.

where Γ is the reflection coefficient at the port, and it is essentially the return loss S_{11}. A tolerable reflection coefficient has been selected as $\Gamma_m = 0.1$ at the beginning, which leads to an around 1.22 VSWR. Fig. 5–6 shows the simulated and measured VSWR of the designed Vivaldi antenna. In the simulation result, an average of 1.35 VSWR has been achieved across the bandwidth of interest that is very close to Γ_m. For the measurement result, however, an average of 2 VSWR is obtained from 2 - 6 GHz, with a more than 2.5 VSWR at the lower and higher bound of the bandwidth of interest. VSWR is the ratio of the peak amplitude of a standing wave to the minimum amplitude of a standing wave, and when the transmission line is not perfectly matched to the load, the transmitted power will be reflected back to the source. A VSWR = 2 is around 11.1 % power reflection. The RF power at the VNA is calibrated to -5 dBm and a maximum allowed power handling is 26 dBm. Therefore, it is important to maintain a lower VSWR value to protect the power source and transmission line. This deviation from the simulation result is hugely contributed by the fabrication progress. In this design, the antenna is fabricated using the mechanical milling process. The milling tip that the machine shop has, does not support a feature size that is smaller than 1 mm. As a result, W_3 has been measured as around 0.9 mm, which is 74 Ω. The characteristic impedance at the microstrip-to-slotline transition is very critical. Hence, a finer fabrication process will absolutely improve the VSWR of the antenna.

CHAPTER 6
CPW Flexible Printed Chipless RFID Tag and Concentration Measurements of Liquid Solutions

6.1 CPW Flexible Printed Chipless RFID Tag

The completed proposed printed chipless RFID tag is shown in Fig. 6–2. The size of the tag is not optimally compact but is adequate for some applications, such as logistic tracking and freshness sensing in food packages. To further shrink down the size of the tag, one can decrease the size of the resonators and UWB antennas to shift the bandwidth of the tag to the upper-frequency range. Additionally, one can decrease the area of the ground plane to an optimal size that does not change the resonances the tag.

The chipless RFID tag is tested in the ambient environment. Fig. 6–3 shows the testing setup. Two cross-polarized Vivaldi antennas are used to interrogate the tag that is distanced 5 cm away. The transmitting Vivaldi antenna is facing the receiving UWB CPW antenna on the tag, and the transmitting tag antenna sends back the encoded information to the receiving Vivaldi antenna. The insertion loss plot is generated and analyzed in the VNA, that is connected to two Vivaldi antennas. Fig. 6–1 shows the port-to-port isolation of two cross-polarized Vivaldi antennas. Usually, an about -40 dB insertion loss would ensure a good cross-polar

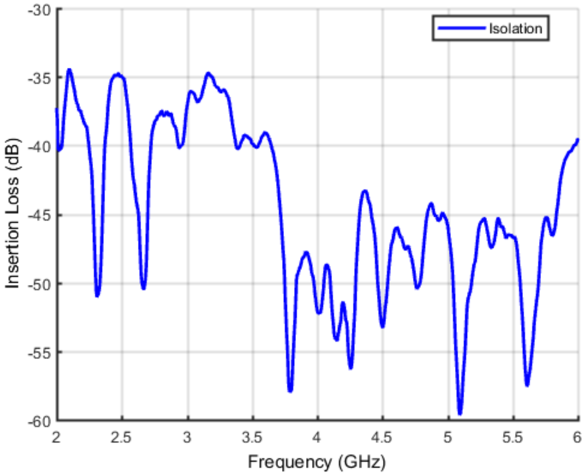

Figure 6–1: Port-to-port isolation between two cross-polarized Vivaldi antennas.

suppression that results in a good reading results [3]. It can be seen that two cross-polarized Vivaldi antennas achieve a more than 45 dB isolation across the bandwidth of interest.

The wireless measurement results of the tag are presented in Fig. 6–4. All plots are generated after subtracting the insertion loss response of the reference tag that is printed out separately without any resonators. The insertion loss of the reference tag is first registered in the memory of the VNA, then it is removed from the attached form board. The printed RFID is placed at the exact location where the reference tag was located, and the subtraction is done by the VNA. Therefore, the net insertion loss response is mostly contributed by the resonators. Resonators ”res 3”, ”res 2” and ”res 1” excite three notches around 3.6, 4.4, and 5.3 GHz, respectively, which are encoded as ”bit 0”, ”bit 1” and ”bit 2”.

Table 6–1: Wireless characterization of the printed flexible chipless RFID in 5 cm

Name	f_{res}	S_{21} (dB)
res 1	3.6	-1.5
res 2	4.4	-4.5
res 3	5.3	-4.2

To further verify the correspondences between resonators and notches, a copper tape is used to cover one resonator at a time. Initially, all resonators are uncovered, followed by covering the resonator ”res 1”, and then resonator ”res 3”. It can be seen that when ”res 1” is covered (shorted), the resonance at 5.3 GHz disappears, whereas the rest two resonances retained at their frequencies. The same phenomena is observed with ”res 3” covered: the resonance at 3.6 GHz vanishes while the rest two retain. With this idea, one has the freedom of encoding different 3-bit messages based on the appearance of notches. It should be noted that the net insertion responses of the resonators are above 0 dB at some frequencies, which is due to the imperfect subtraction from the reference tag that does not physically contribute to any gain. Table 6–1 summarizes the wireless characterization results of the printed flexible chipless RFID in 5 cm.

It is worth mentioning that since the tag is characterized in the ambient environment, and its conductive layer is lossier than the regular copper cladding used in microwave circuit boards. The tag is believed to demonstrate a longer reading range and a higher Q-factor with the resonance in the anechoic chamber. Compared with the RFID systems proposed in [3], this design in the ambient environment has demonstrated an adequate ability for information recognition in the same distance.

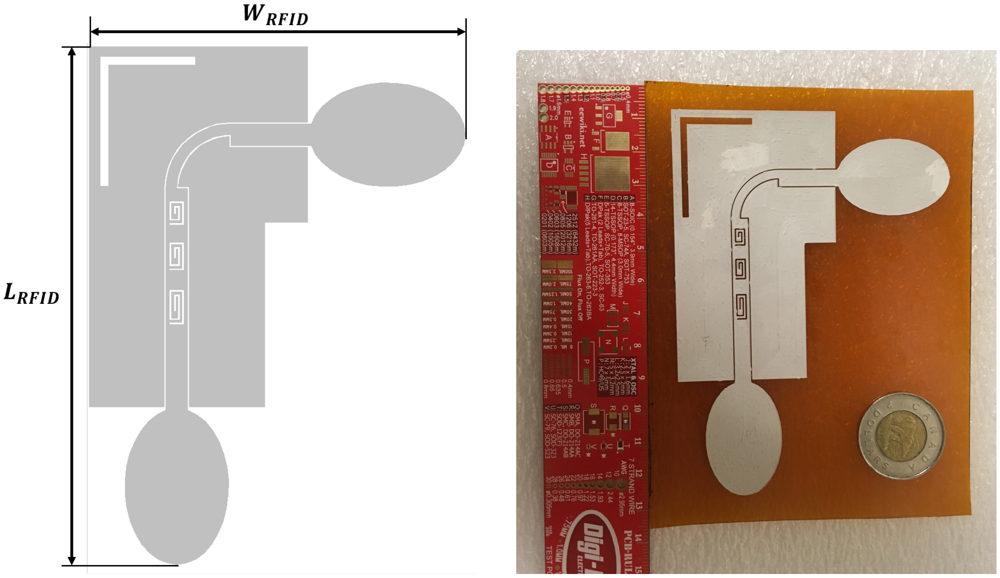

(a) (b)

Figure 6–2: (a) Geometry of the RFID tag with $W_{RFID} = 87.1$ mm, $L_{RFID} = 119.7$ mm. (b) The inkjet-printed flexible chipless RFID tag.

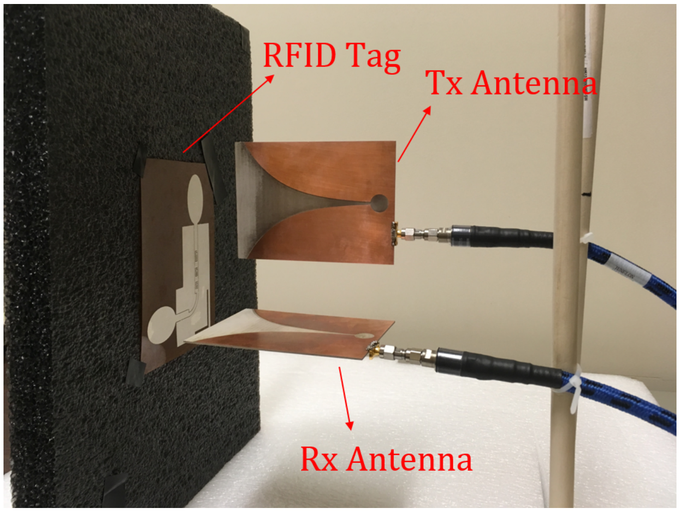

Figure 6–3: Wireless experiment setup for the chipless RFID tag at 5 cm.

When the distance is increased over 10 cm, the information in the insertion loss amplitude is not usable due to the impedance mismatch between reader antennas and

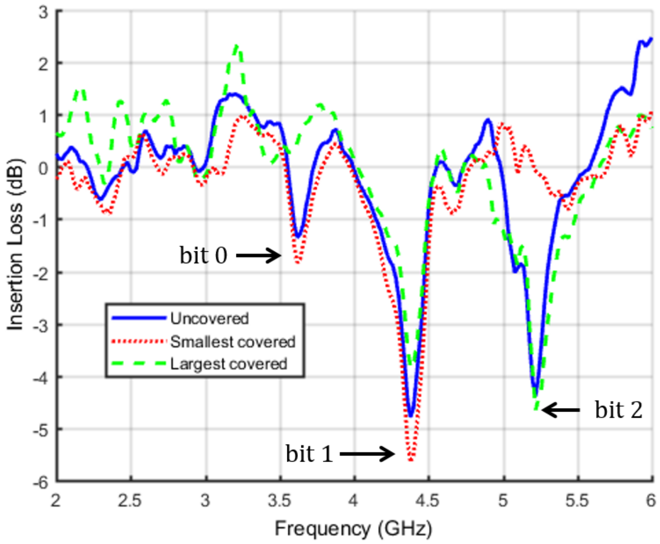

Figure 6–4: Insertion loss response of the tag at 5 cm in distance to the Tx and Rx antennas in the ambient environment, with and without resonators covered.

UWB antennas on the tag. However, it has been shown that [3] the phase of the tag still preserve the information in a greater distance that is more insensitive to the noises. This could be done in the future work.

6.2 Wired Measurements

Before conducting the wireless liquid concentration measurements, it is beneficial to do the wired measurement first using the CPW multiresonator circuit designed in Chapter 4. This is because the wired measurement does not suffer from the ambient noise, thus demonstrating a clearer correlation between the concentration and sensor's frequency response. The extracted relationship can be referred to as the reference to cross-check the wireless response from the sensor. The experiment is conducted in room temperature.

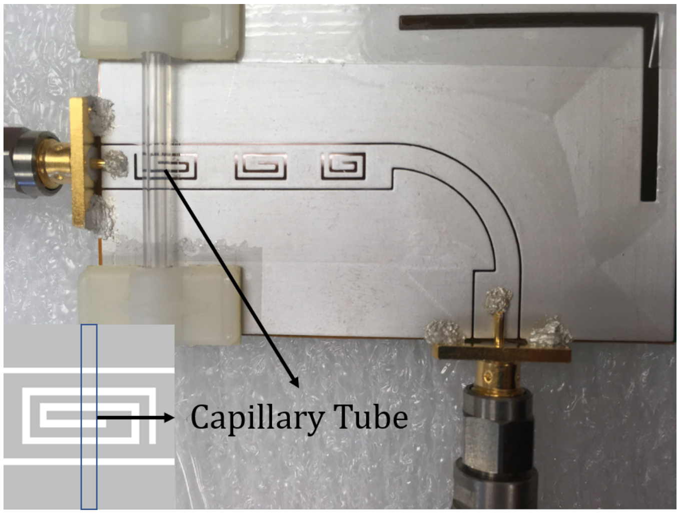

Figure 6–5: Wired liquid concentration measurement set up.

Fig. 6–5 shows the experiment set up for the wired concentration measurements. The silver epoxy is used to cold solder the SMA connectors to the circuit. The whole circuit is with a 70 × 40 mm^2 dimension, where a capillary tube with an inner diameter 0.75 mm is centered on the top of the resonator "res 3" to achieve a better sensitivity [22]. In this measurement, two different binary liquid mixtures are tested, water/sodium chloride (NaCl) and water/sucrose. The capillary tube is drained and filled the tube with a syringe. The water/NaCl concentration is varied in the range [0, 100] μg/ml with an increment of 10 μg/ml per sample, and the water/sucrose concentration is varied in the range [0, 500] μg/ml with an increment of 50 μg/ml per sample.

Primarily, the appearance of the liquid solutions alter the capacitance C_3' of the resonator "res 3" in Fig. 4–8. As discussed in [23], C_3' can be approximated as

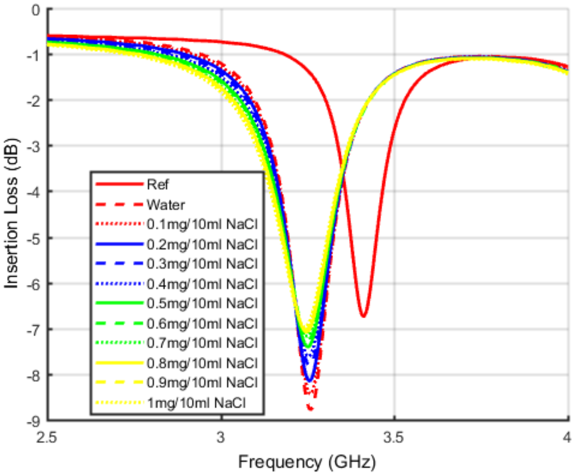

Figure 6–6: Wired measured insertion loss response of the resonator ”res 3” versus various water/NaCl solutions with different concentrations in room temperature.

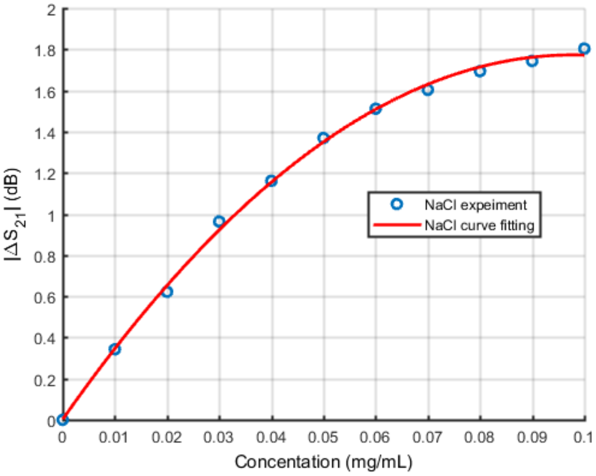

Figure 6–7: Wired measured $|\Delta S_{21}|$ variation with NaCl concentrations in the range [0, 100] μg/ml with an increment of 10 μg/ml per sample.

$$C_3' = C_0 + \epsilon_{solutions} C_{tube} \tag{6.1}$$

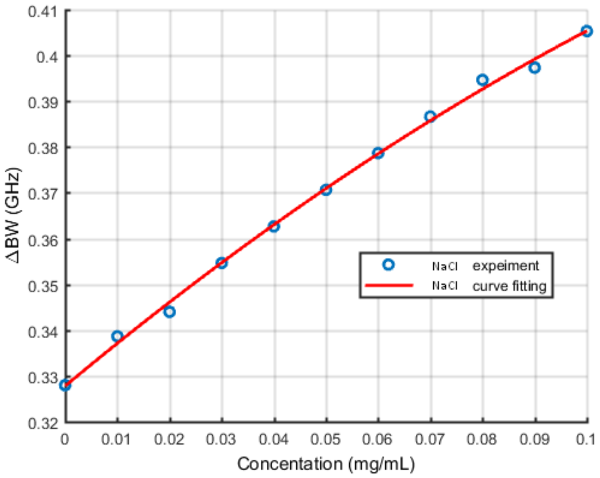

Figure 6–8: Wired measured ΔBW variation with NaCl concentrations in the range [0, 100] μg/ml with an increment of 10 μg/ml per sample.

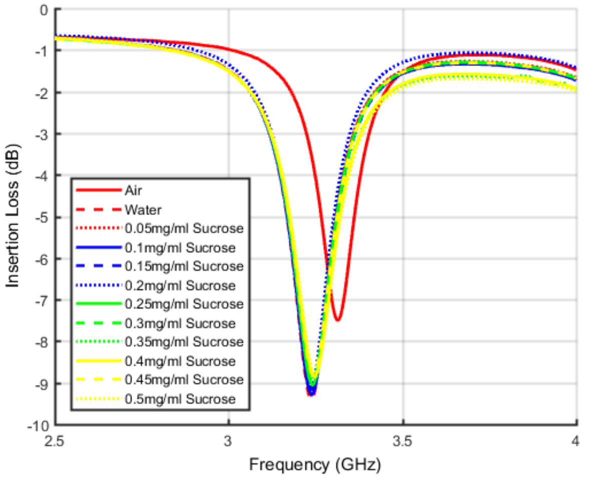

Figure 6–9: Wired measured insertion loss response of the resonator ”res 3” versus various water/sucrose solutions with different concentrations in room temperature.

where C_0 is the capacitance of the ”res 3” excluding the capillary channel, and C_{tube} is the capacitance contributed by the solution-filled capillary channel. The complex dielectric constant of the liquid solution is

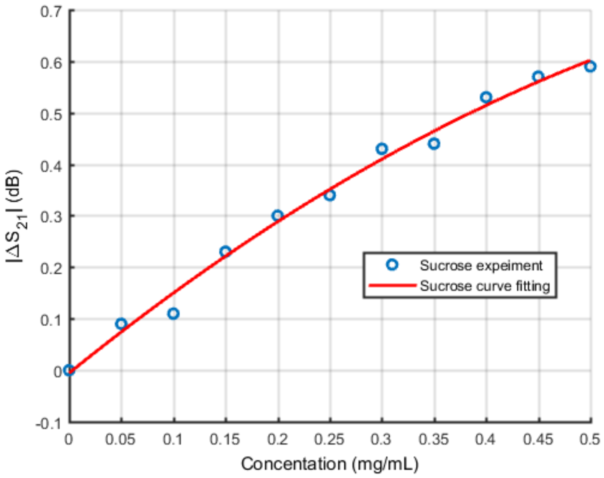

Figure 6–10: Wired measured $|\Delta S_{21}|$ variation with sucrose concentrations in the range [0, 100] μg/ml with an increment of 10 μg/ml per sample.

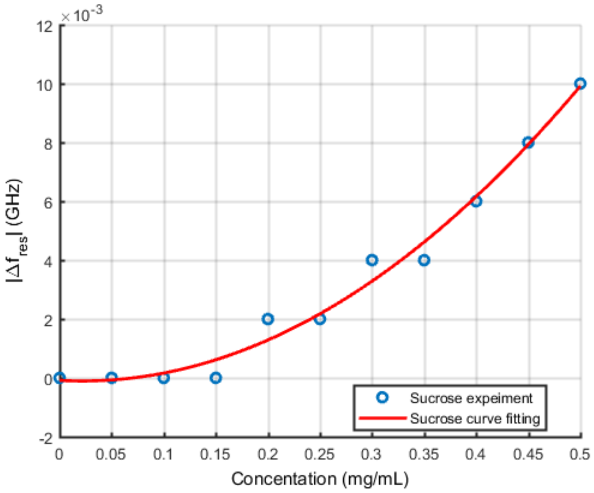

Figure 6–11: Wired measured $|\Delta f_{res}|$ variation with sucrose concentrations in the range [0, 500] μg/ml with an increment of 50 μg/ml per sample.

$$\epsilon_{solutions} = \epsilon^{'}_{solutions} + j\epsilon^{''}_{solutions} \tag{6.2}$$

From Eq. 4.31 - Eq. 4.33 and Eq. 7.1 - 7.2, it can be seen that the Q-factor as well as the resonant frequency are related to the dielectric property of the liquid samples. It is shown in the same literature that $\epsilon'_{solutions}$ and $\epsilon''_{solutions}$ have different contributions on the change of the Q-factor and the resonant frequency, respectively. Also, for different solutions, the increase of the concentration will cause different degree of change of $\epsilon'_{solutions}$ and $\epsilon''_{solutions}$. Therefore, it is convenient to use the parameter that varies noticeably as the concentration of the solution changes. As presented in [21], the water/NaCl solutions produce a dominant change on the Q-factor, and the water/sucrose solutions generate a change on both Q-factor and resonant frequency. This is because the complex permittivity of different liquids has a different impact on these two parameters [23]. To extract the correlation between the concentration variation and the corresponding insertion loss response of two different binary mixtures, the amplitude change of the insertion loss at the resonant frequency $|\Delta S_{21}|$ and the half-power 3-dB bandwidth ΔBW are analyzed for the water/NaCl samples. For the water/sucrose solutions, in addition to $|\Delta S_{21}|$, the resonant frequency shift $|\Delta f_{res}|$ will be analyzed. The definitions of $|\Delta S_{21}|$ and $|\Delta f_{res}|$ are defined mathematically as

$$\begin{cases} |\Delta S_{21}| = |S_{21,liquid} - S_{21,water}| \\ |\Delta f_{res}| = |f_{liquid} - f_{water}| \end{cases} \tag{6.3}$$

where $S_{21,liquid}$ and f_{liquid} represent the insertion loss at the resonant frequency and resonant frequency of different concentration liquid samples, respectively. $S_{21,water}$

and f_{water} are the insertion loss at the resonant frequency and resonant frequency of pure water.

Fig. 6–6 shows the insertion loss response of "res 3" with different NaCl concentrations, where a noticeable Q-factor degeneration is caused by the increase of the concentration, and thus a higher conductivity loss. The change of the insertion loss at the resonant frequency $|\Delta S_{21}|$ is plotted in Fig. 6–7, together with a second-order curve fitting. $|\Delta S_{21}|$ monotonically increases within the testing concentration range, showing a good linear correlation before 60 μg/ml, after which the sensitivity starts to degrade. The 3-dB bandwidth change ΔBW is another metric to reflect the change of liquid concentrations. Fig. 6–8 presents the change of ΔBW that monotonically increases with the concentrations. It demonstrates a better linearity than the $|\Delta S_{21}|$ plot across the whole concentration range, with very small bandwidth change for each concentration increment. Across the testing concentration range, the second-order regression result for $|\Delta S_{21}|$ in Fig. 6–7 is

$$y = -185.2253x^2 + 36.222x + 0.0023 \tag{6.4}$$

and for ΔBW in Fig. 6–8 is

$$y = -1.7405x^2 + 0.9498x + 0.3278 \tag{6.5}$$

Fig. 6–9 shows the insertion loss response of "res 3" with different sucrose concentrations, where a non-obvious Q-factor degeneration is observed due to the increase of the concentration. The change of $|\Delta S_{21}|$ is plotted in Fig. 6–10, together with a second-order curve fitting. It is observed that the sensor has a lower sensitivity to the sucrose concentrations in terms of the Q-factor variation. Nevertheless, $|\Delta S_{21}|$ in Fig. 6–10 shows a more linear fitting result than the NaCl $|\Delta S_{21}|$ plot in Fig. 6–7. The resonant frequency shift $|\Delta f_{res}|$ is plotted in Fig. 6–11 which monotonically increases within the testing concentration range, showing an exponential correlation with respect to the concentration increment. When the sucrose concentration is low, particularly under 0.2 mg/ml, $|\Delta f_{res}|$ almost remains unchanged with the supported VNA resolution division. The same phenomena observed from 0.2 mg/ml to 0.35 mg/ml where the concentration increment does not lead to a noticeable $|\Delta f_{res}|$ variation. In other research works [23], [22], the microwave resonator demonstrates a 10 to 100 times worse sensitivity to sucrose solutions than NaCl, which confirms the observations found here. This could be because the sucrose solutions introduce less conduction loss than the NaCl. The second-order regression result for $|\Delta S_{21}|$ in Fig. 6–10 is

$$y = -0.8485x^2 + 1.6388x - 0.0055 \tag{6.6}$$

and for Δf_{res} in Fig. 6–11 is

$$y = 0.0438x^2 - 0.0019x - 0.0001 \tag{6.7}$$

The performance of the sensor on these two solutions are summarized in Table 6–2. It can be seen that the sensor does have a better sensitivity on the concentration variation of NaCl than sucrose. It is noted that the sensor's sensitivity is approximately calculated from the linear region of each plot. From the results, it

Table 6–2: Wired concentration measurements on NaCl and sucrose solutions

Solutions	Concentration	Increment	Sensitivity
water/NaCl	[0, 100] μg/ml	10 μg/ml	in [0, 60] μg/ml: $\lvert\Delta S_{21}\rvert$: 0.03 dB/($\mu$g/ml) in [0, 100] μg/ml: $\lvert\Delta BW\rvert$: 1 MHz/(μg/ml)
water/sucrose	[0, 500] μg/ml	50 μg/ml	in [0, 500] μg/ml: $\lvert\Delta S_{21}\rvert$: 0.002dB/($\mu$g/ml) in [150, 500] μg/ml: $\lvert\Delta f_{res}\rvert$: 20KHz/($\mu$g/ml)

seems the sensor demonstrates a very high sensitivity on both solutions when the concentrations are low.

6.3 Wireless Measurements

For the proof-of-concept, two different liquid mixtures are prepared for the wireless concentration measurement, the water/NaCl and water/isopropanol solutions. The water/sucrose mixtures do not give usable results, which will be discussed shortly. The NaCl concentration is varied in the range [0, 100] μg/ml with an increment of 10 μg/ml per sample. The isopropanol concentration is varied in the range of [0, 99] vol% in terms of volume fraction, with an increment of 20 vol% per sample. Fig. 6–12 shows the experiment setup. Similar to Fig. 6–3, two cross-polarized Vivaldi antennas interrogate the RFID tag that is place 5 cm away in the ambient environment, where a capillary tube with an inner radius $r_c = 0.75$ mm is centered on the top of the resonator ”res 2” to achieve a better sensitivity. ”res 2” is selected for the wireless measurement, because it shows a higher Q-factor than ”res 1” and ”res 3” in Fig. 6–4. The tube is filled and drained with different liquid samples by a

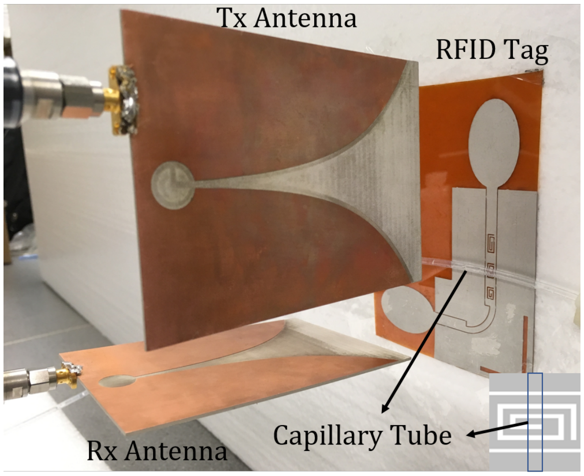

Figure 6–12: Wireless measurement setup for the solutions with various concentrations. The capillary tube is place on the top the resonator ”res 2”.

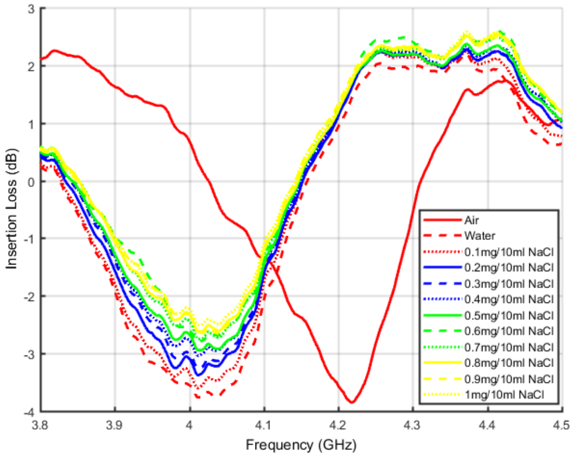

Figure 6–13: Wireless measured insertion loss response of the resonator ”res 2” versus various water/NaCl solutions with different concentrations in room temperature.

syringe to avoid air bubbles, and the data are collected by the VNA. The experiments are operated in room temperature.

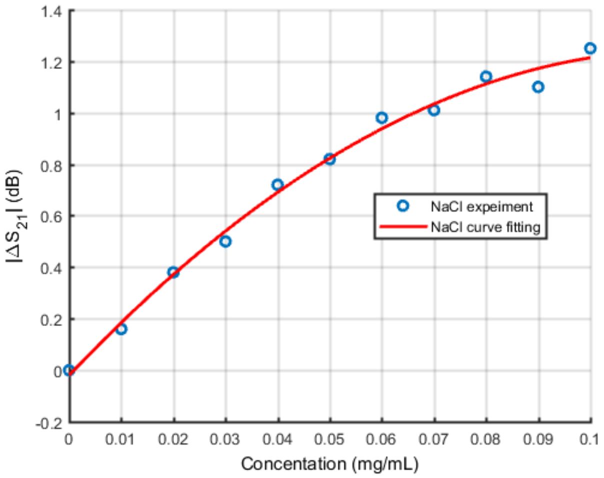

Figure 6–14: Wireless measured $|\Delta S_{21}|$ variation with NaCl concentrations in the range [0, 100] μg/ml with an increment of 10 μg/ml per sample.

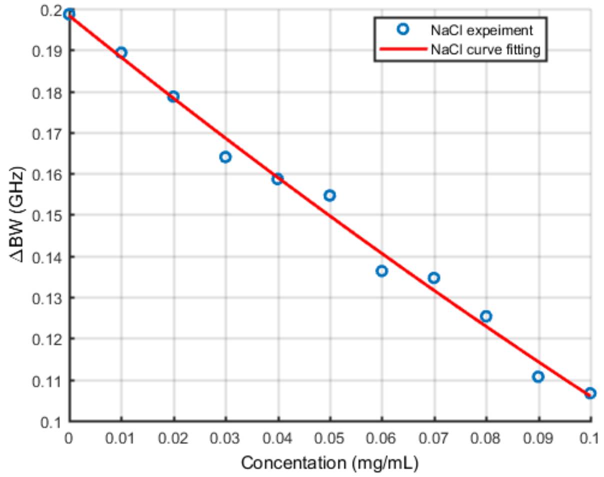

Figure 6–15: Wireless measured ΔBW variation with NaCl concentrations in the range [0, 100] μg/ml with an increment of 10 μg/ml per sample.

Fig. 6–13 shows the insertion loss response of the resonator ”res 2” with the water/NaCl samples. Similar to Fig. 6–6, it is noticed that the concentration variation mainly contributes to the change of the Q-factor. $|\Delta S_{21}|$ and ΔBW versus different NaCl concentrations from the frequency response are plotted in Fig. 6–14 and 6–15, respectively, together with the second-order polynomial fitting result. In Fig. 6–14, the sensor demonstrates a better sensitivity and linearity when the NaCl concentrations are low. The linearity degrades when the concentration is above 60 μg/ml. Within [0, 60] μg/ml, $|\Delta S_{21}|$ response is with an average sensitivity of 0.03 dB/(μg/ml). It is interesting to note that ΔBW in Fig. 6–15 shows a very good linearity across the whole concentration range, with an average sensitivity of 1 MHz/(μg/ml). The shift of resonant frequency is not noticeable in the wireless measurement. As explained before, the water/NaCl mixture has a more dominant influence on the Q-factor rather than the resonant frequency. To magnify the sensitivity for the shift of resonant frequency, it is advisable to increase the inner diameter of the capillary. The trade-off, however, would be a higher possibility of introducing air bubbles in the tube that would destroy the homogeneity of the liquid mixtures [21]. Across the whole testing concentration range, the second-order regression result for $|\Delta S_{21}|$ in Fig. 6–14 is

$$y = -90.5594x^2 + 21.3923x - 0.0199 \tag{6.8}$$

and for ΔBW in Fig. 6–15 is

$$y = 0.9596x^2 - 1.0193x + 0.1983 \tag{6.9}$$

As anticipated, plots in Fig. 6–7 and 6–14 have a very similar trend, whereas Fig. 6–8 and 6–14 imply two totally different correlations. The factor causes this huge deviation might be the resonant frequency. Not obvious, but in Fig. 6–6 there is still a very small resonant frequency shift with the concentration increment. This is shown in Fig. 6–16. The complex permittivity has a very small effect on $|\Delta f_{res}|$ [21] that is still detected by the microwave resonator in the wired experiment. An approximated 5 MHz frequency shift is caused by each NaCl concentration increment. As opposite, in Fig. 6–13 the resonant frequency nearly remains unchanged across the testing concentration range. Shown in Fig. 6–17, $|\Delta f_{res}|$ only fluctuates around a rough average frequency of 138 MHz. The perturbation of $|\Delta f_{res}|$ is primarily caused by the ambient noises. As a result, in Fig. 6–13 the S_{21} amplitudes at the half-power point on the right-hand side of the resonant frequency gradually shift toward the lower frequencies, whereas the S_{21} amplitudes on the left-hand side of the resonant frequency are almost unvaried. Therefore, it leads to an increase of the Q-factor. The shift of resonant frequency has been found to be strongly dependent on the diameter of the capillary tube. Particularly, the sensitivity of the $|\Delta f_{res}|$ will improve with the increase of the tube size [21]. In future work, it will be beneficial to repeat the same experiment with different capillaries.

Fig. 6–18 shows the insertion loss response of water/isopropanol samples measured by the same resonator. Noted that both Q-factor and resonant frequency change noticeably for this mixture. $|\Delta S_{21}|$ and $|\Delta f_{res}|$ response versus different isopropanol concentrations are shown in Fig. 6–19 and 6–20, respectively, together with the second-order polynomial fitting result. When the isopropanol concentration is low, neither $|\Delta S_{21}|$ nor $|\Delta f_{res}|$ changes obviously. When the concentration of isopropanol is above 20 vol%, both $|\Delta S_{21}|$ and $|\Delta f_{res}|$ increase monotonically with the increase of the concentration. In Fig. 6–19, $|\Delta S_{21}|$ plot shows a good linearity within

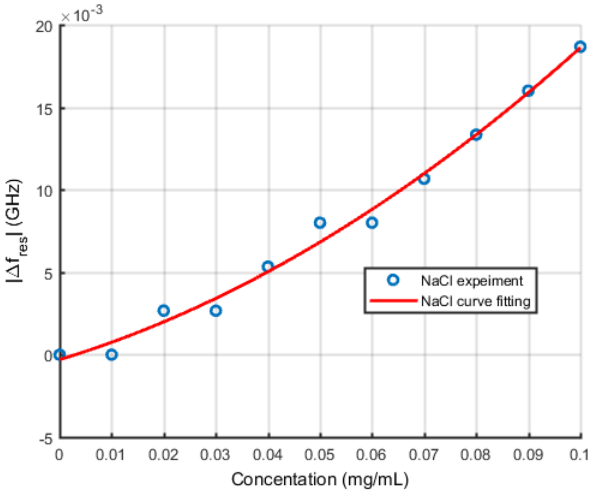

Figure 6–16: Wired measured $|\Delta f_{res}|$ variation with NaCl concentrations in the range [0, 100] μg/ml with an increment of 10 μg/ml per sample.

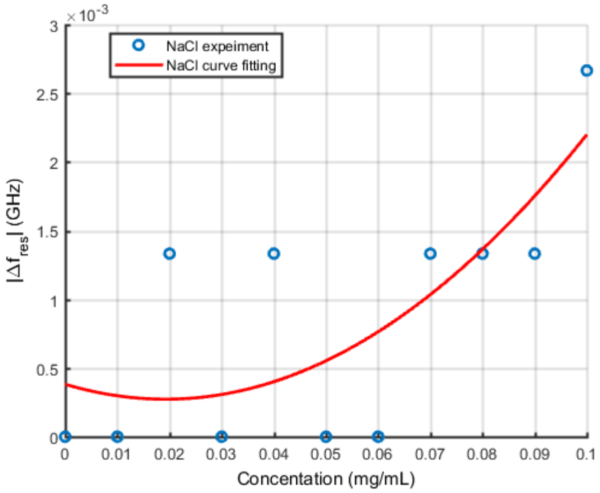

Figure 6–17: Wireless measured $|\Delta f_{res}|$ variation with NaCl concentrations in the range [0, 100] μg/ml with an increment of 10 μg/ml per sample.

[20, 80] vol% concentration range with a sensitivity of 0.3 dB/(vol 20%). $|\Delta f_{res}|$ plot in Fig. 6–20 shows a good linearity within [40, 99] vol% concentration range with

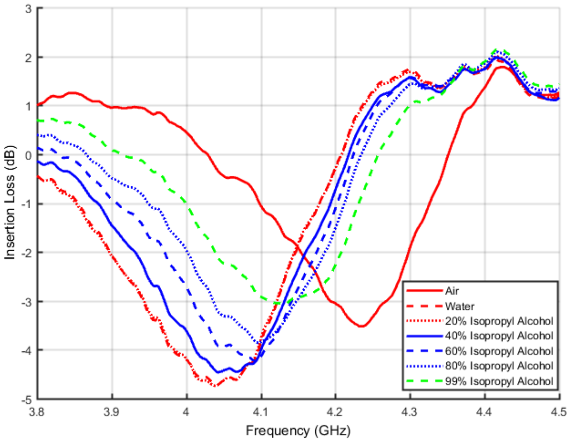

Figure 6–18: Insertion loss response of the resonator "res 2" versus various water/isopropanol solutions with different concentrations in the room temperature.

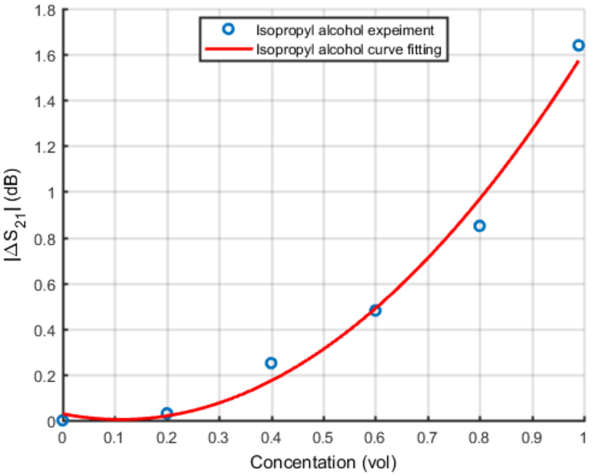

Figure 6–19: Measured $|\Delta S_{21}|$ variation with isopropanol concentrations in the range [0, 99] vol% with an increment of 20 vol% per sample.

an average sensitivity of 30 MHz/(20 vol%). Across the whole testing concentration range, the second-order regression result for $|\Delta S_{21}|$ in Fig. 6–19 is

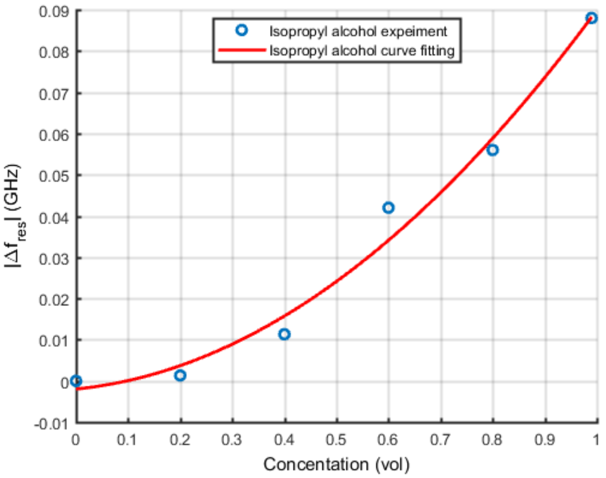

Figure 6–20: Measured $|\Delta f_{res}|$ variation with NaCl concentrations in the range [0, 99] vol% with an increment of 20 vol% per sample.

$$y = 2.0334x^2 - 0.453x + 0.0286 \tag{6.10}$$

and for ΔBW in Fig. 6–20 is

$$y = 0.0794x^2 + 0.0124x - 0.002 \tag{6.11}$$

Regarding the water/sucrose wireless measurements, no usable data has been collected from the sensor within the testing concentration range ([0, 500] μg/ml) due to sensor's poor sensitivity to sucrose in the wireless environment. $|\Delta S_{21}|$ changes less than 0.1 dB in the wired measurement with a 50 μg/ml concentration increment at the low concentration range, implying a more than 15 times worse sensitivity compared to the NaCl measurements. This tiny $|\Delta S_{21}|$ variation can be easily distorted

Table 6–3: performance summary of the sensor at 5 cm in room temperature

Solution	Concentration Range	Measured Parameters	Applicable Range	Sensitivity
water/NaCl	[0, 100] μg/ml	$\lvert\Delta S_{21}\rvert$	$[0, 60]$ μg/ml	0.03 dB/(μg/ml)
		ΔBW	$[0, 100]$ μg/ml	1 MHz/(μg/ml)
water/isopropanol	[0, 99] vol%	$\lvert\Delta S_{21}\rvert$	$[20, 80]$ vol%	0.3 dB/(20 vol%)
		$\lvert\Delta f_{res}\rvert$	$[40, 99]$ vol%	30 MHz/(20 vol%)

by the ambient noises, destroying the frequency response. Either $|\Delta S_{21}|$ or $|\Delta f_{res}|$ do not show any promising correlations compared to the wired experiments.

Table 6–3 summarizes the performance of the sensor in concentration measurements of liquid solutions. It can be seen that for one kind of liquid solution, different ways of data extraction could lead to different linearity and sensitivity. It should be remarked that in contrast to the designs in [21, 22, 23, 24, 25, 26, 27, 4, 28], the proposed sensor operates wirelessly in the ambient environment, and it is strongly subjected to ambient noises. Therefore, the sensitivity of the sensor is drastically degenerated, showing a limited linear range for the concentration measurements. The inevitable air bubbles in the capillary tube also cause the error due to the inhomogeneity of the liquid, which can be mitigated by using a smaller diameter capillary tube. Nevertheless, it will degrade the evaluation of ΔBW [21]. The lossy conductive ink used for the sensor is another factor for decaying its accuracy. With all these issues addressed, it is still interesting to see that within the linear response region, the sensor has a good sensitivity over a low concentration range of NaCl solutions, in contrast to [21, 22, 27]. Furthermore, to demonstrate its applicability for measuring other liquids, the sensor is used for measuring the isopropanol solutions with different concentrations, generating usable results with a coarse concentration increment. It is reasonable to believe that our sensor will achieve a better sensitivity when it is operated in the wired mode.

CHAPTER 7
Acetic Acid Vapor Sensing

7.1 Raoult's Law

Motivated by [5], the proposed multiresonator circuit in Chapter 4 can also be used for the detection of volatile organic compounds (VOCs) with the aid of polydimethylsiloxane (PDMS). It has been shown that by coating a thin PDMS layer on the top of a microwave resonator, the capacitance of the PDMS will change with the appearance of VOCs, therefore alternating the Q-factor and the resonant frequency of the resonator. The swelling effect of PDMS will absorb VOCs that cause the thickness and dielectric constant of the PDMS layer changed. Roughly speaking, the increase of the concentration of VOCs will lead to an increase of the PDMS thickness, as well as the increase of effective permittivity [5].

For the proof-of-concept, a thin 1 mg layer of PDMS is coated on the resonator "res 3", and the whole multiresonator circuit is put inside a small chamber whose volume is 170 ml. The targeted VOC for the test is the acetic acid (CH_3COOH), a common VOC found in vinegar. Fig. 7–1 shows the experiment setup. The vinegar with different acetic acid concentration will be deposited within the chamber once at a time. When the test starts, the chamber will be sealed by a lid and the concentration measurement begins.

Raoult's law is applied here for calculating the concentration of the acetic acid within the chamber. It establishes the correlation between the molar fraction of

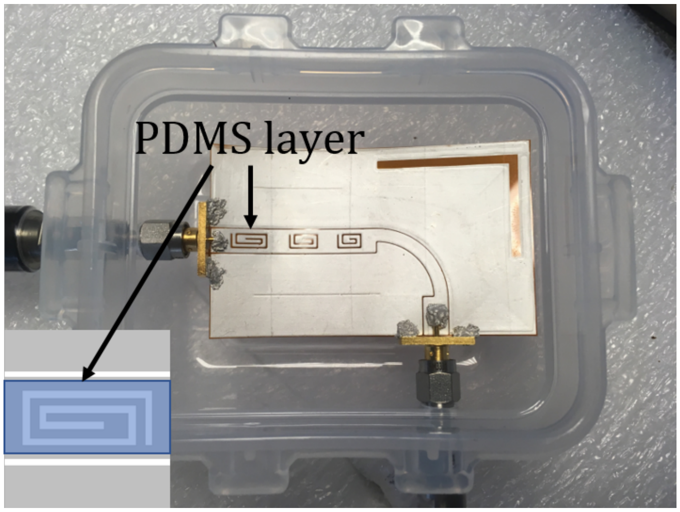

Figure 7–1: Gas chamber for acetic acid concentration measurement. A thin PDMS layer is coated on the resonator "res3". All tests are conducted in room temperature.

the liquid solution and the molar fraction of vapor in a sealed environment. In the following context, T is in Celsius, and pressure P is in Torr. First, the molar fraction of acetic acid and water of the solution is

$$\%mol_{solution,acid} = \frac{n_{CH_3COOH}}{n_{CH_3COOH} + n_{H_2O}} \tag{7.1}$$

$$\%mol_{solution,water} = \frac{n_{H_2O}}{n_{CH_3COOH} + n_{H_2O}} \tag{7.2}$$

Where n_{CH_3COOH} is the molar number of acetic acid, and n_{water} is the molar number of water. Second, the acetic acid vapor pressure is calculated by [65]

$$P_{acid} = 10^{7.80307-1651.2/(225+T)} \tag{7.3}$$

And the water vapor pressure:

$$P_{water} = e^{20.386-5132/(T+273.15)} \tag{7.4}$$

It is also required to calculate the air pressure in a sealed container so that the total vapor pressure of the environment can be obtained. This can be done by using the ideal gas law. Primarily, the air consists of 78.9% nitrogen (N_2) and 20.95% oxygen (O_2), which contribute most of the air pressure inside the sealed chamber. The air pressure is calculated by

$$P_{air} = \frac{0.00750062 n_{air} R(T + 273.15)}{V_{cont}} \tag{7.5}$$

where V_{cont} is the container size, and

$$n_{air} = n_{N_2} + n_{O_2} \tag{7.6}$$

where n_{air} is the summation of the molar number of nitrogen n_{N_2} and oxygen n_{O_2}. The total vapor pressure is therefore

$$P_{tot} = P_{acid} mol_{solution,frac,acid} + P_{water} mol_{solution,frac,water} + P_{air} \tag{7.7}$$

From Eq. 8.1 - 8.4 and 8.7, the molar fraction of acetic acid and water of the vapor can be found by

$$\%mol_{vapor,acid} = \frac{\%mol_{solution,acid} P_{acid}}{P_{tot}} \tag{7.8}$$

$$\%mol_{vapor,water} = \frac{\%mol_{solution,acid} P_{water}}{P_{tot}} \tag{7.9}$$

Table 7–1: Correspondences between different concentrations of acetic acid solutions and acetic acid vapor concentration in the chamber

liquid acetic acid concentration (vol)	5%	4%	3%	2%	1%
acetic acid vapor concentration (ppm)	120	95	70	45	20

The purchased vinegar has an acetic acid volume fraction of 5 vol%. By dilution, a set of solutions with different acetic acid volume fraction varies from 1 to 5 vol% is obtained. The increment is 1 vol% per sample. Table 7–1 shows the acetic acid vapor concentration in the chamber from different concentrations of acetic acid solutions by using Raoult's law.

7.2 Concentration Test

7.2.1 Fast Cycling between Acetic Acid and Air

There are two experiments carried out in this section. The first experiment is to see how the sensor responses to fast cycling of air and different concentration acetic acid vapors. Each cycle lasts for 300 seconds. The sensor will be exposed to one acetic acid dilution deposited within the gas chamber for 200 seconds with the lid closed. The next 100 second the lid will be opened, and the sensor will be in contact with the ambient environment. After one cycle is completed, a syringe is used to empty the liquid within the chamber, and a new concentration acetic acid solution will be deposited in the chamber. Since in total there are five different acetic acid dilutions, five cycles will be conducted. Two parameters will be used to evaluate the sensor's behavior to different concentration acetic acid vapors, the insertion loss at the resonance S_{21} and the resonant frequency f_{res}. The data of both are recorded every 10 seconds.

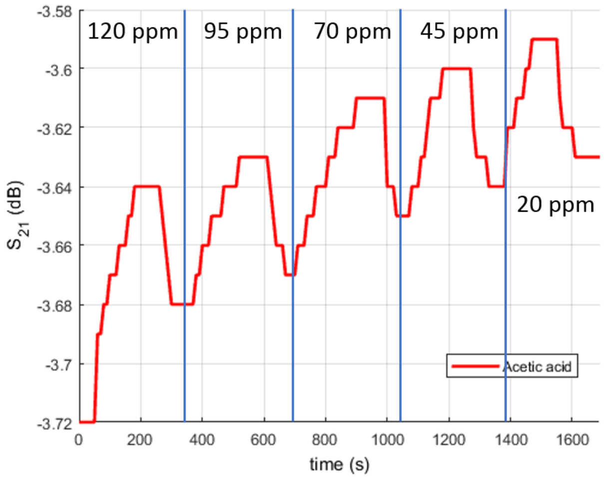

Figure 7–2: S_{21} response over the cycling between ambient air and different concentration acetic acid vapors.

Figure 7–2 shows the S_{21} response to the cycling between ambient air and different concentration acetic acid vapors. Initially, S_{21} of ”res 3” is around -3.72 dB. The first liquid acetic acid solution is with 5 vol%, corresponding to a 120 ppm vapor concentration. After the deposition of the acetic acid solution, the container is sealed and the test begins. It can be seen that S_{21} drastically increases in the first 150 seconds until hitting the time at the 200-second. It stops increases for about 50 seconds, remaining at -3.64 dB. The lid is then opened and S_{21} rapidly drops back to -3.68 dB in 100 seconds. The same operations repeated with 95 ppm, 70 ppm, 45 ppm, and 20 ppm acetic acid vapor and similar observations have been found. In addition, S_{21} drifts from the original -3.72 dB to around -3.63 dB after all five cycles are finished, with an average 0.02 dB increment from each cycle. This is because the diffusion process of acetic acid molecules is governed by the exponential correlation, explained by the well-known Fick’s second law. It should be expected that both the

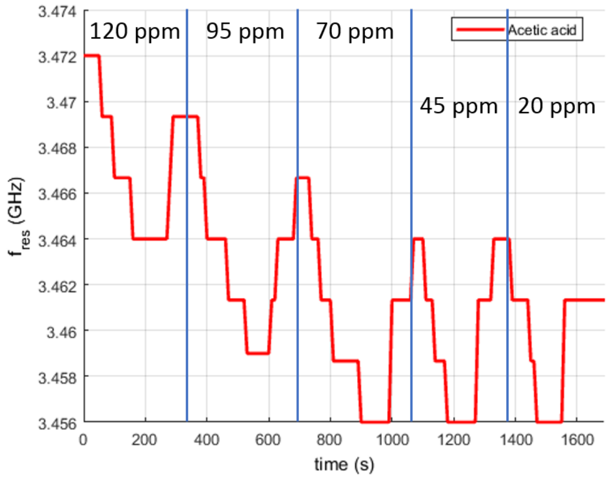

Figure 7–3: f_{res} response over the cycling between ambient air and different concentration acetic acid vapors.

increase and decrease of S_{21} should be in an exponential fashion, meaning that the gradient of S_{21} decreases with the time. In this experiment, since the time given for the air exposure is very short, the sensor does not fully recover from the acetic acid vapor environment as some acetic acid molecules still reside within the PDMS layer. In this case, it seems the exposures of different concentration acetic acid vapor contribute to a similar magnitude change of S_{21}. Again, since the acetic acid molecules from the last cycle do not diffuse to the ambient totally, the acetic acid molecules of the new cycle accumulate with the previous ones, which does not truly reflect the real S_{21} change caused by each acetic acid vapor concentration.

Similar phenomena are found in Fig. 7–3 for the resonant frequency of ”res 3” f_{res}. It starts at 3.472 GHz and promptly decreases with the appearance of acetic acid. f_{res} stops changing for a while after 200-second. Exposing to the air then shifts f_{res} back to about 3.468 GHz rapidly within 100 seconds, followed by the next cycle.

By comparing Fig. 7–2 and Fig. 7–3, it can be seen that two parameters, S_{21} and f_{res}, response to the appearance of acetic acid vapor spontaneously but oppositely. Instead, f_{res} gradually drifts toward lower frequency. The reason has been explained by the Maxwell Garnett equation [66] and simulations in [5]: the inclusion of higher concentration VOCs will increase the effective permittivity, thereby decrease the resonant frequency. Alike S_{21}, since the diffusion process is an exponential relation with respect to time, the rising and falling of f_{res} should be also exponential pattern. With both Fig. 7–2 and Fig. 7–3, this experiment, therefore, suggests that to truly analyze the drift of S_{21} and f_{res}, enough time should be given to the sensor to be exposed to the air so that it can come back to its steady state.

7.2.2 Slow Cycling between Acetic Acid and Air

Discussed in [5], the drift of S_{21} and f_{res} is due to the absorption of acetic acid molecules by the PDMS layer. Therefore, if enough time is given for the sensor to react to the acetic acid vapors, it should render different responses with different concentrations assuming the sensor has robust enough sensitivity. The second experiment is approached in this method: five sub-tests are conducted in this experiment, and in each test one concentration of the acetic acid solution is deposited within the chamber, and the observation time changes from 300 seconds to 1800 seconds. After the one test is completed, the lid is opened and the liquid is withdrawn from the chamber. The sensor is exposed to the ambient air for one night to ensures it recovers to its steady state. The next test is carried out afterward.

It is noted that, due to the inevitable drifting of S_{21} and f_{res}, the collected data from these five tests will have a different starting point. To normalize all plots, the

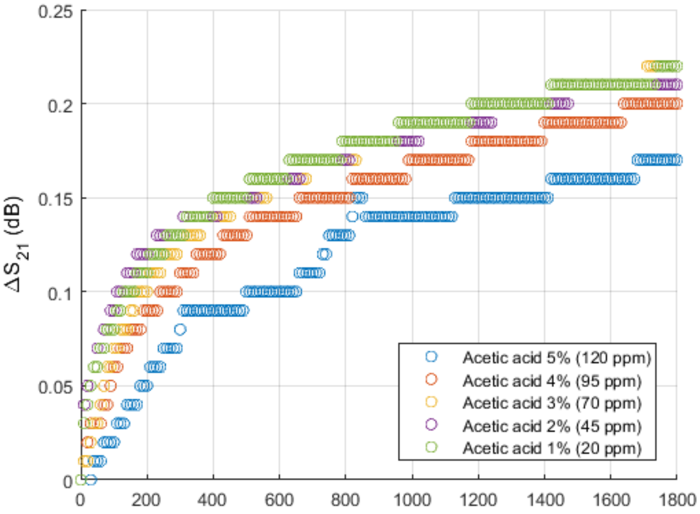

Figure 7–4: ΔS_{21} of "res 3" with all five different acetic acid vapor concentrations.

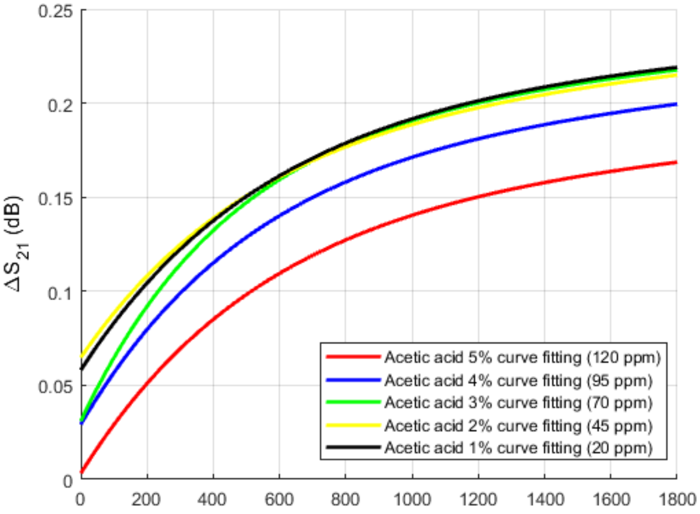

Figure 7–5: ΔS_{21} curve fitting results of "res 3" with all five different acetic acid vapor concentrations.

starting point of each test (both S_{21} and f_{res}) will be subtracted from each original data set that simply gives a better presentation, meaning that all experimental data are shifted to start from the origin. Fig. 7–4 shows the normalized S_{21} plot, denoted as ΔS_{21} (not the same as Eq. 7.3). The exponential fittings are presented in Fig. 7–5 for each vapor concentration since it should follow Fick's second law. It can be seen that the gradient of ΔS_{21} decreases with time. For each test, after 200 seconds, ΔS_{21} may remain unchanged for more than 200 seconds before moving onto the next ΔS_{21} value, which explains the observation in Fig. 7–2. At 1800-second, the curve fittings suggest that the sensor is able to differentiate 120 and 95 ppm acetic acid vapor concentration. Whereas 70, 45, and 20 ppm are not distinguishable that are all about 0.2 dB. The curve fittings in Fig. 7–5 are

$$y_{120ppm} = 0.1556e^{6.436\times10^{-5}x} - 0.1524e^{-1.785\times10^{-3}x} \tag{7.10}$$

$$y_{95ppm} = 0.1826e^{6.331\times10^{-5}x} - 0.1534e^{-1.884\times10^{-3}x} \tag{7.11}$$

$$y_{95ppm} = 0.1952e^{6.854\times10^{-5}x} - 0.1643e^{-2.195\times10^{-3}x} \tag{7.12}$$

$$y_{70ppm} = 0.1975e^{5.924\times10^{-5}x} - 0.1327e^{-1.327\times10^{-3}x} \tag{7.13}$$

$$y_{45ppm} = 0.2082e^{4.407\times10^{-5}x} - 0.1501e^{-1.754\times10^{-3}x} \tag{7.14}$$

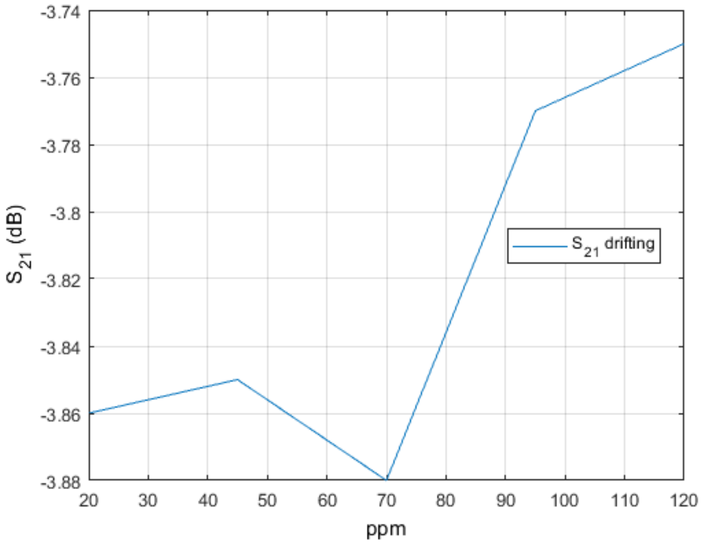

Figure 7–6: Drifting of S_{21} in five different tests.

The drifting of S_{21} is plotted in Fig. 7–6. It is seen that with enough exposure time, the starting point of S_{21} for each test does not drift hugely, with an exception at 70 ppm where an 0.13 dB drifting occurs. In total, a 0.11 dB drifting is observed from 120 ppm to 20 ppm.

Fig. 7–7 shows the normalized f_{res} plot, denoted as Δf_{res} (not the same as Eq. 7.3). The exponential fittings are plotted in Fig. 7–8 for each vapor concentration. The resonant frequency, as expected from Fig. 7–3, decreasing with the time as the inclusion of acetic acid molecules increases the effective permittivity, thus lowering down the resonant frequency. At the time point of 1800-second, the exponential fittings imply a clear differentiation between 120 ppm and 95 ppm, which are at -0.024 and -0.027 GHz, respectively. Similar to Fig. 7–7, the Δf_{res} plots for 70, 45,

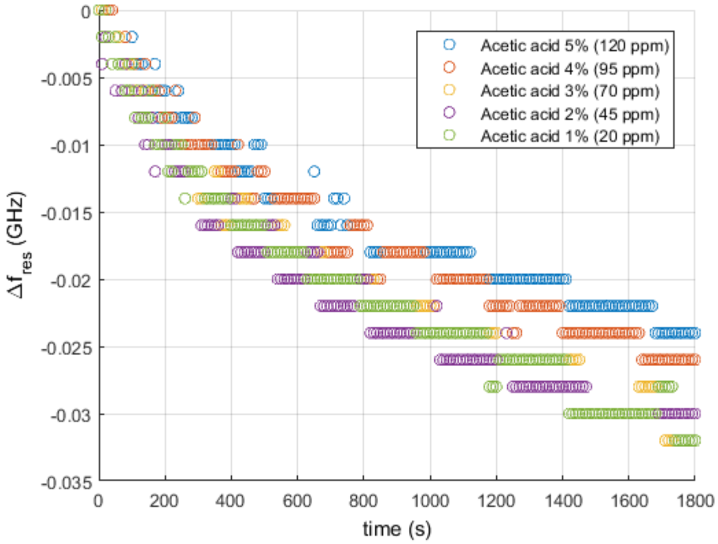

Figure 7–7: Δf_{res} of ”res 3” with all five different acetic acid vapor concentrations.

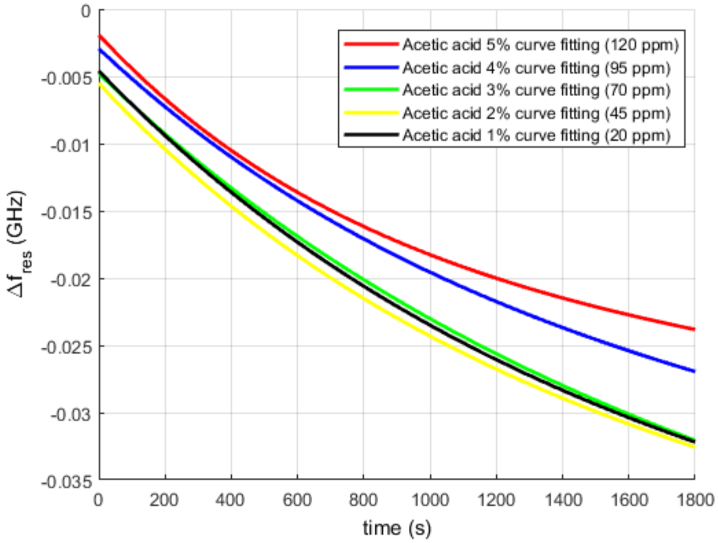

Figure 7–8: Δf_{res} curve fitting results of ”res 3” with all five different acetic acid vapor concentrations.

and 20 ppm are not distinguishable either, all are around -0.032 GHz at 1800-second. The exponential fittings in Fig. 7–8 are

$$f_{120ppm} = -0.02252e^{8.463\times10^{-5}x} + 0.0206e^{-1.194\times10^{-4}x} \tag{7.15}$$

$$f_{95ppm} = -0.02823e^{8.044\times10^{-5}x} + 0.02529e^{-8.301\times10^{-4}x} \tag{7.16}$$

$$f_{95ppm} = -0.03821e^{5.941\times10^{-5}x} + 0.03343e^{-6.458\times10^{-4}x} \tag{7.17}$$

$$f_{70ppm} = -0.03467e^{6.806\times10^{-5}x} + 0.02915e^{-8.234\times10^{-4}x} \tag{7.18}$$

$$f_{45ppm} = -0.03838e^{4.57\times10^{-5}x} + 0.03377e^{-7.058\times10^{-4}x} \tag{7.19}$$

The drifting of f_{res} is plotted in Fig. 7–9. Again, with enough exposure time, the starting point of f_{res} for each test does not drift hugely, with an exception at 70 ppm where an 0.1 GHz drifting occurs. In total, a 0.12 GHz drifting is observed from 120 ppm to 20 ppm.

In conclusion, the sensor does not drift a lot in this experiment if sufficient long recovery time is given for air exposure. It suggests that the sensor is reusable for multiple acetic acid vapor experiments. This process is expected to be faster if an air pump is used. The sensor does have adequate sensitivity for differentiating 120 and 95 ppm acetic acid vapor concentrations, for both ΔS_{21} and Δf_{res}. However, the concentration below 70 ppm becomes indistinguishable for the sensor. In [5], one

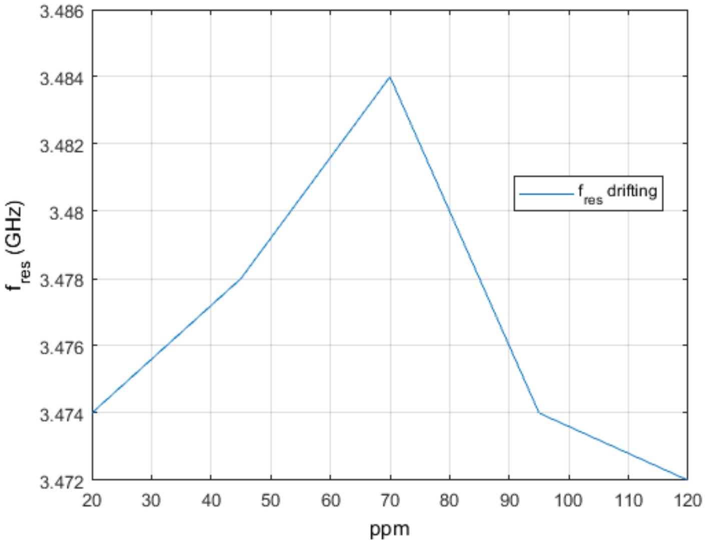

Figure 7–9: Drifting of f_{res} in five different tests.

way to increase the sensitivity is to increase the thickness of PDMS. The trade-off, however, will be longer response time.

CHAPTER 8
Conclusion

8.1 Summary of the Thesis

This thesis studies the design of a flexible printed chipless RFID tag. It is fabricated by the inkjet-printing technology on a flexible Kapton PI substrate. Two different design approaches are discussed, the microstrip line based and CPW based. After the comparison, the CPW structure shows better performance and compatibility to the inkjet printing technology. The tag contains three spiral resonators coupled to the CPW that encode a 3-bit signature in the frequency domain. Two cross-polarized UWB antennas connect to the CPW to receive and transmit the signals. To our knowledge, it is the first reported fully inkjet-printed flexible chipless RFID based on the insertion loss response. Two high-gain UWB cross-polarized Vivaldi antennas interrogate the RFID tag. Three resonances are achieved in the insertion loss response, implying a 3-bit message. The user has the freedom to modify the encoded information by shorting the resonators using copper tape or other highly conductive materials.

The RFID tag is applied for the wired and wireless concentration measurements of binary liquid mixtures by characterizing the insertion loss response. A capillary tube is placed on one of the resonators to allow the interaction between the sensor and the solutions. Water/NaCl and water/sucrose mixtures with different concentrations are measured by the sensor, wired and wirelessly. Different metrics are evaluated to analyze the sensitivity of the sensor to different liquids, ΔS_{21}, ΔBW, and Δf_{res}. The sensor shows good performance in the wired measurements for both NaCl and sucrose solutions. It presents a similar correlation between the concentration variation and frequency response reported in other literature [21, 22, 27], with a higher sensitivity in the low concentration region. The sensor shows some reasonable results in the wireless environment for NaCl, but poor sensitivity for the sucrose. Thus, the water/isopropanol mixtures with various concentrations are tested wirelessly to prove the sensor can wirelessly measure the concentration of other liquid compounds other than water/NaCl. Different concentrations of isopropanol not only change the Q-factor but also shift the resonant frequency, showing a good response with a concentration increment of 20 vol% per sample. Furthermore, the flexible printer multiresonator circuit proposed in Chapter 4 is used for the concentration measurement of acetic acid vapor. A thin PDMS layer is coated on the resonator "res3" to respond to the appearance of acetic acid by the swelling effect. Two parameters are evaluated, the insertion loss at the resonance S_{21} and the resonant frequency f_{res}. The sensor does differentiate different concentrations until 70 ppm, where the responses below this value become indistinguishable. However, due to the unavoidable drifting errors, the sensor requires quite a long time to recover to the steady state by exposing to the air. In nutshell, the sensor shows the potential for measuring both the concentrations of liquids and gases.

8.2 Future Work

There are many things need to be optimized to improve the sensor's performance, including but not limited to

- First, it will be beneficial to use a higher conductive ink to decrease the conduction loss of the tag.
- Second, by improving the impedance matching between reader's antennas and tag's antennas, the interrogation range could be improved.
- Third, instead of encoding the information as the S_{21} amplitude, the phase information is more resilient to the ambient noises, therefore the message will be more usable in a long distance.
- Forth, in the wireless liquid concentration measurements, $|\Delta f_{res}|$ will be more noticeable if the capillary tube is with a larger diameter. However, it has a higher risk of injecting the air bubbles through the tube and causing the inhomogeneity issue.
- Fifth, a better reader antenna fabrication process will improve the impedance matching at the micorstrip-to-slotline transition, thereby lowering down VSWR.
- Sixth, the reader unit is a VNA in this work, which is not feasible in the real-world application. It will be desirable to design a compact dedicated RFID reader system [67].
- Seventh, the sensor has the potential in other sensing applications such as monitoring the humidity and classifying more different gases wirelessly, which requires good collaboration with other facilities.

References

[1] N. C. Karmakar, E. M. Amin, and J. K. Saha. *Chipless RFID Sensors*. John Wiley Sons, Inc, 2016.

[2] F. Costa, S. Genovesi, and A. Monorchio. “A chipless RFID based on multiresonant high-impedance surfaces”. In: *IEEE Transactions on Microwave Theory and Techniques* 61.1 (Jan. 2013), pp. 146–153. ISSN: 0018-9480. DOI: `10.1109/TMTT.2012.2227777`.

[3] S. Preradovic et al. “Multiresonator-based chipless RFID system for low-cost item tracking”. In: *IEEE Transactions on Microwave Theory and Techniques* 57.5 (May 2009), pp. 1411–1419. ISSN: 0018-9480. DOI: `10.1109/TMTT.2009.2017323`.

[4] M. H. Zarifi et al. “Microwave ring resonator-based non-contact interface sensor for oil sands applications”. In: *Sensors and Actuators B: Chemical* 224 (2016), pp. 632–639. ISSN: 0925-4005. DOI: `https://doi.org/10.1016/j.snb.2015.10.061`. URL: `http://www.sciencedirect.com/science/article/pii/S092540051530527X`.

[5] M. H. Zarifi et al. “Detection of volatile organic compounds using microwave sensors”. In: *IEEE Sensors Journal* 15.1 (Jan. 2015), pp. 248–254. ISSN: 1530-437X. DOI: `10.1109/JSEN.2014.2345477`.

[6] C. S. Hartmann. “A global SAW ID tag with large data capacity”. In: *2002 IEEE Ultrasonics Symposium, 2002. Proceedings.* Vol. 1. Oct. 2002, 65–69 vol.1. DOI: `10.1109/ULTSYM.2002.1193354`.

[7] M. Borgese et al. “An inkjet printed chipless RFID sensor for wireless humidity monitoring”. In: *IEEE Sensors Journal* 17.15 (Aug. 2017), pp. 4699–4707. ISSN: 1530-437X. DOI: `10.1109/JSEN.2017.2712190`.

[8] Y. F. Weng et al. “Design of chipless UWB RFID system using a CPW multi-resonator”. In: *IEEE Antennas and Propagation Magazine* 55.1 (Feb. 2013), pp. 13–31. ISSN: 1045-9243. DOI: `10.1109/MAP.2013.6474480`.

[9] D. Betancourt et al. “Bending and folding effect study of flexible fully printed and late-stage codified octagonal chipless RFID tags”. In: *IEEE Transactions on Antennas and Propagation* 64.7 (July 2016), pp. 2815–2823. ISSN: 0018-926X. DOI: `10.1109/TAP.2016.2559522`.

[10] J. G. D. Hester and M. M. Tentzeris. “Inkjet-printed flexible mm-wave van-atta reflectarrays: a solution for ultralong-range dense multitag and multisensing chipless RFID Implementations for IoT Smart Skins”. In: *IEEE Transactions on Microwave Theory and Techniques* 64.12 (Dec. 2016), pp. 4763–4773. ISSN: 0018-9480. DOI: `10.1109/TMTT.2016.2623790`.

[11] R. Nair et al. “A fully printed passive chipless RFID tag for low-cost mass production”. In: *The 8th European Conference on Antennas and Propagation (EuCAP 2014).* Apr. 2014, pp. 2950–2954. DOI: `10.1109/EuCAP.2014.6902446`.

[12] A. Vena et al. “A fully inkjet-printed chipless RFID gas and temperature sensor on paper”. In: *2014 IEEE RFID Technology and Applications Conference (RFID-TA)*. Sept. 2014, pp. 115–120. DOI: `10.1109/RFID-TA.2014.6934211`.

[13] S. Preradovic and N. C. Karmakar. “Multiresonator based chipless RFID tag and dedicated RFID reader”. In: *2010 IEEE MTT-S International Microwave Symposium*. May 2010, pp. 1–1. DOI: `10.1109/MWSYM.2010.5515240`.

[14] M. E. Jalil et al. “Flexible printed chipless RFID tag using metamaterial–split ring resonator”. In: *Applied Physics A* 122.4 (Mar. 2016), p. 348. ISSN: 1432-0630. DOI: `10.1007/s00339-016-9865-5`. URL: `https://doi.org/10.1007/s00339-016-9865-5`.

[15] S. Khan, L. Lorenzelli, and R. S. Dahiya. “Technologies for printing sensors and electronics over large flexible substrates: a review”. In: *IEEE Sensors J.* 15.6 (June 2015), pp. 3164–3185. ISSN: 1530-437X. DOI: `10.1109/JSEN.2014.2375203`.

[16] S. Koskinen, L. Pykari, and M. Mantysalo. “Electrical performance characterization of an inkjet-printed flexible circuit in a mobile application”. In: *IEEE Transactions on Components, Packaging and Manufacturing Technology* 3.9 (Sept. 2013), pp. 1604–1610. ISSN: 2156-3950. DOI: `10.1109/TCPMT.2013.2261774`.

[17] Z. Yin et al. “Inkjet printing for flexible electronics: materials, processes and equipments”. In: *Chinese Science Bulletin* 55.30 (Oct. 2010), pp. 3383–3407. ISSN: 1861-9541. DOI: `10.1007/s11434-010-3251-y`. URL: `https://doi.org/10.1007/s11434-010-3251-y`.

[18] O. Lund Bo and E. Nyfors. “Application of microwave spectroscopy for the detection of water fraction and water salinity in water/oil/gas”. In: *Journal of Non-Crystalline Solids* 305 (July 2002), pp. 345–353. DOI: `10.1016/S0022-3093(02)01130-4`.

[19] M. Kent and D. Anderson. “Dielectric studies of added water in poultry meat and scallops”. In: *Journal of Food Engineering* 28.3 (1996), pp. 239–259. ISSN: 0260-8774. DOI: `https://doi.org/10.1016/0260-8774(95)00064-X`. URL: `http://www.sciencedirect.com/science/article/pii/026087749500064X`.

[20] K. K. Joshi and R. D. Pollard. “Microstrip resonator technique for non-destructive moisture/permittivity measurement”. In: *1999 IEEE MTT-S International Microwave Symposium Digest (Cat. No.99CH36282).* Vol. 4. June 1999, 1863–1866 vol.4. DOI: `10.1109/MWSYM.1999.780336`.

[21] G. Gennarelli et al. “A microwave resonant sensor for concentration measurements of liquid solutions”. In: *IEEE Sensors Journal* 13.5 (May 2013), pp. 1857–1864. ISSN: 1530-437X. DOI: `10.1109/JSEN.2013.2244035`.

[22] B. Kapilevich and B. Litvak. “Microwave sensor for accurate measurements of water solution concentrations”. In: *2007 Asia-Pacific Microwave Conference.* Dec. 2007, pp. 1–4. DOI: `10.1109/APMC.2007.4554682`.

[23] A. Ebrahimi et al. “High-sensitivity metamaterial-inspired sensor for microfluidic dielectric characterization”. In: *IEEE Sensors Journal* 14.5 (May 2014), pp. 1345–1351. ISSN: 1530-437X. DOI: `10.1109/JSEN.2013.2295312`.

[24] S. Harnsoongnoen and A. Wanthong. “Coplanar waveguides loaded with a split ring resonator-based microwave sensor for aqueous sucrose solutions”.

In: *Measurement Science and Technology* 27.1 (Dec. 2015), p. 015103. DOI: `10.1088/0957-0233/27/1/015103`. URL: `https://doi.org/10.1088%5C%2F0957-0233%5C%2F27%5C%2F1%5C%2F015103`.

[25] T. Chretiennot, D. Dubuc, and K. Grenier. "A microwave and microfluidic planar resonator for efficient and accurate complex permittivity characterization of aqueous solutions". In: *IEEE Transactions on Microwave Theory and Techniques* 61.2 (Feb. 2013), pp. 972–978. ISSN: 0018-9480. DOI: `10.1109/TMTT.2012.2231877`.

[26] A. A. Abduljabar et al. "Novel microwave microfluidic sensor using a microstrip split-ring resonator". In: *IEEE Transactions on Microwave Theory and Techniques* 62.3 (Mar. 2014), pp. 679–688. ISSN: 0018-9480. DOI: `10.1109/TMTT.2014.2300066`.

[27] A. Chahadih et al. "Microwave/microfluidic sensor fabricated on a flexible kapton substrate for complex permittivity characterization of liquids". In: *Sensors and Actuators A: Physical* 229 (2015), pp. 128–135. ISSN: 0924-4247. DOI: `https://doi.org/10.1016/j.sna.2015.03.027`. URL: `http://www.sciencedirect.com/science/article/pii/S0924424715001508`.

[28] V. Sekar et al. "A self-sustained microwave system for dielectric-constant Measurement of lossy organic liquids". In: *IEEE Transactions on Microwave Theory and Techniques* 60.5 (May 2012), pp. 1444–1455. ISSN: 0018-9480. DOI: `10.1109/TMTT.2012.2187066`.

[29] R. A. Potyrailo and W. G. Morris. "Multianalyte chemical identification and quantitation using a single radio frequency identification sensor". In: *Analytical Chemistry* 79.1 (2007), pp. 45–51.

[30] J. Chen et al. "Polarity-indicative two-dimensional periodic concave gratings of tethered polystyrene on silicon surfaces for visualization in VOC sensing". In: *Sensors and Actuators B: Chemical* 188 (2013), pp. 1123–1131. ISSN: 0925-4005. DOI: `https://doi.org/10.1016/j.snb.2013.08.026`. URL: `http://www.sciencedirect.com/science/article/pii/S0925400513009507`.

[31] H. Jensenius et al. "A microcantilever-based alcohol vapor sensor-application and response model". English. In: *Applied Physics Letters* 76.18 (2000), pp. 2615–2617. ISSN: 0003-6951. DOI: `10.1063/1.126426`.

[32] X. Yu et al. "Gassensing properties of perovskite BiFeO3 nanoparticles". In: *Journal of the American Ceramic Society* 92.12 (2009), pp. 3105–3107.

[33] X. Song, D. Zhang, and M. Fan. "A novel toluene sensor based on ZnOâSnO2 nanofiber web". In: *Applied Surface Science* 255 (May 2009), 7343â7347. DOI: `10.1016/j.apsusc.2009.02.094`.

[34] T. Ansbæk et al. "Vertical-cavity surface-emitting laser vapor sensor using swelling polymer reflection modulation". English. In: *Applied Physics Letters* 101.14 (2012), p. 143505. ISSN: 0003-6951. DOI: `10.1063/1.4754291`.

[35] D. M. Pozar. *Microwave Engineering*. John Wiley & Sons, 2012. Chap. 8, pp. 413–414.

[36] B. Bhat and S. K. Koul. *Stripline-like Transmission Lines for Microwave Integrated Circuits*. New York, NY, USA: Halsted Press, 1986. ISBN: 0470207000.

[37] T. Blecha. “Screen printed chipless RFID tags”. In: *Proceedings of the 2014 37th International Spring Seminar on Electronics Technology.* May 2014, pp. 143–146. DOI: `10.1109/ISSE.2014.6887581`.

[38] H. R. Khaleel et al. “A compact polyimide-based UWB antenna for flexible electronics”. In: *IEEE Antennas and Wireless Propagation Letters* 11 (2012), pp. 564–567. ISSN: 1536-1225. DOI: `10.1109/LAWP.2012.2199956`.

[39] C. P. Wen. “Coplanar waveguide: a surface strip transmission line suitable for nonreciprocal gyromagnetic device applications”. In: *IEEE Transactions on Microwave Theory and Techniques* 17.12 (Dec. 1969), pp. 1087–1090. ISSN: 0018-9480. DOI: `10.1109/TMTT.1969.1127105`.

[40] T. Kitazawa and Y. Hayashi. “Quasistatic characteristics of a coplanar waveguide with thick metal coating”. In: *IEE Proceedings H - Microwaves, Antennas and Propagation* 133.1 (Feb. 1986), pp. 18–20. ISSN: 0950-107X. DOI: `10.1049/ip-h-2.1986.0003`.

[41] K. Wu et al. “The influence of finite conductor thickness and conductivity on fundamental and higher-order modes in miniature hybrid MIC’s (MHMIC’s) and MMIC’s”. In: *IEEE Transactions on Microwave Theory and Techniques* 41.3 (Mar. 1993), pp. 421–430. ISSN: 0018-9480. DOI: `10.1109/22.223740`.

[42] J. Ke and C. Chen. “The coplanar waveguides with finite metal thickness and conductivity”. In: *1994 IEEE MTT-S International Microwave Symposium Digest (Cat. No.94CH3389-4).* May 1994, 1681–1684 vol.3. DOI: `10.1109/MWSYM.1994.335117`.

[43] R. N. Simons. “Conventional coplanar waveguide”. In: *Coplanar Waveguide Circuits, Components, and Systems*. IEEE, 2001. DOI: `10.1002/0471224758.ch2`. URL: `https://ieeexplore.ieee.org/xpl/articleDetails.jsp?arnumber=5237467`.

[44] W. Hilberg. “From approximations to exact relations for characteristic impedances”. In: *IEEE Transactions on Microwave Theory and Techniques* 17.5 (May 1969), pp. 259–265. ISSN: 0018-9480. DOI: `10.1109/TMTT.1969.1126946`.

[45] R. Garg K. C. Gupta and I. J. Bahl. *Microstrip Lines and Slot-Lines, Thrid Edition*. Artech House, 2013. ISBN: 9781608075355.

[46] F. Ellinger. “S-parameters and impedance transformation”. In: *Radio Frequency Integrated Circuits and Technologies*. Berlin, Heidelberg: Springer Berlin Heidelberg, 2007, pp. 57–78. ISBN: 978-3-540-35790-2. DOI: `10.1007/978-3-540-35790-2_3`. URL: `https://doi.org/10.1007/978-3-540-35790-2_3`.

[47] H. Kim and R. Franklin-Drayton. “Wire-bond free technique for right-angle coplanar waveguide bend structures”. In: *IEEE Transactions on Microwave Theory and Techniques* 57.2 (Feb. 2009), pp. 442–448. ISSN: 0018-9480. DOI: `10.1109/TMTT.2008.2011207`.

[48] M. N. Srifi et al. “Compact disc monopole antennas for current and future ultrawideband (UWB) applications”. In: *IEEE Transactions on Antennas and Propagation* 59.12 (Dec. 2011), pp. 4470–4480. ISSN: 0018-926X. DOI: `10.1109/TAP.2011.2165503`.

[49] F. Wang and T. Arslan. "Inkjet-printed antenna on flexible substrate for wearable microwave imaging applications". In: *2016 Loughborough Antennas Propagation Conference (LAPC)*. Nov. 2016, pp. 1–4. DOI: `10.1109/LAPC.2016.7807499`.

[50] A. C. Durgun et al. "Design, simulation, fabrication and testing of flexible bowtie antennas". In: *IEEE Transactions on Antennas and Propagation* 59.12 (Dec. 2011), pp. 4425–4435. ISSN: 0018-926X. DOI: `10.1109/TAP.2011.2165511`.

[51] V. Sharma and M. Hashmi. "Chipless RFID tag based on open-loop resonator". In: *2017 IEEE Asia Pacific Microwave Conference (APMC)*. Nov. 2017, pp. 543–546. DOI: `10.1109/APMC.2017.8251502`.

[52] Y. Zhao, D. Zhou, and Z. Niu. "Design of a microwave equalizer using microstrip open-loop rectangular ring substructure". In: *2009 3rd IEEE International Symposium on Microwave, Antenna, Propagation and EMC Technologies for Wireless Communications*. Oct. 2009, pp. 1043–1046. DOI: `10.1109/MAPE.2009.5355872`.

[53] E. O Hammerstad and N. T. Hogskole. "Microstrip handbook". English. In: (1975). Includes index.

[54] R. Grag and I. J. Bahl. "Microstrip discontinuities". In: *International Journal of Electronics* 45.1 (1978), pp. 81–87. DOI: `10.1080/00207217808900883`. eprint: `https://doi.org/10.1080/00207217808900883`. URL: `https://doi.org/10.1080/00207217808900883`.

[55] A. Sabban and K. C. Gupta. “A planar-lumped model for coupled microstrip line discontinuities”. In: *IEEE International Digest on Microwave Symposium.* May 1990, 247–250 vol.1. DOI: `10.1109/MWSYM.1990.99566`.

[56] J. D. Baena et al. “Equivalent-circuit models for split-ring resonators and complementary split-ring resonators coupled to planar transmission lines”. In: *IEEE Trans. Microw. Theory Tech.* 53.4 (Apr. 2005), pp. 1451–1461. ISSN: 0018-9480. DOI: `10.1109/TMTT.2005.845211`.

[57] Z. Li and S. Bhadra. “A flexible printed complementary split-ring resonator based chipless RFID”. In: *2018 18th International Symposium on Antenna Technology and Applied Electromagnetics (ANTEM).* Aug. 2018, pp. 1–2. DOI: `10.1109/ANTEM.2018.8572905`.

[58] J. Bonache et al. “On the electrical characteristics of complementary metamaterial resonators”. In: *IEEE Microwave and Wireless Components Letters* 16.10 (Oct. 2006), pp. 543–545. ISSN: 1531-1309. DOI: `10.1109/LMWC.2006.882400`.

[59] J. Lim et al. “A spiral-shaped defected ground structure for coplanar waveguide”. In: *IEEE Microwave and Wireless Components Letters* 12.9 (Sept. 2002), pp. 330–332. ISSN: 1531-1309. DOI: `10.1109/LMWC.2002.803208`.

[60] L. Young G. L. Matthaei and E. M. T. Jones. *Microwave filters, impedance-matching networks, and coupling structures*. Artech House, 1980.

[61] K. Ebnabbasi et al. “Taper design of vivaldi and co-planar tapered slot antenna (TSA) by Chebyshev transformer”. In: *IEEE Transactions on Antennas and Propagation* 60.5 (May 2012), pp. 2252–2259. ISSN: 0018-926X. DOI: `10.1109/TAP.2012.2189697`.

[62] B. Shuppert. “Microstrip/slotline transitions: modeling and experimental investigation”. In: *IEEE Transactions on Microwave Theory and Techniques* 36.8 (Aug. 1988), pp. 1272–1282. ISSN: 0018-9480. DOI: `10.1109/22.3669`.

[63] R. Janaswamy and D. H. Schaubert. “Characteristic impedance of a wide slotline on low-permittivity substrates”. In: *IEEE Transactions on Microwave Theory and Techniques* 34.8 (Aug. 1986), pp. 900–902. ISSN: 0018-9480. DOI: `10.1109/TMTT.1986.1133465`.

[64] K. Lee and W. Chen. *Advances in Microstrip and Printed Antennas.* John Wiley & Sons, 1997. ISBN: 9780471044215.

[65] J. Speight. *Lange’s Handbook of Chemistry.* McGraw-Hill Education, 2005. ISBN: 9780071432207.

[66] R. L. Scot J. H. Hildebrand. *The Solubility of Nonelectrolytes.* New York, NY, USA: Reinhold, 1950.

[67] R. V. Koswatta and N. C. Karmakar. “A novel reader architecture based on UWB chirp signal interrogation for multiresonator-based chipless RFID tag reading”. In: *IEEE Transactions on Microwave Theory and Techniques* 60.9 (Sept. 2012), pp. 2925–2933. ISSN: 0018-9480. DOI: `10.1109/TMTT.2012.2203929`.

Index

KEY TO ABBREVIATIONS

ADS: Advanced Design Studio 126

ASIC: application specific integrated circuit 126

CIJ: continuous inkjet printing 126

CPW: coplanar waveguide 126

CSRR: complementary split-ring resonator 126

DOD: drop-on-demand 126

HFSS: high-frequency structure simulation 126

IoT: Internet-of-Things 126

KCL: Kirchoff's Current Law 126

KVL: Kirchoff's Voltage Law 126

NaCl: soldium Chloride 126

PCB: printed circuit board 126

PDMS: polydimethylsiloxane 126

RCS: radar cross section 126

RFID: radio frequency identification 126

SAW: surface acoustic wave 126

TEM: transverse electromagnetic wave 126

UWB: ultra-wideband 126

VCSEL: vertical-cavity surface-emitting laser 126

VNA: vector network analyzer . . . 126

VOC: volatile organic compound . . . 126

VSWR: voltage standing wave ratio . . . 126